Performance Enhancement and Stability Robustness of Wing/Store Flutter Suppression System

Prasad V. N. Gade

Dissertation submitted to the Faculty of the
Virginia Polytechnic Institute and State University
in partial fulfillment of the requirements for the degree of

Doctor of Philosophy
in
Engineering Mechanics

Daniel J. Inman, Chair
Eugene M. Cliff
Harley H. Cudney
Robert A. Heller
Liviu Librescu

February 6, 1998
Blacksburg, Virginia

Keywords: Wing/Store Flutter Control, Active Decoupler Pylon, Robust Control Strategies

Performance Enhancement and Stability Robustness of Wing/Store Flutter Suppression System

Prasad V. N. Gade

(ABSTRACT)

In recent years, combat aircraft with external stores have experienced a decrease in their mission capabilities due to lack of robustness of the current passive wing/store flutter suppression system to both structured as well as unstructured uncertainties. The research program proposed here is to investigate the feasibility of using a piezoceramic wafer actuator for active control of store flutter with the goal of producing a robust feedback system that demonstrates increased performance as well as robustness to modeling errors. This approach treats the actuator as an active soft-decoupling tie between the wing and store, thus isolating the wing from store pitch inertia effects. Advanced control techniques are used to assess the nominal performance and robustness of wing/store system to flutter critical uncertainties.

This research is generously supported by the Air Force Office of Scientific Research (AFOSR-F49620-95-1-0362) under the direction of Maj. Brian Sanders, Ph.D.

Dedication

This dissertation is dedicated to four of my dearest in the world: my parents: Mr. Balakrishna Rao and Mrs. Gowri, my brother: Jagannadh Das, and to my lovely wife: Sridevi.

Acknowledgments

The successful completion of this dissertation wouldn't have been possible without the support and friendship from several people who have contributed to my learning process, both academically as well as morally.

Foremost, I would like to thank my mentor Prof. Daniel J. Inman for his patience and guidance throughout the course of my Ph.D. work. His unique and gifted attitude to many aspects of life, has always been, and will always be, a great source of inspiration for me. I have learned a great deal from him and would really miss his company. I also extend my gratitude to my committee members for their valuable suggestions and discussions on my research topic. I would also like to thank all of my current and ex-colleagues who have given me excellent support and friendship all these years and made my stay a memorable one. My sincere gratitude is also extended to Maj. Brian Sanders, Ph.D. who supervised this work that was generously supported under the auspices of the Air Force Office of Scientific Research via the grant AFOSR-F49620-95-1-0362.

Last, but not in any measure, the least, I would like to thank my parents for bringing me up to what I am now and for providing me with the best education possible through their hard work and several sacrifices. I thank them very much for having confidence in me throughout my academic career. Thanks are due to my dear brother whose cheerfulness has always lifted my spirits. Thanks for being with me throughout. And finally I would like to thank my dear wife and sweetheart, Sridevi, the most, for her moral support and understanding that gave me strength to complete this dissertation successfully. I thank her

for being patient especially during the last few months and I promise her that it will definitely pay-off.

Contents

List of Figures

List of Tables

Nomenclature

ab	distance between elastic center and mid-chord
b	semi-chord length
h	plunge displacement
i	$\sqrt{-1}$
$\ell_1 b$	distance between top of strut to elastic center
$\ell_2 b$	distance between pivot-point to elastic center
m_f	fictitious noise intensity coefficient
m_a	mass per unit length of the piezoceramic wafer actuator
m_s	mass of the store
m_w	mass of the wing
$r_\alpha b$	radius of gyration of airfoil about elastic center
$r_\theta b$	radius of gyration of pylon/store about pivot-point
s	Laplace variable
$\overline{s}$	reduced frequency, bs/U
U	free stream velocity
u	actuator output (restoring moment to the store)
$x_\alpha b$	distance between elastic center and c.g. of wing
$x_\theta b$	distance between c.g. of store to pivot-point
x_1, x_2	aerodynamic lag states
α	pitch angle of airfoil

γ	tuning parameter used in weighting functions
Δ	multiplicative uncertainty transfer matrix
ρ	density of air
θ	pitch angle of store relative to airfoil
σ	minimum singular value
σ	maximum singular value
ω_h	uncoupled wing bending frequency
ω_α	uncoupled wing torsional frequency
ω_θ	uncoupled store pitch frequency

Chapter 1

Introduction

Military aircraft are required to carry several combinations of under-wing external stores to accomplish a variety of missions. Rigid mountings of these stores causes the coupling between the first torsional mode and fundamental bending frequency of the wing to occur sooner than for the case of a bare wing. This results in a substantial decrease in flutter speed critical for the survivability against anti-aircraft guns. Although passive methods such as structural and mass balance techniques have claimed to alleviate flutter, the associated added weights generally results in decreased aircraft performance. Moreover the requirement on the aircraft to carry several combinations of stores makes its implementation practically impossible. The use of semi-active control technology suggested in the past also has its own disadvantages. In particular, the use of hydraulically actuated ailerons for control of store induced flutter did not gain popularity because of the difficulty in the prediction of counteracting unsteady aerodynamic forces produced by the control surfaces and insufficient hydraulic flow-rate requirements. In the early eighties, a novel semi-passive approach of using a soft-spring pivot mechanism for isolating the wing torsion mode from store pitch inertia effects was experimentally proven to be successful in alleviating flutter. The objective of the current research is investigate the feasibility of robustifying the decoupler pylon mounted system using active control technology. Instead of a passive decoupler pylon, a

piezoelectric wafer actuator consisting of a series of thin circular plates with piezoceramics laminated to its opposite sides, is proposed for use an active decoupling tie between the wing and the store. The major use of piezoceramic actuator controlled system is the solution it provides to the time delay problems imposed by hydraulic actuators. Although active control technology also has weight penalties due to actuator mass and electronic hardware, the flexibility it offers in addressing robustness issues via modern dynamic feedback controllers places it at an advantageous position relative to passive methods. By exploring various modern advanced control laws with the actuator and coupled fluid-structure models, issues of improving the robustness of a wing/store system to changes in the store configuration and nominal performance characteristics are investigated.

1.1 Literature Review

Flutter can be alleviated by conventional passive schemes or by the more advanced active approaches. Passive methods typically include adding mass ballast, relocating store location span-wise and/or chord-wise or tuning the pylon stiffness characteristics [1, 2, 3]. But these methods are generally tailored to a specific configuration and fail to accommodate different store mass and location combinations.

Active methods on the other hand, are relatively more flexible and require mere change of control law to accommodate different store combinations. One of the earliest known works on the feasibility of using active control for wing/store flutter suppression was reported by Triplett [4] in 1972. His analytical study of an F-4 Phantom aircraft wing/store configuration involved deflecting ailerons in a manner to produce aerodynamic forces that opposed the flutter causing aerodynamic forces. A number of other investigators made important contributions to the field of active wing/store flutter suppression [5, 6]. In 1979 Harvey and his coworkers [7] investigated the feasibility of using adaptive control for wing/store flutter suppression with the above approach. Some researchers [8, 9] proposed a slightly

modified version which involved feeding back signals from the accelerometers at the fore and aft end of the store to electro-hydraulic actuators to drive vanes attached to the forward part of the store. The deflected vanes generated counteracting aerodynamic forces that stabilized the store pitch motion. Hönlinger and Destuynder [10] used a Linear Quadratic Regulator (LQR) control law to test the above procedure on a Phantom F-4F wing/store configuration. The effectiveness of these methods, however, depended largely on the accurate knowledge of counteracting unsteady aerodynamic forces produced by the control surfaces. This poses a particular problem especially in the transonic range where the theoretical predictions of the unsteady aerodynamic coefficients of the control surfaces are least reliable [11, 12].

Triplett's feasibility study [4] in 1972 gained interest in the aeronautical community and was soon followed by an Air Force contract to evaluate the ability of a single wing/store flutter control scheme that would be robust to several different store configurations [13]. Instead of using control surface's unsteady aerodynamics as in the earlier active methods, Triplett and his colleagues proposed to use a hydraulic actuator to decouple the store vibratory motion from that of the wing. Although the dynamic behavior of this scheme worked quite well in restoring bare wing flutter speed, the actuator's inability to meet high flow rate requirements for the control of higher frequency perturbations restricted its practical implementation.

Instead of looking at actuating control surfaces for wing/store flutter suppression, Reed et al. [11] in 1980 argued that the issue should be addressed by looking at the more fundamental cause of flutter i.e. the coupling between the bending and torsional mode of the wing/store system. They proposed a modified version of the above approach. Instead of using a hydraulic actuator as a load carrying tie, a passive soft-spring/damper combination was used together with a low-power active control system to maintain store alignment.

Their idea is based on the argument that instead of modifying the aerodynamic forces, the frequencies associated with flutter critical bending and torsion modes can be separated by making the wing insensitive to store pitch inertia and eventually alleviate the

adverse coupling to a higher flutter speed. Some researchers [14-18] analyzed this concept and successfully demonstrated its use in wing/store bending-torsion flutter suppression. The bending-torsion flutter [19] involves coupling or the coalescence of bending and torsion mode frequencies as the flutter speed is approached. The frequencies at zero air speed are those due to the undamped inertially coupled bending and torsion motions. These are slightly reduced from their natural values due to the apparent additional mass term associated with non-circulatory component of the aerodynamic loads. The dashed pair of curves represent a rigidly attached store while the solid pair represent a decoupler pylon mounted store. Since the decoupler pylon isolates the wing from the influence of store pitch inertia, the wing torsion frequency with the decoupled store is substantially higher than that for the wing with the rigidly attached store. As the flight speed is increased, the bending branch frequency remains approximately equal to its ground frequency while torsion branch frequency decreases from its decoupled ground frequency to a frequency where both branches comes close to one another. These branches do not however coalesce because of the presence of aerodynamic damping present in the system.

The design of a decoupler pylon mounted store consists of a pitch-pivot mechanism near the fore end that allows the store to pitch relative to the wing surface. Near the aft end, a soft spring is used to decouple the influence of store pitch inertia on wing torsion modes. A low frequency feedback control is used to prevent large static deflections and maintain alignment. The result is a substantial increase in flutter speed, well beyond that of the bare wing. Based on a feasibility study [20], a decoupler pylon was fabricated by Clayton et al. [21] and was later successfully implemented on an F-16 aircraft to increase the flutter speed. Instead of passive soft-spring/damper elements as used by Reed to demonstrate his concept, the current approach proposes an active decoupler pylon for the control of wing/store flutter suppression. The proposed active isolation scheme, shown in Fig. 1.1, serves two purposes. First it decouples the wing dynamics from the store pitch inertia effects - a primary source for bending-torsion flutter in wing with external stores. Second, with the aid of a robust controller, it acts as an actuator that stabilizes and maintains the

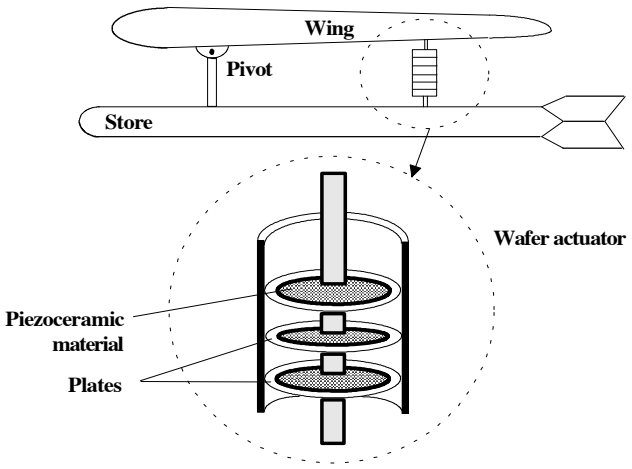

Figure 1.1: Wing/store piezostrut arrangement

performance characteristics of the closed-loop system in the face of uncertainties at flutter speed. The active pylon consists of a strut with series of thin circular plates laminated on opposite faces with piezoceramic material. The poled directions of the piezoceramics are aligned so that a voltage (control input) applied across the element contracts on one side and expands on the other. The plate bending is then translated into an axial motion along the strut. The piezostrut is designed such that its equivalent stiffness satisfies Reed's criterion [11] of a soft spring system for isolation purposes, i.e., the store pitch to wing bending frequency ratio should always be less than 1 for effective store flutter alleviation. The novelty in this approach is the use of the strut as both a passive isolator as well as an active actuator to maintain stability and performance. The current active concept has two major advantages over other passive schemes [11, 20, 21]. Not only does the active decoupler makes the system more robust to various uncertainties, but it also has significant weight benefits because it gets away with all the hardware that is required with pneumatic springs and hydraulic dashpots. Moreover, compared to that of a hydraulic actuator, wafer actuator's faster time response to input command signals makes it suitable for store flutter suppression problem.

It is proposed that this device will represent a significant improvement in the much needed stroke length requirement over the traditional stack actuator [22] which has been shown to fail in providing the much needed stroke length for restoring the bare wing flutter speed. Moreover these actuators typically fail in tension because of the brittle nature of the piezoceramic materials. On the other hand, the current bender-element type actuator, initially fabricated and designed [23] for use in a large flexible structure, behaves the same both in tension as well in compression. Several issues pertaining to the actuator are yet to be quantified such as actuator dynamics, its time response to input command signals relative to hydraulic actuators, stroke length capability over traditional stack actuators and power requirements. At the time of writing of this dissertation, the dynamics of the actuator had not yet been identified and hence are not included. Therefore the approach taken here is to lump the actuator dynamics into the uncertainty model.

1.2 Dissertation Outline

The dissertation is organized in the following manner: Chapter 2 presents the equations of motion of the typical section wing with a decoupler pylon mounted store. It incorporates the generalized forces due to piezostrut actuator on the wing and the store. Jones' approximation is used to model the circulatory part of the aerodynamics on the wing section in incompressible flow where the store aerodynamics are ignored for simplification. The equations of motion are then cast into state-space form. An uncertainty dynamic model is also developed for use with various control laws for robust stability analysis. In Chapter 3, the state-space equations are used as the plant model to design a continuous-time domain controller, based on LQG/LTR control law. Nominal performance and stability robustness analysis are performed to investigate the effectiveness of using active decoupler pylon concept. Chapter 4 treats the same kind of analysis by designing an $\mathcal{H}_\infty$ controller wherein a mixed-sensitivity objective is solved using Glover-Doyle algorithm. The design of a robust adaptive control law is presented in Chapter 5 in which a self-tuning algorithm is numerically

implemented to investigate the store release problem. Chapter 6 presents the conclusions of the this dissertation and lists some recommendations for future work.

1.3 Summary of Contributions

The following are the original contributions contained in this dissertation:

1. The concept of an active decoupler pylon is introduced for performance enhancement and stability robustness of the wing/store flutter suppression system.

2. A wing/store-piezostrut model is developed with a typical section configuration and using a 2-D incompressible flow theory. The non-conservative generalized forces due to the proposed active decoupler pylon actuator acting on the wing and store is incorporated via the principle of virtual work.

3. An uncertainty model is developed which assumes that majority of the uncertainty is due to ignoring store aerodynamics. It is derived based on the argument that had the store aerodynamics been included, then the circulatory aerodynamic component of the wing and store combination can be approximated by the same equations that are used to represent the aero loads around the wing, with the exception that the Jones' rational function be replaced by some Jones'-like transfer function that closely captures the wing/store aerodynamics. Although it would still be an approximation to the true Theodorsen-like function (involving complex modified Bessel function), a rough representation of uncertainty can be developed by considering the error between the Jones'-like and Jones approximations.

4. The above uncertainty model is expressed as an input multiplicative error by reflecting all the inaccuracies at the input of the plant and was analyzed for robustness using LQG/LTR optimal control law. Nominal performance and perturbation analysis was done to evaluate issues with the implementation of such a control law.

5. $\mathcal{H}_\infty$ control law with a mixed-sensitivity objective was numerically implemented for wing/store flutter suppression system. Nominal performance analysis and stability robustness for uncertainty model expressed as an output multiplicative uncertainty was studied. A $\mathcal{H}_\infty$ algorithm based on Glover-Doyle is used for the design of control system. Appropriate weighting functions to characterize performance and robust stability are used in the process.

6. Previous Self-Tuning Regulator method adopted in 1970's did not include robustness modifications. This work presents an up-to-date robust adaptive control law to study the problem of a store release event. This is the first record to address the store release problem.

Chapter 2

Analytical Model

This chapter presents the derivation of an analytical model of wing/store/strut system in an incompressible flow regime. Section 2.1 presents the typical section wing/store formulation, the typical section part of which is found in any standard text on aeroelasticity [19]. Section 2.2 presents the procedure for incorporating the non-conservative forces due to actuator acting on the wing/store system. Two-dimensional unsteady incompressible fluid flow around the typical Section 2.3 are then included to form the final set of equations. Equations derived in Section 2.3 are then normalized and presented in Section 2.4. To aid in controller design using modern control algorithms, the normalized equations are finally cast into state-space in Section 2.5. Section 2.6 presents some open-loop studies to calculate the flutter boundary of a wing with decoupler pylon mounted store. In Section 2.7, definitions of some frequently used uncertainty models are presented and an approximate model is constructed based on Jones' approximation. Finally section 2.8 summarizes the chapter.

2.1 Wing/Store Typical Section Formulation

The analytical model is restricted to a typical section of a thin airfoil with an underwing external store. This is to facilitate numerical implementation of modern state-space based control laws for design and analysis purpose. A sketch of the typical section together with the decoupler pylon and the store is shown in Fig. 2.1.

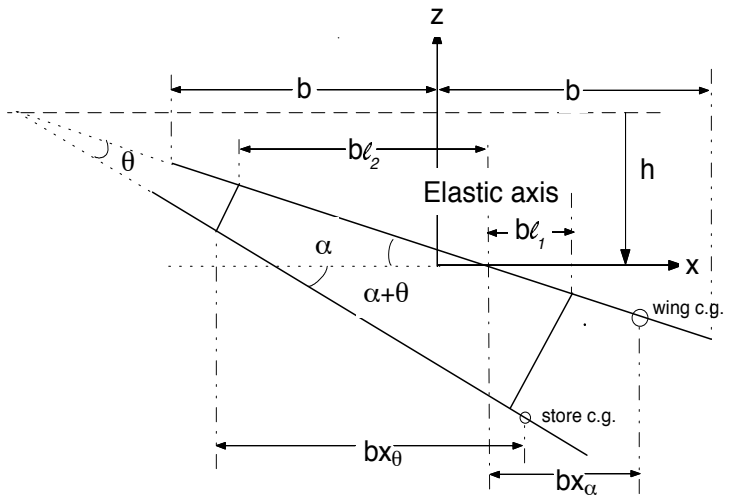

Figure 2.1: Schematic diagram of a thin airfoil and decoupler pylon mounted store

The three degrees-of-freedom considered here are the wing/store combination plunging or bending motion h, the wing pitch angle α and the store pitch angle measured relative to the undeformed wing θ. Linear and torsional springs at the elastic center are used to model the restraining forces generated by the vertical and angular displacements of the airfoil, while restraint to the pitching motion of the store is provided by the decoupler pylon mechanism. Standard sign conventions are used in which the plunging displacement is measured positive downward while a nose-up position of the structure implies a positive pitching angle. The total lift on the airfoil is defined positive up while the pitching moment of the entire airfoil about the one-quarter chord length point is positive in the nose-up sense.

From Fig. 2.1 the position vector is given by

$$w_w = (-h - x_\alpha b\alpha)\vec{j}$$

and the kinetic energy is written as

$$T_w = \frac{1}{2}\int_{chord} \dot{w}_w.\dot{w}_w dm = \frac{1}{2}(m_w\dot{h}^2 + 2m_w x_\alpha b\dot{h}\dot{\alpha} + m_w x_\alpha^2 b^2\dot{\alpha}^2) + \frac{1}{2}I_{wcg}\dot{\alpha}^2 \tag{2.1}$$

where an additional term resulting from the rotation of the wing relative to its center of gravity has been added. If I_w is the mass moment of inertia of the wing about the elastic axis, then it can be expressed as $I_w = I_{wcg} + m_w x_\alpha^2 b^2 = m_w r_\alpha^2 b^2$ where $r_\alpha b$ is the radius of gyration of the wing. The kinetic energy can then accordingly be modified as

$$T_w = \frac{1}{2}(m_w\dot{h}^2 + 2m_w x_\alpha b\dot{h}\dot{\alpha} + m_w r_\alpha^2 b^2\dot{\alpha}^2) \tag{2.2}$$

Similarly with the position vector for the center of gravity location of store given by

$$w_s = [-h - (x_\theta - \ell_2)b\alpha - x_\theta b\theta]\,\vec{j}$$

the corresponding kinetic energy can be written as

$$\begin{aligned} T_s &= \frac{1}{2}\int_{store} \dot{w}_s.\dot{w}_s dm \\ &= \frac{1}{2}m_s[\dot{h}^2 + b^2(x_\theta - \ell_2)^2\dot{\alpha}^2 + b^2 r_\theta^2\dot{\theta}^2 + 2(x_\theta - \ell_2)b\dot{h}\dot{\alpha} + 2b^2(x_\theta - \ell_2)x_\theta\dot{\alpha}\dot{\theta} + 2x_\theta b\dot{h}\dot{\theta}] \end{aligned} \tag{2.3}$$

where $r_\theta b$ is the radius of gyration of the store obtained as a result of considering kinetic energy from the rotation of the store relative to its center of gravity. The sum total of the kinetic energies of the wing and the store is given by

$$\begin{aligned} T_{w/s} &= T_w + T_s \\ &= \frac{1}{2}m_w\dot{h}^2 + m_w r_\alpha b\dot{h}\dot{\alpha} + \frac{1}{2}m_w x_\alpha^2 b^2\dot{\alpha}^2 + \frac{1}{2}m_s\dot{h}^2 + \frac{1}{2}(m_s x_\theta^2 + m_s\ell_2^2 - 2m_s x_\theta\ell_2)b^2\dot{\alpha}^2 \\ &+ \frac{1}{2}m_s r_\theta^2 b^2\dot{\theta}^2 + (m_s x_\theta - m_s\ell_2)b\dot{h}\dot{\alpha} + (m_s x_\theta^2 - m_s x_\theta\ell_2)b^2\dot{\alpha}\dot{\theta} + m_s x_\theta b\dot{h}\dot{\theta} \end{aligned} \tag{2.4}$$

The total potential energy can similarly be written as

$$V_{w/s} = \underbrace{\frac{1}{2}K_h h^2 + \frac{1}{2}K_\alpha\alpha^2}_{V_w} + \underbrace{\frac{1}{2}K_\theta\theta^2}_{V_s} \tag{2.5}$$

Performing the operations

$$\frac{d}{dt}\left(\frac{\partial L}{\partial h}\right) - \frac{\partial L}{\partial h} = -L_{aero} + Q_{act-h}$$
$$\frac{d}{dt}\left(\frac{\partial L}{\partial \alpha}\right) - \frac{\partial L}{\partial \alpha} = M_{aero} + Q_{act-\alpha}$$
$$\frac{d}{dt}\left(\frac{\partial L}{\partial \theta}\right) - \frac{\partial L}{\partial \theta} = 0 + Q_{act-\theta}$$

on the Lagrangian $L = T_{w/s} - V_{w/s}$ would yield the following three governing equations

$$(m_w + m_s)\ddot{h} + (m_w x_\alpha b + m_s x_\theta b - m_s \ell_2 b)\ddot{\alpha} + (m_s x_\theta b)\ddot{\theta} + K_h h = -L_{aero} + Q_{act-h} \tag{2.6}$$

$$(m_w x_\alpha b + m_s x_\theta b - m_s \ell_2 b)\ddot{h} + (m_w r_\alpha^2 b^2 + m_s r_\theta^2 b^2 + m_s \ell_2^2 b^2 - 2m_s x_\theta \ell_2 b^2)\ddot{\alpha}$$
$$+(m_s r_\theta^2 b^2 - m_s x_\theta \ell_2 b^2)\ddot{\theta} + K_\alpha \alpha = M_{aero} + Q_{act-\alpha} \tag{2.7}$$

$$(m_s x_\theta b)\ddot{h} + (m_s r_\theta^2 b^2 - m_s x_\theta \ell_2 b^2)\ddot{\alpha} + (m_s r_\theta^2 b^2)\ddot{\theta} + K_\theta \theta = 0 + Q_{act-\theta} \tag{2.8}$$

where L_{aero} is the aerodynamic lift acting on the wing/store system and M_{aero} is the aerodynamic moment per semi-chord length for a unit span acting about the elastic center. Aerodynamic effects on the store are however ignored and is reflected by the presence of a zero term on the right side of Eq. (2.8). Structural damping is neglected and the gravitational effects are ignored. The terms $Q_{act-h}, Q_{act-\alpha}$ and $Q_{act-\theta}$ represent the components of the generalized actuator forces and moments acting on the wing/store system which are calculated in the next section. The three stiffness terms K_h, K_α and K_θ can also be replaced by $m_w\omega_h^2, m_w r_\alpha^2 b^2 \omega_\alpha^2$ and $m_s r_\theta^2 b^2 \omega_\theta^2$ respectively. Here ω_h, ω_α and ω_θ are the uncoupled wing bending, wing torsion and store pitch frequencies respectively. The term K_θ in Eq. (2.8) is the equivalent stiffness of the piezostrut actuator providing restoring moment to the store and is defined as $\omega_\theta^2 = K_\theta / m_s r_\theta^2 b^2$. Here all the linear distances are expressed as a fraction of the semi-chord length b.

2.2 Generalized Forces Due to Actuator

The primary element of the proposed actuator shown in Fig. 1.1 is a strut, made up of either aluminium or steel and consists of a series of thin circular substrates with piezoceramics laminated on either one or both sides. These substrates are simply supported at the outer edge by the actuator superstructure. The configuration of the actuator superstructure-substrate connection results in a geometrically "parallel" configuration. The piezoceramic wafers are also electrically wired in parallel. The poling direction of the piezoceramic laminates is such that a voltage applied across the element results in an in-plane contraction/expansion of the element. The in-plane induced strain of the substrate results in bending of the laminate. The net result is therefore an axial motion of the strut producing restoring moment to the store against misalignment during maneuvers.

Following the derivation and notation of Ref. [24], the strut is modeled by finite elements using linear shape functions given by

$$w_{act}(z_a, t) = \left[\left(1 - \frac{z_a}{L_a}\right) w_1(t) + \left(\frac{z_a}{L_a}\right) w_2(t)\right] \vec{j} \tag{2.9}$$

The kinetic energy is then be given by

$$T_{act} = \int_{act} \frac{1}{2} \rho_a \dot{w}_{act} . \dot{w}_{act} d\Omega \tag{2.10}$$

where ρ_a is the mass density with mass per unit length of the actuator denoted by m_a and area of cross section of the strut being A_a. The displacement variable z_a varies along the length L_a of the actuator. On simplification, the kinetic energy can be written as

$$T_{act} = \frac{1}{6} m_a L_a (\dot{w}_1^2 + \dot{w}_1 \dot{w}_2 + \dot{w}_2^2) \tag{2.11}$$

In addition to elastic energy, the potential energy has the contribution of net work due to induced axial strain along the strut which is a result of applied voltage at discrete number of wafer plate stations. The total potential energy is then given by

$$\begin{aligned} V_{act} &= \frac{1}{2} \int_0^{L_a} \frac{E A_a}{L_a^2} (w_2 - w_1)^2 dz + mutual + dielectric \\ &= \frac{1}{2} \frac{E A_a}{L_a} (w_2 - w_1)^2 + \mathcal{F}(\phi) Q \end{aligned} \tag{2.12}$$

where Q is the electric charge and $\mathcal{F}(\phi)$ consists of parameters such as dielectric constant, permitivity and piezoelectric constants of the material, radius of the bender elements etc. Since at the time of writing, actuator dynamics haven't been fully characterized or experimentally verified [25], the last term in the above equation is left out as a function of typical parameters contributing to the dynamics of the actuator. A good starting point for the interested reader would be Ref. [23] where Pokines derived force induced in the strut due to expansion and contraction of the piezoceramics around the neutral axis of the bender element.

The non-conservative forces present are the applied forces (N_1, N_2) and the voltage $(\bar{V})$. N_1 and N_2 are the two axial forces of opposite signs applied to the wing/store structure at the nodal points by the actuator. To model the active structure with these known applied forces and voltages, the absolute mechanical displacements (w_1, w_2) and electric charge Q are chosen as independent variables. The work done by the non-conservative forces can be written as

$$W_{act} = N_1 w_1 + N_2 w_2 - \bar{n}\bar{V}Q \tag{2.13}$$

where $\bar{n}$ is the number of wafer plates along the strut. Applying Hamiltons principle

$$\delta \int_{t_1}^{t_2} (T_{act} - V_{act} + W_{act}) dt = 0 \qquad \delta w_1, \delta w_2, \delta Q = 0 \ \text{ at } \qquad t = t_1, t_2 \tag{2.14}$$

to the kinetic energy, potential energy and the non-conservative work equations, the following governing equations are obtained as

$$\frac{m_a L_a}{6} \begin{bmatrix} 2 & 1 \\ 1 & 2 \end{bmatrix} \begin{Bmatrix} \ddot{w}_1 \\ \ddot{w}_2 \end{Bmatrix} + \frac{EA_a}{L_a} \begin{bmatrix} 1 & -1 \\ -1 & 1 \end{bmatrix} \begin{Bmatrix} w_1 \\ w_2 \end{Bmatrix} = \begin{Bmatrix} N_1 + \mathcal{F}(\psi)\bar{V} \\ N_2 - \mathcal{F}(\psi)\bar{V} \end{Bmatrix} \tag{2.15}$$

where $\mathcal{F}(\psi)$ will be a function of the piezoelectric constant d_{31}, thickness of the piezoceramic wafer elements, diameter of bender elements, dielectric constant and other critical parameters contributing to the net induced strain in the strut. Reference [24] provides a comprehensive discussion on the derivation of the governing equations of a piezoceramic stack actuator.

The above equations can be used to derive the actuator force and moments (Eqs. 2.6-2.8) acting on the wing/store system by first expressing the absolute nodal displacements w_1 and w_2 of the piezostrut in terms of the generalized coordinates h, α, and θ. Assuming small pitching motion about the airfoil and the store, the position vector of the tip of the strut (at the wing end) with respect to center of mass of the wing can be written as

$$w_1 = -(h + \ell_1 b\alpha)\vec{j}$$

and the force acting on the wing due to actuator axial strain is given by

$$F_w = N_1\vec{j}$$

Therefore the work done on the wing due to actuator stroke can be obtained from the principle of virtual work,

$$\delta W_{act-w} = F_w.\delta w_1 = -N_1\delta h - N_1\ell_1 b\delta\alpha \tag{2.16}$$

Similarly the virtual work on the store can be obtained by taking the dot product of the position vector w_2 of the tip of the strut at the store end (with respect to center of mass of the store) and axial force of the piezostrut N_2 on the store as

$$\begin{aligned} w_2 &= -[h - \ell_1 b(\alpha + \theta)]\vec{j} \\ F_s &= N_2\vec{j} \end{aligned}$$

resulting in

$$\delta W_{act-s} = -N_2\delta h - N_2\ell_1 b\delta\alpha - N_2\ell_1 b\delta\theta \tag{2.17}$$

The total virtual work done on the wing and store by the actuator is given by

$$\delta W_{act-w} + \delta W_{act-s} = -(N_1 + N_2)\delta h - (N_1\ell_1 b + N_2\ell_1 b)\delta\alpha - N_2\ell_1 b\delta\theta \tag{2.18}$$

From the above equation the generalized force and moments due to the actuator on the

wing/store system can be expressed as

$$\begin{aligned} Q_{act-h} &= -N_1 - N_2 \\ &= -\frac{1}{6} m_a L_a (6\ddot{h} + 6\ell_1 b\ddot{\alpha} + 3\ell_1 b\ddot{\theta}) \qquad (2.19) \\ Q_{act-\alpha} &= -N_1\ell_1 b - N_2\ell_1 b \\ &= -\frac{1}{6} m_a L_a (6\ell_1 b\ddot{h} + 6\ell_1^2 b^2\ddot{\alpha} + 3\ell_1^2 b^2\ddot{\theta}) \qquad (2.20) \\ Q_{act-\theta} &= -N_2\ell_1 b \\ &= -\frac{1}{6} m_a L_a (3\ell_1 b\ddot{h} + 3\ell_1^2 b^2\ddot{\alpha} + 2\ell_1^2 b^2\ddot{\theta}) - \frac{EA_a}{L_a}\ell_1^2 b^2\theta - \mathcal{F}(\psi)\ell_1 b\bar{V} \qquad (2.21) \end{aligned}$$

where $m_a L_a$ is the total mass of the actuator and $\mathcal{F}(\psi)$ includes piezoceramic properties such as the piezoelectric constant d_{31}, the permitivity constant of the piezoelectric material, effective radius of the bender elements, the thickness of the wafer plates, etc [23].

2.3 Generalized Aerodynamic Loads

In this work, the controller design and analysis are done only in incompressible flow regime as is common in previously published work on store flutter [14]. A method for calculating the two-dimensional incompressible unsteady aerodynamic loads for simple harmonic oscillations of a wing section was first given by Theodorsen [26]. The aerodynamic loads thus calculated are given by

$$\begin{aligned} -L_{aero} &= -\pi\rho b^2[\ddot{h} + U\dot{\alpha} - ab\ddot{\alpha}] - 2\pi\rho UbT(k)[\dot{h} + U\alpha + (0.5 - a)b\dot{\alpha}] \qquad (2.22) \\ M_{aero} &= \pi\rho b^2[ab\ddot{h} - U(0.5 - a)b\dot{\alpha} - b^2(1/8 + a^2)\ddot{\alpha}] + 2\pi\rho U(0.5 + a)b^2T(k)[\dot{h} \\ &\quad + (0.5 - a)b\dot{\alpha} + U\alpha] \qquad (2.23) \end{aligned}$$

where $T(\bar{s})$ represents the complex Theodorsen function. $\bar{s} = b\omega i/U$ is a Laplace operator associated with non dimensional time Ut/b. The effects of aerodynamics on the store are however neglected to make the analysis simpler.

2.4 Normalized Equations of Motion

Substituting Eqs. (2.22-2.23) and Eqs. (2.19-2.21) into Eqs. (2.6-2.8) and dividing the first of the resulting equation on both sides by $\pi\rho b^2$ and the second and third equations by $\pi\rho b^4$, the following simplified matrix notation in the Laplace domain can be written as

$$(\boldsymbol{M_s}s^2 + \boldsymbol{K_s})\boldsymbol{q}(s) = [\underbrace{-s^2\boldsymbol{M_{nc}} - s\boldsymbol{C_{nc}}}_{non-circulatory} + \underbrace{T(\bar{s})(s\boldsymbol{C_c} + \boldsymbol{K_c})}_{circulatory}]\boldsymbol{q}(s) + \boldsymbol{H}u(s) \tag{2.24}$$

where

$$\boldsymbol{q}(s) = \begin{Bmatrix} h/b & \alpha & \theta \end{Bmatrix}^T$$

is a vector of generalized coordinates in which the plunge motion (h) of the airfoil is non-dimensionalized by its semi-chord length (b) to enable easy comparison with the pitching motions. The left hand side of Eq. (2.24) consists of the mass and elastic terms of the airfoil, the actuator and the attached store and are given as

$$\boldsymbol{M_s} = \begin{bmatrix} \mu_w + \mu_s + \mu_a & \mu_w x_\alpha + \mu_s(x_\theta - \ell_2) + \mu_a\ell_1 & \mu_s x_\theta + \frac{1}{2}\mu_a\ell_1 \\ \mu_w x_\alpha + \mu_s(x_\theta - \ell_2) + \mu_a\ell_1 & \mu_w r_\alpha^2 + \mu_s(r_\theta^2 + \ell_2^2 - 2x_\theta\ell_2) + \mu_a\ell_1^2 & \mu_s(r_\theta^2 - x_\theta\ell_2) + \frac{1}{2}\mu_a\ell_1^2 \\ \mu_s x_\theta + \frac{1}{2}\mu_a\ell_1 & \mu_s(r_\theta^2 - x_\theta\ell_2) + \frac{1}{2}\mu_a\ell_1^2 & \mu_s r_\theta^2 + \frac{1}{3}\mu_a\ell_1^2 \end{bmatrix}$$

$$\boldsymbol{K_s} = \begin{bmatrix} \mu_w\omega_h^2 & 0 & 0 \\ 0 & \mu_w r_\alpha^2\omega_\alpha^2 & 0 \\ 0 & 0 & \mu_s r_\theta^2\omega_\theta^2 \end{bmatrix} \tag{2.25}$$

where $\mu_w = m_w/\pi\rho b^2, \mu_s = m_s/\pi\rho b^2$ and $\mu_a = m_a L_a/\pi\rho b^2$ are the virtual masses of the wing, store and the actuator respectively. Recall that $\mu_s r_\theta^2\omega_\theta^2$ is the normalized version of K_θ of Eq. (2.8) (normalized by $\pi\rho b^4$) providing restoring moment to the store and is equal to $(EA_a/L_a)\ell_1^2/\pi\rho b^2$. This term should be such that it satisfies the Reed's criterion, that is, the ratio of the store pitch to wing bending frequency should always be less than 1 for effective store flutter alleviation. The right side of Eq. (2.24) is a result of Edwards [27] work in which he extended Theodorsen's generalized unsteady aerodynamic theory (which was

based on simple harmonic oscillations) to include arbitrary motions. His generalized unsteady aerodynamic theory divides the aerodynamic loads into non-circulatory and circulatory parts as shown in Eq. (2.24) where $\boldsymbol{M_{nc}}$ and $\boldsymbol{C_{nc}}$ are apparent additional mass and damping matrices due to non-circulatory oscillations of the aerodynamic loads given by

$$\boldsymbol{M_{nc}} = \begin{bmatrix} 1 & -a & 0 \\ -a & a^2 + \frac{1}{8} & 0 \\ 0 & 0 & 0 \end{bmatrix} \qquad \boldsymbol{C_{nc}} = \frac{U}{b} \begin{bmatrix} 0 & 1 & 0 \\ 0 & \frac{1}{8} - a & 0 \\ 0 & 0 & 0 \end{bmatrix} \tag{2.26}$$

Matrices $\boldsymbol{C_c}$ and $\boldsymbol{K_c}$ are the Laplace transform of the circulatory part of the unsteady aerodynamics loads and are given by

$$\boldsymbol{C_c} = \begin{bmatrix} -2 & -2(0.5 - a) & 0 \\ 2(0.5 + a) & 2(0.5^2 - a^2) & 0 \\ 0 & 0 & 0 \end{bmatrix} \qquad \boldsymbol{K_c} = \begin{bmatrix} 0 & -2 & 0 \\ 0 & 2(0.5 + a) & 0 \\ 0 & 0 & 0 \end{bmatrix} \tag{2.27}$$

The term u represents the actuator input (control moment to the store) acting through the input matrix $\boldsymbol{H} = [0\ 0\ 1]^T$ due to the components of the generalized actuator forces and moments $Q_{act-h}, Q_{act-\alpha}$ and $Q_{act-\theta}$ given in Eqs. (2.6-2.8). Actually u is equal to $-\mathcal{F}(\psi)\bar{V}\ell_1 b/(\pi\rho b^2)$ where $\mathcal{F}(\psi)$ involves parameter such as piezoelectric constant d_{31}, permitivity, effective radius of the bender elements, the thickness of the wafer plates, etc [23].

2.5 State-Space Representation

Numerical implementation of most of the modern advanced control laws often require the plant model to be in state-space form. The Theodorsen's function present in the above equations involves complex Bessel's function which makes the equations infinite dimensional. The following is a standard procedure [27] to convert the infinite dimensional aeroelastic plant describing typical section wing in an incompressible flow, into a finite dimensional one (and subsequently to state-space form) using Jones' approximation to the Theodorsen function.

Matrices $\boldsymbol{C_c}$ and $\boldsymbol{K_c}$ corresponding to the circulatory part are further sub divided into

$$T(\bar{s})[s\boldsymbol{C_c} + \boldsymbol{K_c}] = T(\bar{s})\boldsymbol{R}[s\boldsymbol{S_2} + \boldsymbol{S_1}] \tag{2.28}$$

where

$$\boldsymbol{R} = \begin{bmatrix} -2 \\ 2(a+0.5) \\ 0 \end{bmatrix} \quad \boldsymbol{S_1} = \begin{bmatrix} 0 & 1 & 0 \end{bmatrix} \quad \boldsymbol{S_2} = \begin{bmatrix} 1 & 0.5-a & 0 \end{bmatrix}$$

The complete equations of motion are recast into the form

$$\left\{s^2(\boldsymbol{M_s} + \boldsymbol{M_{nc}}) + s\boldsymbol{C_{nc}} + \boldsymbol{K_s}\right\}\boldsymbol{q}(s) = T(\bar{s})\boldsymbol{R}[s\boldsymbol{S_2} + \boldsymbol{S_1}]\boldsymbol{q}(s) + \boldsymbol{H}u(s) + \boldsymbol{F}\boldsymbol{w}(s) \tag{2.29}$$

where the term $\boldsymbol{w}$ represents the free stream airflow disturbance acting through an identity matrix $\boldsymbol{F}$ while u represents the actuator input acting through the input matrix $\boldsymbol{H} = [0\ 0\ 1]^T$. To complete the model in the Laplace domain, Jones' [28] second order rational approximation to the complex Theodorsen function is used and is given by

$$T(\bar{s}) = \frac{0.5(\frac{sb}{U})^2 + 0.2808(\frac{sb}{U}) + 0.01365}{(\frac{sb}{U})^2 + 0.3455(\frac{sb}{U}) + 0.01365} \tag{2.30}$$

A non-unique state-space representation of Jones' approximation for unsteady circulatory aerodynamic loads can be obtained as

$$\left[\begin{array}{c|c} \boldsymbol{A_2} & \boldsymbol{B_2} \\ \hline \boldsymbol{C_2} & \boldsymbol{D_2} \end{array}\right] = \left[\begin{array}{cc|c} -0.3(\frac{U}{b}) & 0 & -1.2650(\frac{U}{b}) \\ 0 & -0.0455(\frac{U}{b}) & -0.4927(\frac{U}{b}) \\ \hline -0.0799 & -0.0151 & 0.5 \end{array}\right] \tag{2.31}$$

The state-space representation of the structural equations and non-circulatory components of the aerodynamic loads is given as

$$\left[\begin{array}{c|c} \boldsymbol{A_1} & \boldsymbol{B_1} \\ \hline \boldsymbol{C_1} & \boldsymbol{D_1} \end{array}\right] = \left[\begin{array}{cc|c} \boldsymbol{0} & \boldsymbol{I} & \boldsymbol{0} \\ -(\boldsymbol{M_s} + \boldsymbol{M_{nc}})^{-1}\boldsymbol{K_s} & -(\boldsymbol{M_s} + \boldsymbol{M_{nc}})^{-1}\boldsymbol{C_{nc}} & (\boldsymbol{M_s} + \boldsymbol{M_{nc}})^{-1}\boldsymbol{R} \\ \hline (\frac{U}{b})^2\boldsymbol{S_1} & (\frac{U}{b})\boldsymbol{S_2} & \boldsymbol{0} \end{array}\right] \tag{2.32}$$

From Eq. (2.30) it is evident that the circulatory aerodynamic loads introduce two additional states, called the "aerodynamic lags" (x_1, x_2), which increase the total number of states to eight. The state-space representation of the augmented system is given by

$$\begin{aligned} \dot{\boldsymbol{x}} &= \boldsymbol{A}\boldsymbol{x} + \boldsymbol{B}u + \boldsymbol{\Gamma}\boldsymbol{w} \\ \boldsymbol{y} &= \boldsymbol{C}\boldsymbol{x} + \boldsymbol{D}u \end{aligned} \tag{2.33}$$

where

$$\boldsymbol{x} = \left\{ h/b \quad \alpha \quad \theta \quad \dot{h}/b \quad \dot{\alpha} \quad \dot{\theta} \quad x_1 \quad x_2 \right\}^T$$

and

$$\left[\begin{array}{c|c} \boldsymbol{A} & \boldsymbol{B} \\ \hline \boldsymbol{\Gamma}^T & \boldsymbol{D} \end{array}\right] = \left[\begin{array}{cc|c} \boldsymbol{A_1} + \boldsymbol{B_1 D_2 C_1} & \boldsymbol{B_1 C_2} & \boldsymbol{B_0} \\ \boldsymbol{B_2 C_1} & \boldsymbol{A_2} & \boldsymbol{0} \\ \hline \boldsymbol{E} & \boldsymbol{0} & \boldsymbol{0} \end{array}\right]$$

where $\boldsymbol{B_0} = \left[\, \boldsymbol{0} \;\; \boldsymbol{(M_s + M_{nc})^{-1} H} \,\right]^{\boldsymbol{T}}$ and $\boldsymbol{E} = \left[\, \boldsymbol{0} \;\; \boldsymbol{(M_s + M_{nc})^{-1} F} \,\right]^{\boldsymbol{T}}$. The three primary outputs of interest are the plunging motion h, the wing pitch α and the store pitch angle θ.

2.6 Open-Loop Simulations

The parameters in Table 1 represent those of an F-16 aircraft carrying under each wing a GBU-8 bomb near the midspan mounted on a passive decoupler pylon. The airplane also had in addition, a AIM-9J wingtip missile, and external fuel tank on each wing [21]. For the current work, only the GBU-8/B store configuration is considered for simulation purposes ($\rho = 0.008256$ slug/ft^3). Figure 2.2 shows the bending-torsion frequency coalescence trend as a function of air speed. The figure illustrates the effectiveness of the decoupler pylon mounted wing/store system over a rigidly mounted store in increasing the flutter speed. The frequencies at ground speed are those due to undamped, inertially coupled wing/store system which are slightly reduced due to the apparent additional mass contributed by non-circulatory component of the aerodynamic loads (Eq. 2.29). As the flight speed is increased,

Table 2.1: Wing/store structural parameters

$m_s = 1027.6$ kg (2265 lb)	$x_\alpha b = 0.178$ m (7.04 in)
$m_w = 5.3 m_s$	$x_\theta b = 0$
$m_a L_a = 13.61$ kg (30 lb)	$\ell_1 b = 0.223$ m (8.8 in)
$r_\alpha b = 0.635$ m (25 in)	$\ell_2 b = 0.223$ m (8.8 in)
$r_\theta b = 0.830$ m (32.7 in)	$ab = -0.1702$ m (-6.68 in)
$b = 1.12$ m (44 in)	$\omega_h = 24.5$ rad/s
ω_θ/ω_h=0.55	$\omega_\alpha/\omega_h = 1.27$

the bending branch frequency for both rigid and the decoupler case remains approximately equal to its ground frequency, with a slight increase near the flutter speed. The first wing torsional mode frequency for the decoupler case, however, decreases relatively less than that corresponding to the rigid case because of the reduced store pitch inertia effects (due to the presence of soft-spring like actuator) and comes close to the bending branch near the flutter speed. The result is an increase in flutter speed for the decoupler mounted store system. These branches do not coalesce because of the presence of aerodynamic damping present in the system.

The open-loop flutter speed is therefore predicted exactly from the *V-g* plot by calculating the speed where dissipation energy changes sign. The variation of bending and torsional mode structural damping as a function of airspeed is shown in Fig. 2.3. It is observed that for both torsional and bending modes, the damping at first increases with air speed with the branch corresponding to bending mode increasing more rapidly than the torsional branch. At around 85 to 95% of the flutter speed, the torsional mode damping suddenly decreases and approaches zero at the flutter speed. The bending mode damping, however, continues to increase at a much faster rate. The open-loop flutter speed where the torsional mode damping changes sign is found to occur at $U/b = 170 sec^{-1}$ for decoupler case and $U/b = 127 sec^{-1}$ for rigid case. For comparison, the flutter speed for a clean wing (without any store) is found to be at $U/b = 148 sec^{-1}$. This represents a 14.86% increase

in flutter speed with decoupler pylon over that of a bare wing and a 33.86% increase over a rigidly attached case.

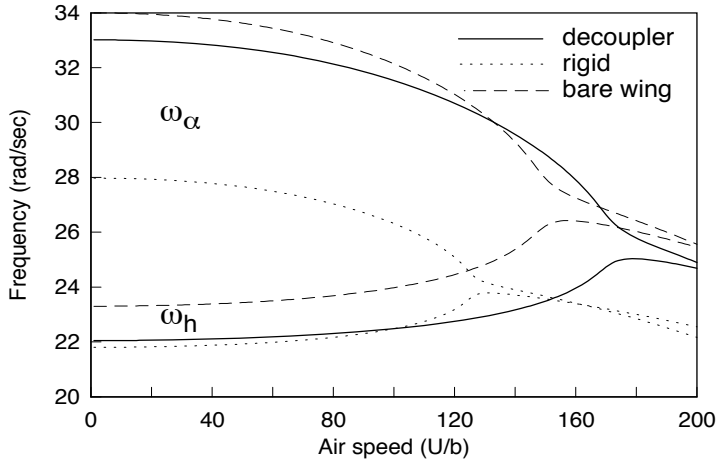

Figure 2.2: Bending-torsion frequency coalescence vs. air speed

2.7 Uncertainty Representation

The dynamics of any physical system can never be captured completely by mathematical models. There are always errors associated with the approximations made during the modeling process. These approximations are made either because of the lack of complete knowledge of the system or because of the difficulty in modeling. For instance, the plant described in previous section does not include actuator dynamics and aero loads on the store are neglected. These imprecisions in high frequency dynamics are termed as unstructured uncertainties that generally result in an under-estimation of the system order. Some of the other examples of unstructured uncertainties for wing/store flutter problem are the errors from ignoring rigid body modes of the aircraft.

Uncertainties can also be parametric in nature where the parameters fluctuate slowly

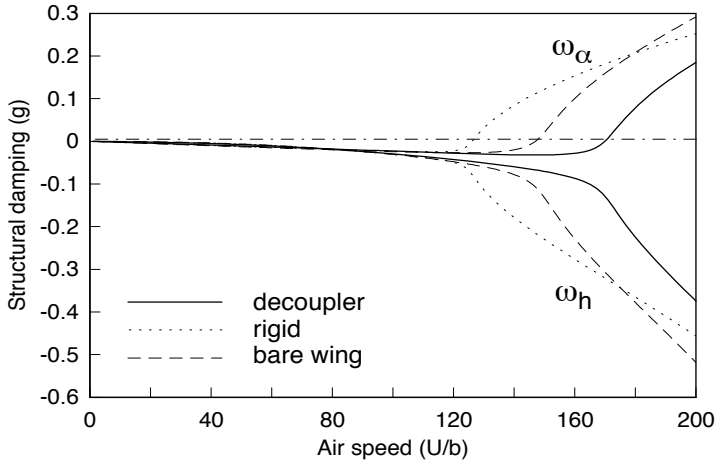

Figure 2.3: Structural damping vs. air speed

between known values. These low frequency perturbations are called as structured uncertainties. In the case of wing/store flutter problem, they are common in situations of combat when center of gravity location and radius of gyration of the store vary with various rigid body maneuvers. Hence during the design of an appropriate controller, the robustness of the closed-loop system in the face of these uncertainties and maintenance of its nominal performance are therefore the primary objectives of any control strategy.

In robust control literature, the mathematical representation of uncertainties caused by such unintentional exclusion of high frequency dynamics, generally take many form [29], of which the most commonly used is the multiplicative uncertainty model. Depending on where the errors are reflected with respect to the plant, they are further classified into input and output multiplicative uncertainties. In a narrow sense, using these equivalent input and output multiplicative uncertainties imply an imperfect set of actuators and sensors respectively. In a broader sense, any plant uncertainty can be "referred" to its input or output. This is because the source of unstructured uncertainties is not generally known, and therefore an equivalent input or output uncertainty can be used to characterize the total plant uncertainty.

If $\Delta_m(s)$ represents a proper and stable approximation transfer function error, then the plant transfer function $[Q(s)]$ from u to y_1 (Fig. 2.4) perturbed with an input multiplicative uncertainty model is given by:

$$Q^*(s) = Q(s)[1 + \Delta_m(s)] \tag{2.34}$$

Similarly the plant perturbed with an output multiplicative uncertainty model $\Delta_m(s)$ is given by:

$$Q^*(s) = [1 + \Delta_m(s)]Q(s) \tag{2.35}$$

For simulation and analysis purposes, an approximate model of uncertainty is constructed based on the error from neglecting store aerodynamics.

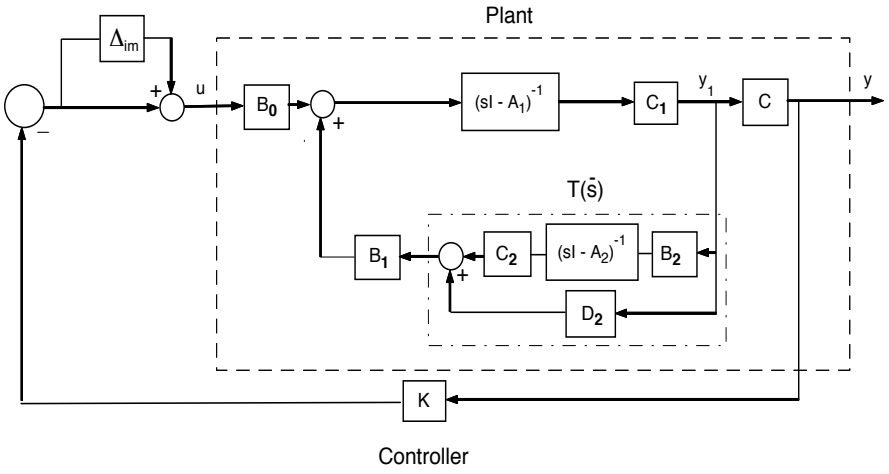

Figure 2.4: Block diagram of active flutter suppression

It is derived based on the argument that had the store aerodynamics been included then the circulatory aerodynamics of wing and store combination (as opposed to that of the wing alone as in Eq. 2.28) can be approximated by Eq. (2.28), with the exception that the Jones' rational function be replaced by some Jones'-like transfer function that closely captures the circulatory effects due to wing/store combination aerodynamics. In

other words, the uncertainty in store aerodynamics is reflected on to the uncertainty in Jones' rational function approximation. For simulation purposes, it is assumed that the Jones' approximation $[T(\bar{s})]$ be replaced with a Jones'-like rational approximation $[T^*(\bar{s})]$ whose frequency response characteristics are shown in Fig. 2.5. where

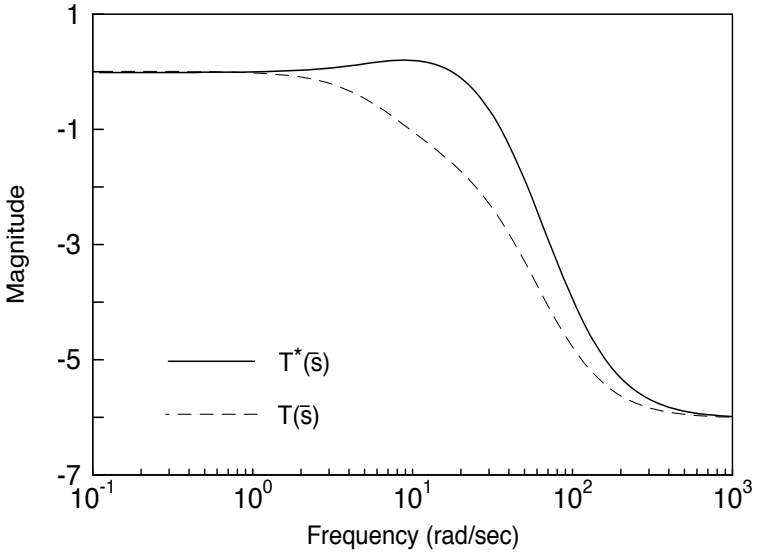

Figure 2.5: Jones' approximations

$$T^*(\bar{s}) = \frac{0.5(\frac{sb}{U})^2 + 0.3398(\frac{sb}{U}) + 0.013627}{(\frac{sb}{U})^2 + 0.3455(\frac{sb}{U}) + 0.01365} \tag{2.36}$$

It is assumed that the majority of the difference between the magnitudes occur in the mid to high frequency range. It is to be noted that $T^*(\bar{s})$ is picked only for simulation purposes and lacks any physical backing. However, the motivating argument still remains valid. That is, some other rational function may replace the Jones' approximation that closely represents the circulatory aero loads around wing-store combination. The aim here is to construct an approximate uncertainty model $\Delta_m(s)$ to reflect the error in store aerodynmaics that is later used to perturb the closed-loop system to evaluate for its robustness to modeling limitations. The following details the construction of an uncertainty model $\Delta_m(s)$ from the block diagram shown in Fig. 2.4.

This block diagram re-iterates the fact that flutter is a self-excited phenomenon occuring primarily due to the circulatory aerodynamic loads being regeneratively fed back

into the system. Using the Jones' approximation to the Theodorsen's function, the transfer function from u to y_1 can be represented as

$$\begin{aligned} Q(s) &= \frac{\boldsymbol{C_1}[s\boldsymbol{I} - \boldsymbol{A_1}]^{-1}\boldsymbol{B_0}}{1 - \boldsymbol{C_1}[s\boldsymbol{I} - \boldsymbol{A_1}]^{-1}\boldsymbol{B_1}T(\bar{s})} \\ &= \frac{N_0(s)/M(s)}{1 - T(\bar{s})N_1(s)/M(s)} \end{aligned} \tag{2.37}$$

Let the actual plant's transfer function (obtained by using Jones-like approximation) be given by

$$\begin{aligned} Q^*(s) &= \frac{\boldsymbol{C_1}[s\boldsymbol{I} - \boldsymbol{A_1}]^{-1}\boldsymbol{B_0}}{1 - \boldsymbol{C_1}[s\boldsymbol{I} - \boldsymbol{A_1}]^{-1}\boldsymbol{B_1}T^*(\bar{s})} \\ &= \frac{N_0(s)/M(s)}{1 - T^*(\bar{s})N_1(s)/M(s)} \end{aligned} \tag{2.38}$$

Using the input multiplicative uncertainty the true plant can be expressed in terms of the nominal plant as

$$\frac{N_0(s)}{M(s) - N_1(s)T^*(\bar{s})} = \frac{N_0(s)}{M(s) - N_1(s)T(\bar{s})}[1 + \Delta_m(s)] \tag{2.39}$$

The uncertainty model $\Delta_m(s)$ can now be written as

$$\Delta_m(s) = \frac{N_1(s)[T^*(\bar{s}) - T(\bar{s})]}{M(s) - N_1(s)T^*(\bar{s})} \tag{2.40}$$

which remains the same when an output multiplicative uncertainty model is considered. Because the control theory [29] requires that $\Delta_m(s)$ be stable, the uncertainty model is designed at a flight speed of $0.9U_f$, which is in the sub-critical flutter region.

2.8 Summary

In this chapter, the equations of motion for flutter of wing/store-strut combination were derived based on Lagrange's equations. For the structural part, three degrees-of-freedom were utilized, namely, the wing bending, wing torsion and store pitch relative to the wing. Typical section formulation is used to model the wing where structural damping is

neglected. Two-dimensional, incompressible unsteady flow model is used for the wing aerodynamics and the store aerodynamics is ignored. Jones' rational function approximation is used approximate the Theodorsen's function and the resulting structural-aerodynamic equations are reformulated in normalized state-variable form. Because of the Jones' 2nd order rational function approximation, the state-space equations developed yielded two additional states. The structural parameters of an F-16 aircraft carrying a bomb near midspan have been used to simulate the open-loop flutter model.

A multiplicative uncertainty model is also developed based on the assumption that the circulatory aerodynamic loads around the wing-store combination can be approximately modeled by an approximate Jones'-like rational function. The rationale behind this is to have an approximate analytical model to represent the uncertainty that could be then used to perturb the plant to analyse the robust stability properties of the designed closed-loop control systems of Chapters 3, 4 and 5.

Chapter 3

Linear Quadratic Controller Design

In this chapter linear optimal control laws are used to design controllers for the single input multi-output linear time invariant wing/store aeroelastic system of equations derived earlier. In particular a robust LQG/LTR design technique is used to achieve the best trade-off between nominal performance and robust stability of the closed-loop system. Sections 3.1 and 3.2 describe the steps involved in the design of such a controller. First a Linear Quadratic Regulator (LQR) is designed which relies on the basic premise that all the states are available for feedback. The states are then estimated using Kalman-Bucy filter and a LQG controller is designed for the wing/store open-loop plant. Comparing the drawbacks of the LQG design and the current requirements, LTR design procedure (Section 3.2.1) is illustrated. Section 3.3 presents the results and discussion of the numerical simulation followed by the summary of this chapter in Section 3.4.

3.1 Linear Quadratic Regulator (LQR)

The first step in the LQR design is to augment the plant with integrators at the three output channels to ensure zero steady-state tracking errors. The external disturbance term

introduced in Eq. (2.29) can be used for this purpose by defining a dynamic model as

$$\begin{aligned} \dot{\boldsymbol{d}} &= \boldsymbol{A_I d} + \boldsymbol{B_I v} \\ \boldsymbol{w} &= \boldsymbol{C_I d} + \boldsymbol{D_I v} \end{aligned} \tag{3.1}$$

where the output $\boldsymbol{w}$ is an external input into the system as in Eq. (2.29), $\boldsymbol{A_I} = \boldsymbol{0_3}$, $\boldsymbol{B_I} = \boldsymbol{I_3}$, $\boldsymbol{C_I} = \boldsymbol{I_3}$ and $\boldsymbol{D_I} = \boldsymbol{0_3}$. The complete state-space equations augmented with the disturbance model for the LQR design are given by

$$\begin{aligned} \dot{\boldsymbol{x}}_{\boldsymbol{a}} &= \boldsymbol{A_a x_a} + \boldsymbol{B_a} u + \boldsymbol{\Gamma_a v} \\ \boldsymbol{y_a} &= \boldsymbol{C_a x_a} + \boldsymbol{n} \end{aligned} \tag{3.2}$$

where

$$\left[\begin{array}{c|c} \boldsymbol{A_a} & \boldsymbol{B_a} \\ \hline \boldsymbol{C_a} & \boldsymbol{D_a} \end{array}\right] = \left[\begin{array}{cc|c} \boldsymbol{A} & \boldsymbol{\Gamma C_I} & \boldsymbol{B} \\ \boldsymbol{0} & \boldsymbol{A_I} & \boldsymbol{0} \\ \hline \boldsymbol{C} & \boldsymbol{0} & \boldsymbol{0} \end{array}\right]$$

The optimal regulator problem is to find a control input $u(t)$ defined on $[0, \infty]$ which drives the states $\boldsymbol{x_a}(t)$ to zero in an arbitrarily short time. The optimal full-state feedback gain required to achieve this task is obtained by minimizing a scalar performance index

$$J = \frac{1}{2} \int_0^\infty (\boldsymbol{x_a^T Q_c x_a} + u^T R_c u) dt \tag{3.3}$$

where the positive definite matrix $\boldsymbol{Q_c}$ represents the penalty on the states and R_c is a weighting that penalizes the control effort. Minimization is achieved by solving the steady-state Algebraic Riccati Equation (ARE) for a semi-positive definite matrix $\boldsymbol{P}$.

$$\boldsymbol{0} = \boldsymbol{A_a^T P} + \boldsymbol{P A_a} - \boldsymbol{P B_a} R_c^{-1} \boldsymbol{B_a P} + \boldsymbol{Q_c} \tag{3.4}$$

The final optimal gain matrix is then given by

$$\boldsymbol{K_c} = R_c^{-1} \boldsymbol{B_a^T P} \tag{3.5}$$

and the required control input $u(t)$ is equal to $-\boldsymbol{K_c x_a}(t)$.

3.2 Linear Quadratic Gaussian (LQG)

Slow variations of store parameters such as mass and the center of gravity location are quite common during maneuvers of a high performance military aircraft. While the LQR design provides a controller robust enough to withstand such low frequency parameter changes, the unavailability of all states for feedback makes the design impractical.

As an alternative, a Linear Quadratic Gaussian (LQG) design which uses noise corrupted outputs for feedback is used as a controller. The practicality of the LQG design also lies in the assumption that the uncertainty is represented as an additive white noise. The state-space representation of the plant augmented with process and measurement noises for the LQG design are given in Eq. (3.2), where

$$\boldsymbol{\Gamma}_{\boldsymbol{a}} = \begin{bmatrix} \boldsymbol{\Gamma D_I} \\ \boldsymbol{B_I} \end{bmatrix}$$

It is assumed that additive process noise $\boldsymbol{v}$ and the measurement noise $\boldsymbol{n}$ are uncorrelated zero-mean, Gaussian, white-noise processes with correlation matrices

$$\begin{aligned} \boldsymbol{E}[\boldsymbol{v}\boldsymbol{v}^{\boldsymbol{T}}] &= \boldsymbol{Q_f}\boldsymbol{\delta}(t-\tau) \\ \boldsymbol{E}[\boldsymbol{n}\boldsymbol{n}^{\boldsymbol{T}}] &= \boldsymbol{R_o}\boldsymbol{\delta}(t-\tau) \end{aligned} \tag{3.6}$$

where $\boldsymbol{R_o}$ is assumed to be a positive definite matrix and $\boldsymbol{Q_f}$ is allowed to be a positive semi-definite matrix.

To obtain the estimates $\widehat{\boldsymbol{x}}_{\boldsymbol{a}}$ of the states $\boldsymbol{x_a}(t)$ under noisy measurements, the variance of the error $\widetilde{\boldsymbol{x}}_{\boldsymbol{a}}(t) = \boldsymbol{x_a}(t) - \widehat{\boldsymbol{x}}_{\boldsymbol{a}}(t)$ given by $J_e = E[\widetilde{\boldsymbol{x}}_{\boldsymbol{a}}^{\boldsymbol{T}}(t)\widetilde{\boldsymbol{x}}_{\boldsymbol{a}}(t)]$ is minimized. Under the standard assumptions that the pair $(\boldsymbol{A_a}, \boldsymbol{B_a})$ is stabilizable and $(\boldsymbol{C_a}, \boldsymbol{A_a})$ is detectable the state-space representation for the Kalman filter is given by

$$\dot{\widehat{\boldsymbol{x}}}_{\boldsymbol{a}} = \boldsymbol{A_a}\widehat{\boldsymbol{x}}_{\boldsymbol{a}} + \boldsymbol{B_a}u + \boldsymbol{K_e}(\boldsymbol{y_a} - \boldsymbol{C_a}\widehat{\boldsymbol{x}}_{\boldsymbol{a}}) \tag{3.7}$$

The Filter Algebraic Riccati Equation (FARE) needed to solve for the estimation error

covariance $\boldsymbol{\Sigma}$ is given by

$$\mathbf{0} = \boldsymbol{A}_a^T\boldsymbol{\Sigma} + \boldsymbol{\Sigma}\boldsymbol{A}_a - \boldsymbol{\Sigma}\boldsymbol{C}_a^T\boldsymbol{R}_o^{-1}\boldsymbol{C}_a\boldsymbol{\Sigma} + \underbrace{\boldsymbol{\Gamma}_a Q_o \boldsymbol{\Gamma}_a^T}_{\boldsymbol{Q}_f} \tag{3.8}$$

The Kalman filter gain matrix is then given by

$$\boldsymbol{K}_e = \boldsymbol{\Sigma}\boldsymbol{C}_a^T\boldsymbol{R}_o^{-1} \tag{3.9}$$

Using the separation principle [30], a controller based on a cascade realization [31] is synthesized. The state-space matrices of the resulting closed-loop system is given by

$$\left[\begin{array}{c|c} \boldsymbol{A}_{cl} & \boldsymbol{B}_{cl} \\ \hline \boldsymbol{C}_{cl} & \boldsymbol{D}_{cl} \end{array}\right] = \left[\begin{array}{cc|c} \boldsymbol{A} & -\boldsymbol{B}\boldsymbol{K}_c & \boldsymbol{B} \\ \boldsymbol{K}_e\boldsymbol{C} & \boldsymbol{A}_a - \boldsymbol{B}_a\boldsymbol{K}_c - \boldsymbol{K}_e\boldsymbol{C}_a & \mathbf{0} \\ \hline \boldsymbol{C} & \mathbf{0} & \mathbf{0} \end{array}\right]$$

Tuning parameters $\boldsymbol{Q_c}$, R_c, Q_o and $\boldsymbol{R_o}$ can be adjusted until a satisfactory design is obtained. Here the loop is assumed to be broken at the input to reflect all the uncertainties at the input of the plant. This is equivalent to the assumption of an imperfect actuator.

Although the LQG design is more practical because it involves the estimation of unknown states, and has the ability to withstand errors due to unstructured uncertainties, it does not however have the desired properties of LQR, namely good nominal performance. To obtain a design that is tolerant of modeling errors and maintains a satisfactory nominal performance, a robust loop shaping technique called the Loop Transfer Recovery (LTR) is used.

3.2.1 Loop Transfer Recovery (LTR)

This technique [30] involves tuning the Kalman filter to recover the stability margins associated with full-state feedback design. The Kalman filter in the LQG technique was designed assuming that it had accurate knowledge of the input. But in reality, the input has uncertainties (due to unmodeled actuator dynamics) that may not allow the Kalman

filter to perfectly estimate the states. Hence to achieve a perfect estimation of states for input uncertainties, the Kalman filter is re-designed by adding fictitious noise on the input through $\boldsymbol{B_a}$ matrix resulting in a modified process noise intensity

$$\boldsymbol{Q_f} = \boldsymbol{\Gamma}_a Q_o \boldsymbol{\Gamma}_a^{\boldsymbol{T}} + m_f^2 \boldsymbol{B_a} \boldsymbol{B_a^T} \tag{3.10}$$

There is however no change in the measurement noise weighting that is equal to its original intensity $\boldsymbol{R_o}$. When $m_f = 0$ the original Kalman filter of Eq. (3.9) is obtained. To briefly examine the effect of increasing the value of m_f to infinity, the modified FARE equation is first written as

$$\begin{aligned}
\mathbf{0} &= \boldsymbol{A_a}^{\boldsymbol{T}}\boldsymbol{\Sigma} + \boldsymbol{\Sigma}\,\boldsymbol{A_a} - \boldsymbol{\Sigma}\boldsymbol{C_a}^{\boldsymbol{T}}\boldsymbol{R_o}^{-\mathbf{1}}\boldsymbol{C_a}\boldsymbol{\Sigma} + \boldsymbol{\Gamma}_a Q_o \boldsymbol{\Gamma_a}^{\boldsymbol{T}} + m_f^2 \boldsymbol{B_a}\boldsymbol{B_a}^{\boldsymbol{T}} \\
\mathbf{0} &= \frac{1}{m_f^2}(\boldsymbol{A_a}^{\boldsymbol{T}}\boldsymbol{\Sigma} + \boldsymbol{\Sigma}\,\boldsymbol{A_a} + \boldsymbol{\Gamma}_a Q_o \boldsymbol{\Gamma_a}^{\boldsymbol{T}}) + \boldsymbol{B_a}\boldsymbol{B_a}^{\boldsymbol{T}} - m_f^2\left[\frac{\boldsymbol{\Sigma}}{m_f^2}\boldsymbol{C_a}^{\boldsymbol{T}}\boldsymbol{R_o}^{-\mathbf{1}}\boldsymbol{C_a}\frac{\boldsymbol{\Sigma}}{m_f^2}\right]
\end{aligned}$$

As m_f tends to infinity, the first three terms become small and

$$\begin{aligned}
m_f^2\left[\frac{\boldsymbol{\Sigma}}{m_f^2}\boldsymbol{C_a}^{\boldsymbol{T}}\boldsymbol{R_o}^{-\mathbf{1}}\boldsymbol{C_a}\frac{\boldsymbol{\Sigma}}{m_f^2}\right] &\longrightarrow \boldsymbol{B_a}\boldsymbol{B_a}^{\boldsymbol{T}} \\
\frac{1}{m_f^2}(\boldsymbol{\Sigma}\boldsymbol{C_a}^{\boldsymbol{T}}\boldsymbol{R_o}^{-\mathbf{1}})\boldsymbol{R_o}(\boldsymbol{\Sigma}\boldsymbol{C_a}^{\boldsymbol{T}}\boldsymbol{R_o}^{-\mathbf{1}})^T &\longrightarrow (\boldsymbol{B_a}\boldsymbol{R_o}^{\frac{\mathbf{1}}{\mathbf{2}}})\boldsymbol{R_o}(\boldsymbol{B_a}\boldsymbol{R_o}^{-\frac{\mathbf{1}}{\mathbf{2}}})^{\boldsymbol{T}}
\end{aligned}$$

and from Eq. (3.9)

$$\frac{\boldsymbol{K_e}}{m_f} \longrightarrow \boldsymbol{B_a}\boldsymbol{R_o}^{-\frac{\mathbf{1}}{\mathbf{2}}} \text{ as } m_f \longrightarrow \boldsymbol{\infty} \tag{3.11}$$

From Fig. 3.1, the loop gain of the LQG system is given by

$$\begin{aligned}
\hat{\boldsymbol{x}} \;=\; & \boldsymbol{\Phi}\Big[\boldsymbol{B_a}(\boldsymbol{C_a}\boldsymbol{\Phi}\boldsymbol{B_a})^{-\mathbf{1}} - \boldsymbol{K_e}(\boldsymbol{I} + \boldsymbol{C_a}\boldsymbol{\Phi}\boldsymbol{K_e})^{-\mathbf{1}}\Big]\boldsymbol{C_a}\boldsymbol{\Phi}\boldsymbol{B_a}u' \\
& + \boldsymbol{\Phi}\Big[\boldsymbol{K_e}(\boldsymbol{I} + \boldsymbol{C_a}\boldsymbol{\Phi}\boldsymbol{K_e})^{-\mathbf{1}}\Big]\boldsymbol{C_a}\boldsymbol{\Phi}\boldsymbol{B_a}u''
\end{aligned}$$

where $\boldsymbol{\Phi} = (s\boldsymbol{I} - \boldsymbol{A_a})^{-\mathbf{1}}$. Substituting Eq. (3.11) in the above expression and re-arranging

$$\begin{aligned}
\hat{\boldsymbol{x}} \;=\; & \boldsymbol{\Phi}\Big[\boldsymbol{B_a}(\boldsymbol{C_a}\boldsymbol{\Phi}\boldsymbol{B_a})^{-\mathbf{1}} - \frac{\boldsymbol{B_a}}{\sqrt{\boldsymbol{R_o}}}\Big(\frac{\boldsymbol{I}}{m_f} + \frac{\boldsymbol{C_a}\boldsymbol{\Phi}\boldsymbol{B_a}}{\sqrt{\boldsymbol{R_o}}}\Big)^{-\mathbf{1}}\Big]\boldsymbol{C_a}\boldsymbol{\Phi}\boldsymbol{B_a}u' \\
& + \boldsymbol{\Phi}\Big[\frac{\boldsymbol{B_a}}{\sqrt{\boldsymbol{R_o}}}\Big(\frac{\boldsymbol{I}}{m_f} + \frac{\boldsymbol{C_a}\boldsymbol{\Phi}\boldsymbol{B_a}}{\sqrt{\boldsymbol{R_o}}}\Big)^{-\mathbf{1}}\Big]\boldsymbol{C_a}\boldsymbol{\Phi}\boldsymbol{B_a}u''
\end{aligned}$$

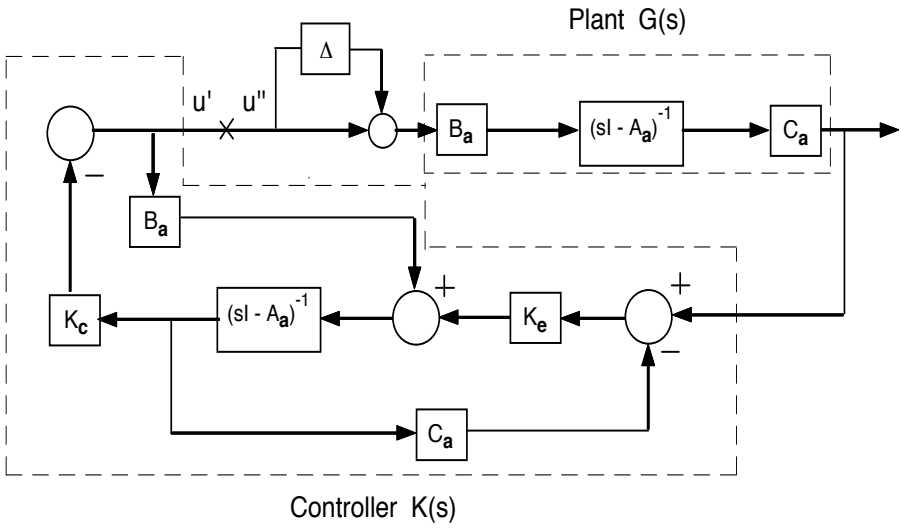

Figure 3.1: Block diagram of LQG based system

As $m_f \longrightarrow \infty$, $(\boldsymbol{I}/m_f) \longrightarrow 0$, and hence

$$\begin{aligned}\hat{\boldsymbol{x}} &= \boldsymbol{\Phi}\Big[\boldsymbol{B_a}(\boldsymbol{C_a}\boldsymbol{\Phi}\boldsymbol{B_a})^{-1} - \boldsymbol{B_a}(\boldsymbol{C_a}\boldsymbol{\Phi}\boldsymbol{B_a})^{-1}\Big]\boldsymbol{C_a}\boldsymbol{\Phi}\boldsymbol{B_a}u' + \boldsymbol{\Phi}\Big[\boldsymbol{B_a}(\boldsymbol{C_a}\boldsymbol{\Phi}\boldsymbol{B_a})^{-1}\Big]\boldsymbol{C_a}\boldsymbol{\Phi}\boldsymbol{B_a}u'' \\ &= \boldsymbol{\Phi}\boldsymbol{B_a}(\boldsymbol{C_a}\boldsymbol{\Phi}\boldsymbol{B_a})^{-1}(\boldsymbol{C_a}\boldsymbol{\Phi}\boldsymbol{B_a})u'' \\ &= \boldsymbol{\Phi}\boldsymbol{B_a}u''\end{aligned}$$

Therefore the loop gain of the modified LQG system becomes

$$\text{Loop gain} = \boldsymbol{K_c}\boldsymbol{\Phi}\boldsymbol{B_a}$$

which is equal to that of the LQR. Thus as the fictitious noise intensity coefficient m_f is increased, the loop properties of the observer-based system approach that of the LQR design. But if the measurements are much noisier than expected (as indicated by $\boldsymbol{R_o}$), then the Kalman filter would produce noise corrupted estimated states and therefore would suffer inaccuracy. Thus there is always a trade-off between filter accuracy and loop recovery.

3.3 Simulation Results

The values used for simulation purposes are $\boldsymbol{Q_c} = \text{diag}(10^7[1.7, 0.7, 0.03, 0, \ldots, 0])$, $R_c = 2.2 \times 10^{-4}$, $Q_o = 10^4$ and $\boldsymbol{R_o} = \boldsymbol{I_3}$. An initial estimate for the state-to-control weighting ratios were based on Ref. [32]. The value of m_f is increased from 0, which corresponds to the LQG design, to 1×10^3 where the recovery process is stopped. This is based on comparison of the maximal control-input energy constraint of the LQG/LTR and $\mathcal{H}_\infty$ controller compensated systems (Chapter 4).

3.3.1 Robust Stability Analysis

A measure of robust stability is obtained by first assuming an input multiplicative uncertainty model as shown in Fig. 3.1. Here the uncertainty model $\Delta(s)$ is equal to $\Delta_m(s)$ as derived in Section 2.7 of Chapter 2. Applying small gain theorem [33] to the loop gives a singular value sufficiency test for stability robustness of a closed-loop system subjected to uncertainty due to unmodeled dynamics and is given by

$$\overline{\sigma}[\Delta(s)]\overline{\boldsymbol{\sigma}}[\boldsymbol{T_i}(s)] < 1 \tag{3.12}$$

where

$$\boldsymbol{T_i}(s) = \frac{\boldsymbol{K}(s)\boldsymbol{G}(s)}{\boldsymbol{I} + \boldsymbol{K}(s)\boldsymbol{G}(s)}$$

is the input complementary sensitivity transfer matrix. Assuming the product of $\boldsymbol{K}$ and $\boldsymbol{G}$ to be non-singular, the stability condition can be re-written as

$$\sigma[\Delta(\omega)] < \underline{\boldsymbol{\sigma}}[\boldsymbol{I} + (\boldsymbol{K}(j\omega)\boldsymbol{G}(j\omega))^{-1}] \qquad \forall\omega \tag{3.13}$$

which gives percentage tolerance bounds for input multiplicative uncertainties. The frequency response of the robust stability margins for unstructured uncertainties is shown in Fig. 3.2. The absolute value of the minimum singular value of $[\boldsymbol{I} + (\boldsymbol{K}(j\omega)\boldsymbol{G}(j\omega))^{-1}]$ is

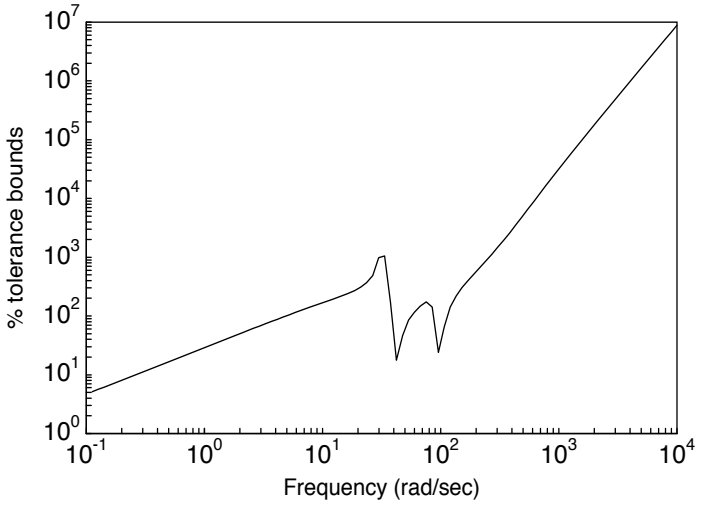

Figure 3.2: Percentage stability margins vs. frequency

observed to be 13.44 dB, which implies that the closed-loop system is capable of withstanding at least ± 235% plant uncertainty (with errors reflected at the input), without being destabilized. At the flutter frequency (25 rad/sec), the magnitude of the stability margin is observed to be ± 350% where the closed-loop system is required to alleviate the effects of modeling limitations, such as those caused by wing/store aerodynamic and other flutter critical uncertainties. For frequencies beyond 25 rad/sec, the percentage tolerance bounds increase monotonically with the increase in frequency. Large endurance margins are necessary at such frequencies where the effects of ignoring the aileron degree-of-freedom and other flexible modes including sensor and actuator dynamics are prominent.

To test the effectiveness of the controller in sustaining any errors caused by unmodeled dynamics, the input multiplicative model developed earlier (Eq. 2.40) is used to perturb the system and the resulting step responses are calculated. A representative time response of the output α is shown in Fig. 3.3. Clearly the closed-loop withstands and stabilizes the perturbation whereas the open-loop system response diverges leading to instability.

As mentioned earlier, the value of m_f for LQG/LTR design was selected based on comparison of the maximal control-input energy constraint of the LQG/LTR and $\mathcal{H}_\infty$ con-

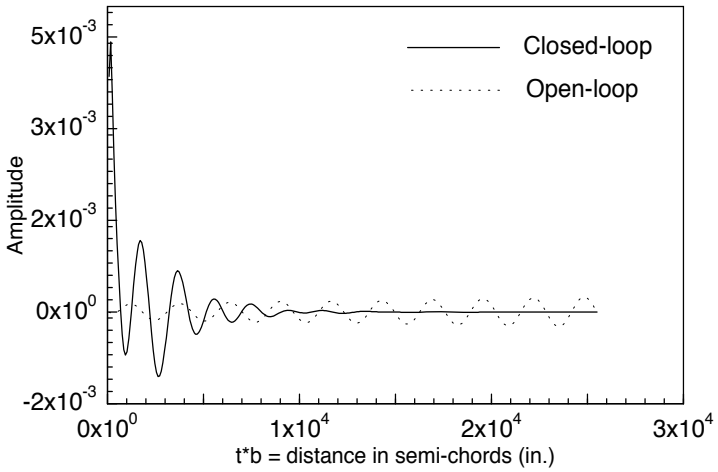

Figure 3.3: Step response of the perturbed open- and closed-loop systems (output α)

troller compensated systems. Incidentally, by assuming an additive uncertainty to the loop of the Fig. 3.1 and applying the small gain theorem, a sufficient condition for robust stability for additive modeling errors can be obtained which also is a measure of maximum control-input energy [34]. It is given by

$$\overline{\sigma}[\Delta]\overline{\boldsymbol{\sigma}}\left[\frac{\boldsymbol{K}}{\boldsymbol{I}+\boldsymbol{KG}}\right] < 1 \tag{3.14}$$

If $\boldsymbol{K}(j\omega)$ is non-singular at each frequency ω, then the tolerance bounds for additive uncertainty can be plotted from the condition

$$\overline{\sigma}[\Delta(j\omega)] < \underline{\boldsymbol{\sigma}}[\boldsymbol{G}(j\omega) + \boldsymbol{K^{-1}}(j\omega)] \qquad \forall\omega \tag{3.15}$$

Figure 3.4 shows the additive bounds for LQG/LTR and $\mathcal{H}_\infty$ compensated system. This forms the baseline for comparison of the results obtained with the use of LTR and $\mathcal{H}_\infty$ controllers.

The singular value Bode plot of controller transfer function is also given in Fig. 3.5. The controller has quite a large gain and bandwidth (1100 rad/sec). Although, large bandwidths are required to be able to withstand sudden fluctuations, they restrict the digital

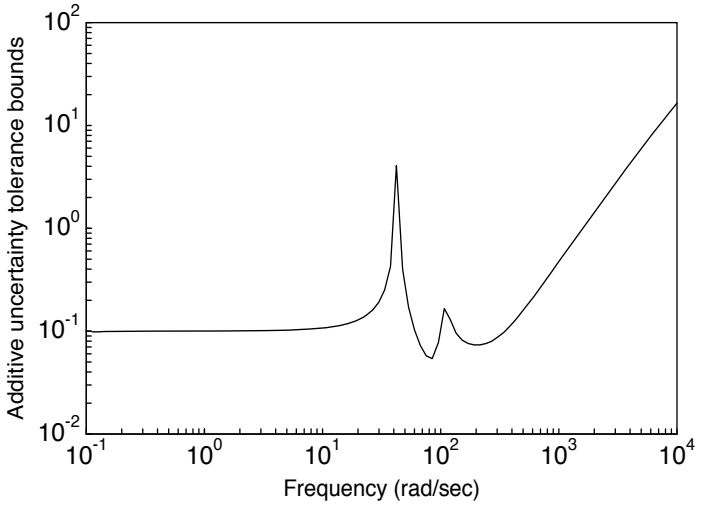

Figure 3.4: Additive uncertainty tolerance bounds

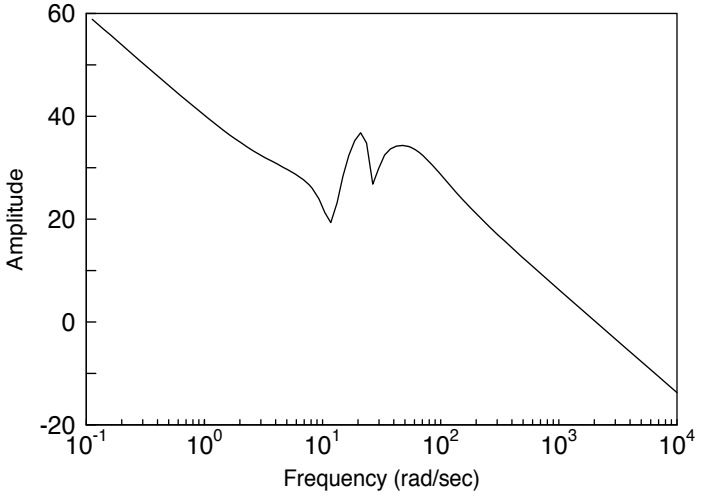

Figure 3.5: Controller transfer function

implementation and may be potentially dangerous to the actuators for the fear of saturation. They may also unnecessarily excite unwanted higher modes.

3.3.2 Nominal Performance Analysis

For nominal performance analysis, the controller is designed at sub-critical flutter speed ($0.9U_f$) with an intention of comparing the open-loop passive decoupler pylon mounted wing/store system responses with those of the closed-loop to assess the effectiveness of the active system. A step response of the output h for open- and closed-loop systems are compared in Fig. 3.6. Clearly the closed-loop system's output has better response than open-loop

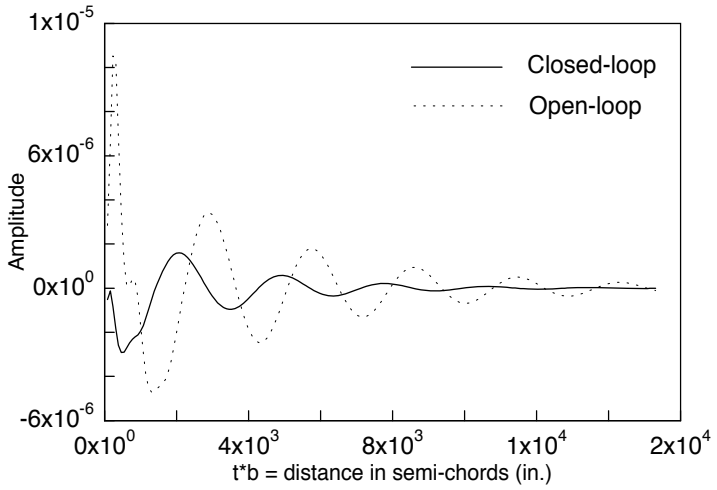

Figure 3.6: Step response (output h)

system's output in terms of smaller amplitude of the transient response and faster settling time. A singular value plot of the transfer matrix from sensor noise to plant outputs is shown in Fig. 3.7. Clearly all the three outputs attenuate external noises satisfactorily.

Another performance measure used to evaluate the effectiveness of the closed-loop system is the frequency response of the transfer function from the disturbance input (entering at the input of the plant) to the outputs. One example is the gust disturbance which typically

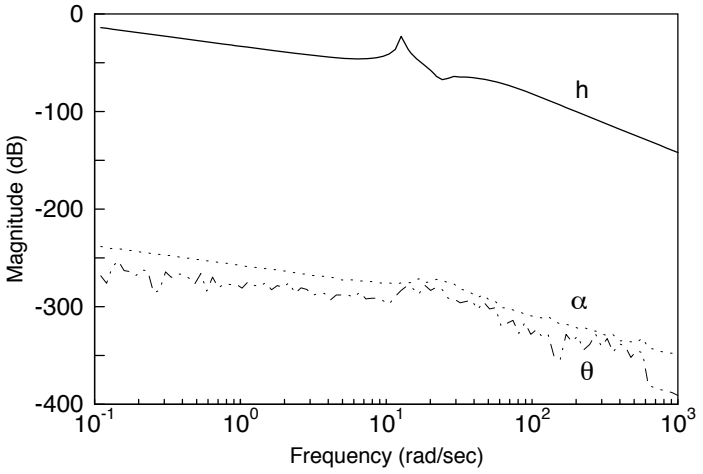

Figure 3.7: Transfer matrix between noise to outputs

enters at low frequency of around 6 rad/sec. To compare the performance of the open- and the closed-loop systems to a sinusoidal disturbance input, the controller is designed at $0.9U_f$ using the same control parameters used earlier. A plot of the frequency response of the transfer matrix from the disturbance input to the output is shown in Fig. 3.8. Clearly, at all frequencies, the frequency response of the two systems exactly overlap, indicating that no attenuation can be expected in the maximum magnitude of the disturbance. This is shown in the time responses of the open- and the closed-loop systems when they are subjected to a sinusoidal input of frequency 6 rad/sec (Fig. 3.9). It is found that the presence of controller did not effect the peak amplitude of the system. The only difference is the faster transient response and shorter settling time.

The singular value Bode plot of the output sensitivity transfer matrix $\boldsymbol{S_o}(s) = \boldsymbol{I}/(\boldsymbol{I}+\boldsymbol{G}(s)\boldsymbol{K}(s))$, which gives a measure of nominal performance (even when the loop is broken at the input) in terms of sensitivenss to parameter variations, is plotted in Fig. 3.10. This figure illustrates that the output h of the compensated system is capable of withstanding parameter variations of low frequency range (< 6 rad/sec) rejecting them by as much as 0.2 dB at very low freqeuncies. The pitch angle outputs of the wing and the store, however show

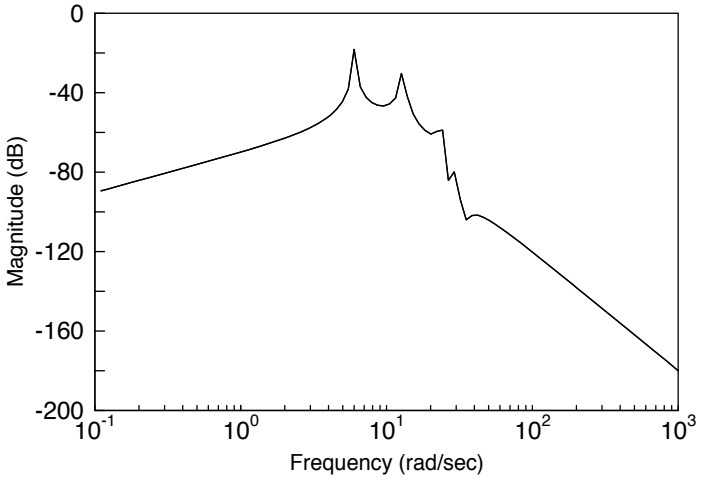

Figure 3.8: Magnitude response of the transfer function from disturbance input to output θ (open/closed-loop system)

no signs of attenuation. The plot also shows that the effects of output disturbances on the plunging motion h get rejected for a good range of frequencies. On the other hand, outputs α and θ allows the disturbances to just pass through (neither attenuate nor amplify) in almost entire range of frequencies, excepting at 1.5 rad/sec where the disturbances amplify output θ's response.

3.3.3 Perturbation Analysis

To evaluate the effectiveness of the closed-loop system to low frequency perturbations, the following two cases were tested.

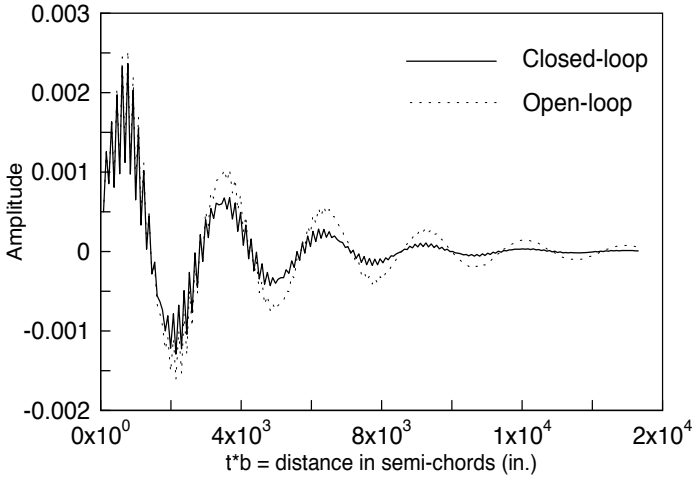

Figure 3.9: Time response of output θ for a sinusoidal disturbance input

Input Matrix Uncertainty

Consider the input matrix $\boldsymbol{H}$ (Section 2.5) to be perturbed to represent a perfect actuator as

$$\tilde{\boldsymbol{H}} = \begin{bmatrix} 0.2 \\ 0.5 \\ 1.4 \end{bmatrix} \tag{3.16}$$

The loop gains of the original and the perturbed systems can be used to calculate the equivalent input multiplicative uncertainty (i.e. reflecting the perturbation to the plant's input)

$$\Delta(j\omega) = \frac{(\boldsymbol{K}\boldsymbol{G}_{pert})(j\omega) - (\boldsymbol{K}\boldsymbol{G}_{nom})(j\omega)}{(\boldsymbol{K}\boldsymbol{G}_{nom})(j\omega)} \tag{3.17}$$

where $\boldsymbol{K}$ is the controller designed based on the unperturbed nominal plant model $\boldsymbol{G}$. The stability at each frequency is assured if $|\Delta(j\omega)|$ is less than the right hand side of Eq. (3.13). The loop gains for the original and perturbed systems as a function of frequency are shown in Fig. 3.11. It is observed that the loop gains differ from one another only at very low frequencies where effects due to parameter variations are prominent. The frequency response of the

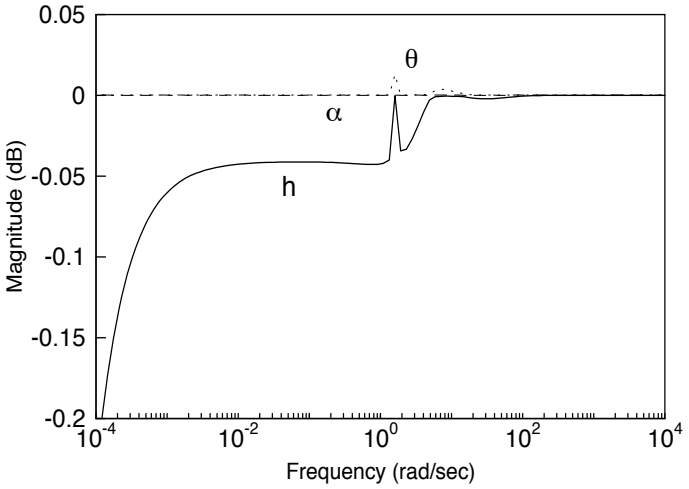

Figure 3.10: Output sensitivity transfer matrix

stability condition (Eq. 3.13) is plotted in Fig. 3.12. It is observed from this figure that at all frequencies and particularly at lower frequencies where the parameter sensitivity is critical, the graph of maximum singular values of $\Delta(j\omega)$ is below that of the minimum singular values of $[\boldsymbol{I} + (\boldsymbol{K}(j\omega)\boldsymbol{G}(j\omega))^{-1}]$. This indicates that the stability is always guaranteed for the given $\tilde{\boldsymbol{H}}$ matrix. Time responses to a pulse input of magnitude 1 on the perturbed open- and closed-loop systems are shown in Fig. 3.13. Up-until $100U_f$ the responses belong to the unperturbed open- and closed-loop systems and the later responses belong to that of the perturbed systems. In both perturbed and unperturbed cases, the output θ of the closed-loop response settles down relatively faster and has smaller amplitude than the corresponding open-loop response.

Circulatory Store Aerodynamic Matrix Uncertainty

To allow the controller to pass through a relatively rigorous parametric test, all the zero terms due to lack of store aerodynamics are made non-zero. In addition, the actuator uncertainty $\tilde{\boldsymbol{H}}$ is also kept for completeness. This amounts to modifying the elements of

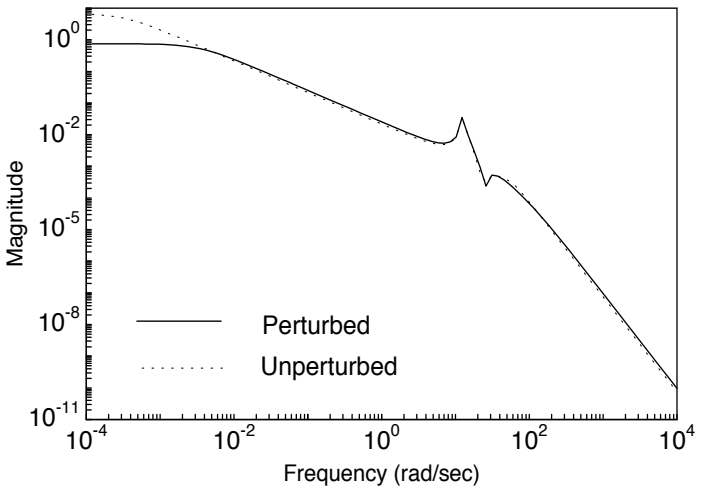

Figure 3.11: Loop gains for the perturbed and unperturbed system

matrices corresponding to the circulatory part of the aerodynamics and are given by

$$\tilde{\boldsymbol{R}} = \begin{bmatrix} -2 \\ 0.69 \\ -2.3 \end{bmatrix} \quad \widetilde{\boldsymbol{S}}_{\boldsymbol{1}} = \begin{bmatrix} 1 & 1 & 1 \end{bmatrix} \quad \widetilde{\boldsymbol{S}}_{\boldsymbol{2}} = \begin{bmatrix} 1 & 0.652 & 1.8 \end{bmatrix} \quad \tilde{\boldsymbol{C}}_{\boldsymbol{nc}} = \begin{bmatrix} 0 & 153 & 0 \\ 0 & 99.756 & 0 \\ 0 & 250 & 0 \end{bmatrix} \tag{3.18}$$

Only some aerodynamic damping due to non-conservative store aerodynamics is assumed to be present ($\boldsymbol{C_{nc}}$ matrix) and it is assumed that the corresponding $\boldsymbol{M_{nc}}$ matrix remains unchanged. The singular value plot of the loop gains for the perturbed and the unperturbed cases are shown in Fig. 3.14. Clearly, the perturbation seems to be large enough to differ significantly from the unperturbed case for the majority of the frequency range of interest. The plot in Fig. 3.15 shows that the stability condition is indeed violated at low frequencies. Hence the closed-loop system for the given perturbation is unstable. A representative plot of the open- and closed-loop simulations to initial conditions is shown in the Fig. 3.16. It is seen that the closed-loop starts to go unstable.

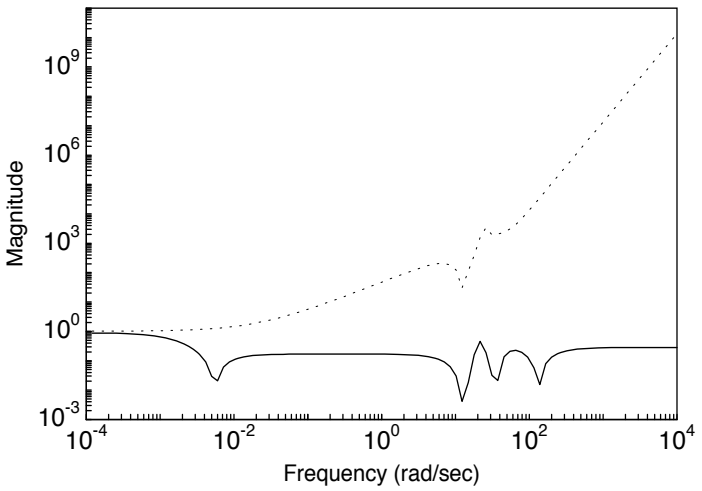

Figure 3.12: Stability test of Eq. (3.13) - solid $\overline{\sigma}[\Delta]$, dashed $\underline{\sigma}[\boldsymbol{I} + (\boldsymbol{KG})^{-1}]$

3.4 Summary

The following are the key features of this chapter. First, the wing/store state-space flutter model is augmented with integrators at the three outputs of interest via the $\boldsymbol{w}$ (Eq. 2.29) that acts as an external disturbance input into the system. The aim is to ensure zero steady-state errors as well as to analyse the system's performance subjected to external disturbance. An optimal feedback control gain is then designed based on the state-to-control weighting ratio. An initial guess was to the weighting matrix was based on the one suggested in Ref. [32]. Using the separation principle, the Kalman-Bucy filter is then designed. Because of the importance of sensitivity properties for the wing/store flutter problem, the LQG design is modified using the Loop Transfer Recovery (LTR) method to recover at least partially the sensitivity margins. The choice of the variable parameter m_f in the LTR method is governed by comparing the design's maximum control-input energy constraint (Eq. 3.14) response (Fig. 3.4) with that obtained with the $\mathcal{H}_\infty$ design (Fig. 4.8). This is to compare the results of the two design methedologies under similar control-energy constraints.

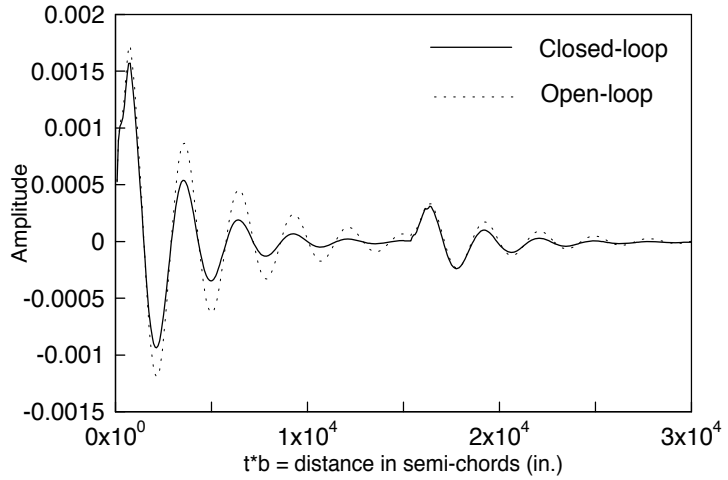

Figure 3.13: Pulse input response of open- and closed-loop systems (output θ)

Robustness analysis test using small gain theorem was performed on the designed closed-loop control system. The results (Fig. 3.2) yielded a minimum tolerance bound of $\pm$ 235% at all frequencies to withstand modeling uncertainties. At and beyond flutter frequency (25 rad/s) the margin of tolerance was even greater ($\geq \pm$ 350%) where it is absolutely necessary to endure errors due to neglecting higher frequency dynamics such as those due to store aerodynamics and other flexible modes. A step response plot (Fig. 3.3) of the open- and closed-loop plant perturbed multiplicatively at the input clearly shows the design's effectiveness in stabilizing the compensated system when the uncompensated system diverges for the given perturbation.

For nominal performance analysis, the controller was designed for the plant at a sub-critical flutter speed. For a step input, the closed-loop system demonstrated a relatively faster transient response and smaller settling time than the open-loop system. Also when the system is excited by a sinusoidal signal of frequency 6 rad/s (a typical disturbance frequency entering at the input of the plant through $\boldsymbol{w}$ of Eq. 2.29), the LTR controller did not show any attenuation of the peak value of the response - an issue that is quite important in the design of proper wing/store flutter control system. Another important performance measure

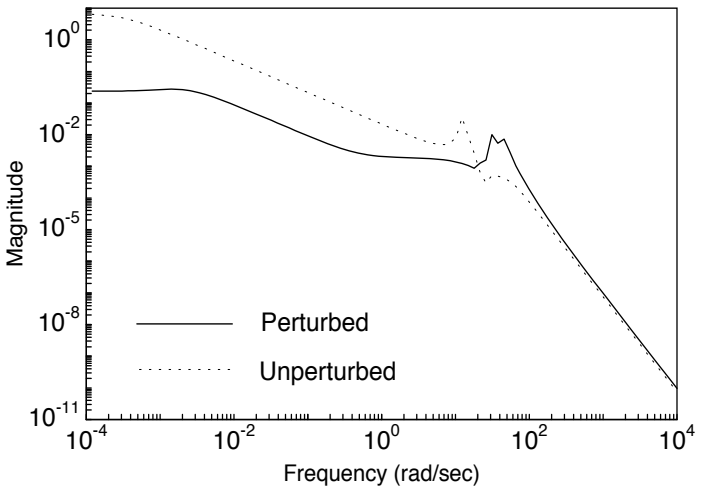

Figure 3.14: Loop gains for the perturbed and unperturbed system

is the output sensitivity function which is an indicator of the systems ability to withstand parameter variations. The plot in Fig. 3.10 shows that the plunging motion output of the closed-loop systems demonstrates rejection of low frequency perturbations while pitch angles outputs do not. They however neither amplify the perturbations.

To study the effect of parameter variations, for instance due to error in modeling actuator vector $\boldsymbol{H}$ and/or matrix corresponding circulatory store aerodynamics, the time response plots plotted indicate that for the former case the system is capable of withstanding the perturbation, but any perturbation of the later category did not yield a stable system. That is, when the store aerodynamic uncertainty is approached from a parametric perturbation point of view then the LQG/LTR compensated system was not successful in maintaining the stability of the system. However when the same uncertainty is categorized as an input multiplicative modeling error, which is usually the realistic case, the tolerance margins shown in Fig. 3.2 indicate good tolerance bounds.

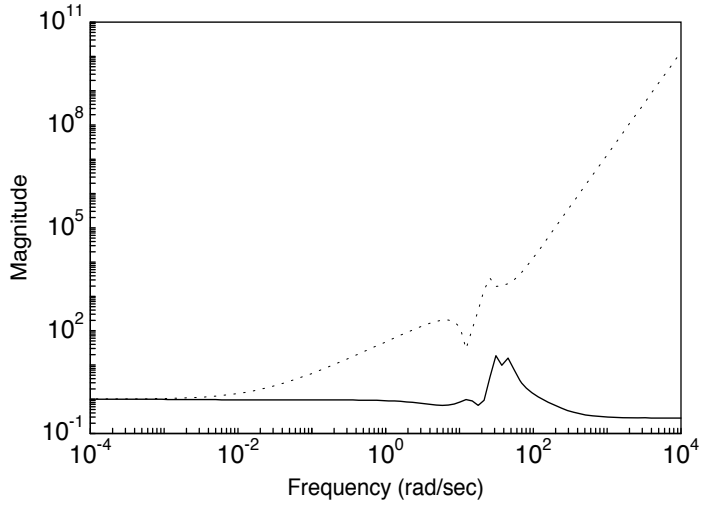

Figure 3.15: Stability test of Eq. (3.13) - solid $\overline{\sigma}[\Delta]$, dashed $\underline{\sigma}[\boldsymbol{I} + (\boldsymbol{KG})^{-1}]$

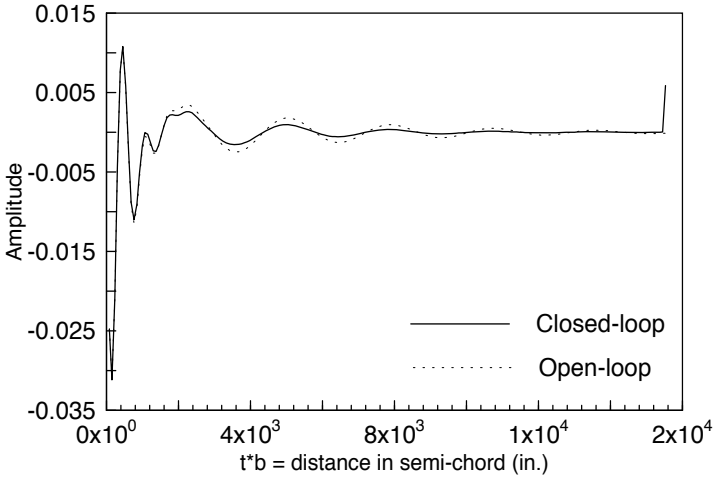

Figure 3.16: Initial condition response of open- and closed-loop systems (output h)

Chapter 4

$\mathcal{H}_\infty$ Controller Design

$\mathcal{H}_\infty$ control problem is a state-space based frequency dependent design and analysis tool. Its formulation is therefore different from other conventional control algorithms which is described in Section 4.1. Section 4.2 presents the basic assumptions required for such a formulation, which is followed by the $\mathcal{H}_\infty$ algorithm in Section 4.3. A mixed-sensitivity $\mathcal{H}_\infty$ control problem is solved for the present wing/store flutter model (Section 4.4). Various simulation results for the choice of weighting functions made are described in Section 4.5 and in subsections following it. Finally the chapter is summarized in Section 4.6.

4.1 $\mathcal{H}_\infty$ Control Problem Formulation

In $\mathcal{H}_\infty$ control literature, there are primarily two ways of designing a controller: the transfer matrix (consisting of transfer functions as elements) shaping approach and the signal-based approach. In the first approach, the shape of the singular values of the transfer matrix is modified by using $\mathcal{H}_\infty$ optimization techniques to match the prespecified requirements on performance and/or stability. In the second approach, $\mathcal{H}_\infty$ optimization theory is used to minimize the energy (or the norm) of error signals of interest under a given set of unwanted

exogenous input signals. If an input multiplicative uncertainty model to the plant is assumed then the signal based approach becomes a problem of addressing robust performance and robust stability issues, which in control literature is the famous μ-synthesis problem involving structured singular value analysis. In this work, μ-synthesis is not considered and is left as a problem of future work. Instead, the shaping of closed-loop transfer functions with stacked objectives involving the output sensitivity function $\boldsymbol{S_o}(s)$ and output complementary sensitivity function $\boldsymbol{T_o}(s)$ is addressed for the improvement of nominal performance and robust stability of wing/store flutter system.

A standard problem formulation into which almost any linear control theory problem can be manipulated is shown in the form of a general configuration called a two-port block diagram [Fig. 4.1]. Here $\boldsymbol{P}$ is the generalized plant and $\boldsymbol{K}$ is the generalized controller to be

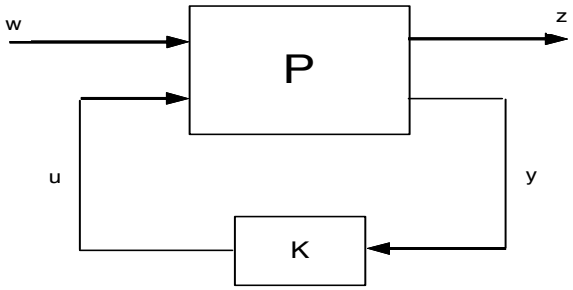

Figure 4.1: Two-port block diagram

designed. The input signal vector $\boldsymbol{w}$ consist of all exogenous inputs (sometimes weighted) comprising of plant disturbances, sensor noises, and model-error outputs, u is the controller output, and $\boldsymbol{y}$ is a vector of signals consisting of measurements, references and other signals that are available for on-line control purposes. Signal $\boldsymbol{z} = (\boldsymbol{z_1}, \boldsymbol{z_2})$ is a vector whose elements are comprised of the weighted cost functions.

The system of Fig. 4.1 is described by

$$\begin{bmatrix} \boldsymbol{z} \\ \boldsymbol{y} \end{bmatrix} = \boldsymbol{P}(s) \begin{bmatrix} \boldsymbol{w} \\ u \end{bmatrix} = \begin{bmatrix} \boldsymbol{P_{11}}(s) & \boldsymbol{P_{12}}(s) \\ \boldsymbol{P_{21}}(s) & \boldsymbol{P_{22}}(s) \end{bmatrix} \begin{bmatrix} \boldsymbol{w} \\ u \end{bmatrix} \tag{4.1}$$

where $\boldsymbol{P}(s)$ is partitioned so that

$$\boldsymbol{z} = \boldsymbol{P_{11}}\boldsymbol{w} + \boldsymbol{P_{12}}u \tag{4.2}$$

$$\boldsymbol{y} = \boldsymbol{P_{21}}\boldsymbol{w} + \boldsymbol{P_{22}}u \tag{4.3}$$

Here $\boldsymbol{P_{11}} \in \mathcal{R}^{p_1 \times m_1}$, $\boldsymbol{P_{12}} \in \mathcal{R}^{p_1 \times m_2}$, $\boldsymbol{P_{21}} \in \mathcal{R}^{p_2 \times m_1}$ and $\boldsymbol{P_{22}} \in \mathcal{R}^{p_2 \times m_2}$. Eliminating u and $\boldsymbol{y}$ using $u = \boldsymbol{K}\boldsymbol{y}$ the closed-loop transfer matrix from $\boldsymbol{w}$ to $\boldsymbol{z}$ can be given by the Linear Fractional Transformation (LFT) [35]

$$\boldsymbol{z} = F_\ell(\boldsymbol{P}, \boldsymbol{K})\boldsymbol{w} \tag{4.4}$$

where

$$F_\ell(\boldsymbol{P}, \boldsymbol{K}) = \boldsymbol{P_{11}} + \boldsymbol{P_{12}}\boldsymbol{K}(\boldsymbol{I} - \boldsymbol{P_{22}}\boldsymbol{K})^{-1}\boldsymbol{P_{21}} \tag{4.5}$$

The minimization of the $\mathcal{H}_\infty$ norm of $F_\ell(\boldsymbol{P}, \boldsymbol{K})$ over all realizable controllers $\boldsymbol{K}(s)$ constitutes the $\mathcal{H}_\infty$ control problem.

The overall control objective then becomes that of minimizing $\mathcal{H}_\infty$ norm of the transfer function from $\boldsymbol{w}$ to $\boldsymbol{z}$. Specifically, the control problem is to find a controller $\boldsymbol{K}$, which based on the sensor data $\boldsymbol{y}$, generates a counteracting control signal u that minimizes the unwanted influence of exogenous signals $\boldsymbol{w}$ on the cost functions of interest $\boldsymbol{z}$. The elements of the generalized plant $\boldsymbol{P}$ are obtained by manipulating the weighted cost functions of the vector $\boldsymbol{z}$ (via the push through rule, for instance) into lower linear fractional transformation form. The state-space representation of the resulting generalized plant is given by

$$\boldsymbol{P} = \left[\begin{array}{c|cc} \boldsymbol{A_p} & \boldsymbol{B_{1p}} & \boldsymbol{B_{2p}} \\ \hline \boldsymbol{C_{1p}} & \boldsymbol{D_{11p}} & \boldsymbol{D_{12p}} \\ \boldsymbol{C_{2p}} & \boldsymbol{D_{12p}} & \boldsymbol{D_{22p}} \end{array}\right] \tag{4.6}$$

which yields the following state-space equations

$$\dot{\boldsymbol{x}} = \boldsymbol{A_p}\boldsymbol{x} + \boldsymbol{B_{1p}}\boldsymbol{w} + \boldsymbol{B_{2p}}u \tag{4.7}$$

$$\boldsymbol{z} = \boldsymbol{C_{1p}}\boldsymbol{x} + \boldsymbol{D_{11p}}\boldsymbol{w} + \boldsymbol{D_{12p}}u \tag{4.8}$$

$$\boldsymbol{y} = \boldsymbol{C_{2p}}\boldsymbol{x} + \boldsymbol{D_{21p}}\boldsymbol{w} + \boldsymbol{D_{22p}}u \tag{4.9}$$

where $\boldsymbol{x}(t) \in \mathcal{R}^n$, $\boldsymbol{w}(t) \in \mathcal{R}^{m_1}$, $\boldsymbol{z}(t) \in \mathcal{R}^{p_1}$, $u(t) \in \mathcal{R}^{m_2}$ and $\boldsymbol{y}(t) \in \mathcal{R}^{p_2}$.

4.2 $\mathcal{H}_\infty$ Control Problem Assumptions

The $\mathcal{H}_\infty$ control algorithm used here is based on the one developed by Glover and Doyle [36]. It is necessary to check for certain assumptions that are essential for applying above algorithm which are listed below:

1. It is assumed that $(\boldsymbol{A_p}, \boldsymbol{B_{2p}})$ is stabilizable and $(\boldsymbol{C_{2p}}, \boldsymbol{A_p})$ is detectable which are necessary conditions for the existence of stabilizing controllers. It guarantees that the controller can reach all unstable states and that these states show up on the measurements.

2. To ensure realizability of the controller it is assumed that the rank conditions,

$$\text{rank}(\boldsymbol{D_{12p}}) = m_2 \qquad \text{rank}(\boldsymbol{D_{21p}}) = p_2$$

are satisfied. Another frequent way of expressing these conditions are

$$\boldsymbol{D_{12p}} = \begin{bmatrix} \boldsymbol{0} \\ \boldsymbol{I} \end{bmatrix} \qquad \boldsymbol{D_{21p}} = \begin{bmatrix} \boldsymbol{0} & \boldsymbol{I} \end{bmatrix}$$

or

$$\boldsymbol{D_{12p}^T D_{12p}} = \boldsymbol{I} \qquad \boldsymbol{D_{21p} D_{21p}^T} = \boldsymbol{I}$$

These equations denote that $\boldsymbol{D_{12p}}$ must have no more columns than rows i.e., the number of error signals in $\boldsymbol{z}$ must be greater than or equal to the number of actuators in u. Also $\boldsymbol{D_{21p}}$ must not have any more rows than columns i.e., the number of external inputs in $\boldsymbol{w}$ must be greater than or equal to the number of sensors in $\boldsymbol{y}$.

The interpretations offered by these conditions are that the error signal $\boldsymbol{z}$ and the output $\boldsymbol{y}$ include non-singular normalized penalties on the control u and sensor noise $\boldsymbol{w}$ (not on the plant disturbance since $\boldsymbol{D_{21p}} = [\boldsymbol{0}\ \boldsymbol{I}]$).

3. In addition, the rank conditions

$$\begin{aligned} \text{Rank}\begin{bmatrix} \boldsymbol{A_p} - j\omega \boldsymbol{I} & \boldsymbol{B_{2p}} \\ \boldsymbol{C_{1p}} & \boldsymbol{D_{12p}} \end{bmatrix} &= n + m_2 \quad \forall\ \omega \\ \text{Rank}\begin{bmatrix} \boldsymbol{A_p} - j\omega \boldsymbol{I} & \boldsymbol{B_{1p}} \\ \boldsymbol{C_{2p}} & \boldsymbol{D_{21p}} \end{bmatrix} &= n + p_2 \quad \forall\ \omega \end{aligned} \tag{4.10}$$

together with stabilizability and detectability conditions guarantees that the two Hamiltonian matrices have no eigenvalues on the imaginary axis.

4. Sometimes for simplicity it is assumed that $\boldsymbol{D_{11p} = 0}$ and $\boldsymbol{D_{22p} = 0}$ to make $\boldsymbol{P_{11}}$ and $\boldsymbol{P_{22}}$ strictly proper.

In the event that any of the rank conditions are violated, matrices such as $\boldsymbol{A_p}$ and/or $\boldsymbol{D_p}$ can be modified [36] to satisfy the requirements in such a manner that the behavior of the plant is changed very little over significant range of frequencies. For a more general situation where some of these assumptions are relaxed, see Ref. [29].

4.3 $\mathcal{H}_\infty$ Control Algorithm

For the general control configuration of Fig. 4.1 described by Eqs. (4.7-4.9), with assumptions listed above, the algorithm proposed by Glover, et al. [36] states that a stabilizing controller $\boldsymbol{K}(s)$ satisfying $\|F_\ell(\boldsymbol{P}, \boldsymbol{K})\|_\infty < \gamma$ exists if and only if the following conditions are satisfied:

1.

$$X_\infty = X_\infty^T = \text{Ric}\begin{bmatrix} \boldsymbol{A_p} & \gamma^{-2}\boldsymbol{B_{1p}}\boldsymbol{B_{1p}^T} - \boldsymbol{B_{2p}}\boldsymbol{B_{2p}^T} \\ -\boldsymbol{C_{1p}^T}\boldsymbol{C_{1p}} & -\boldsymbol{A_p^T} \end{bmatrix} \geq 0 \tag{4.11}$$

2.

$$Y_\infty = Y_\infty^T = \mathrm{Ric}\begin{bmatrix} \boldsymbol{A_p^T} & \gamma^{-2}\boldsymbol{C_{1p}^T C_{1p}} - \boldsymbol{C_{2p}^T C_{2p}} \\ -\boldsymbol{B_{1p}B_{1p}^T} & -\boldsymbol{A_p} \end{bmatrix} \geq 0 \tag{4.12}$$

3. the above Hamiltonians have no imaginary eigenvalues

4. $\rho(X_\infty Y_\infty) < \gamma^2$

The procedure for implementing the algorithm is as follows: First a large value of γ is selected and the above conditions are tested. If any of them fail, then γ is considered too small for any solution to exist, and γ is increased for the next iteration and the conditions are again checked. The process is terminated when γ is large enough to pass all the tests. The family of all stabilizing controllers $\boldsymbol{K}(s)$ satisfying $\|F_\ell(\boldsymbol{P},\boldsymbol{K})\|_\infty < \gamma$ is then given by $\boldsymbol{K} = F_\ell(\boldsymbol{K_c},\boldsymbol{Q})$ where $\boldsymbol{Q}(s)$ is any stable proper transfer function such that $\|\boldsymbol{Q}\|_\infty < \gamma$ and

$$\boldsymbol{K_c}(s) = \left[\begin{array}{c|cc} \boldsymbol{A_\infty} & -\boldsymbol{Z_\infty L_\infty} & \boldsymbol{Z_\infty B_{2p}} \\ \hline \boldsymbol{F_\infty} & \boldsymbol{0} & \boldsymbol{I} \\ -\boldsymbol{C_{2p}} & \boldsymbol{I} & \boldsymbol{0} \end{array}\right] \tag{4.13}$$

where

$$\begin{aligned} \boldsymbol{A_\infty} &= \boldsymbol{A_p} + \gamma^{-2}\boldsymbol{B_{1p}B_{1p}^T X_\infty} + \boldsymbol{B_{2p}F_\infty} + \boldsymbol{Z_\infty L_\infty C_{2p}} \\ \boldsymbol{Z_\infty} &= (\boldsymbol{I} - \gamma^{-2}\boldsymbol{Y_\infty X_\infty})^{-1} \\ \boldsymbol{F_\infty} &= -\boldsymbol{B_{2p}^T X_\infty} \\ \boldsymbol{L_\infty} &= -\boldsymbol{Y_\infty C_{2p}^T} \end{aligned}$$

A particular member of the family of solutions obtained by letting $\boldsymbol{Q}(s) = \boldsymbol{0}$ has the structure of a state estimator. The controller obtained when $\boldsymbol{Q}(s) = \boldsymbol{0}$ is called a "central" or "maximum-entropy" [36] controller and is given by

$$\boldsymbol{K}(s) = -\boldsymbol{Z_\infty L_\infty}(s\boldsymbol{I} - \boldsymbol{A_\infty})^{-1}\boldsymbol{F_\infty} \tag{4.14}$$

which has the same number of states as the generalized plant $\boldsymbol{P}(s)$ and can be separated into an observer of the form

$$\dot{\hat{\boldsymbol{x}}} = \boldsymbol{A_p}\hat{\boldsymbol{x}} + \boldsymbol{B_{1p}}\underbrace{\gamma^{-2}\boldsymbol{B_{1p}^T}\boldsymbol{X_\infty}\hat{\boldsymbol{x}}}_{\hat{\boldsymbol{w}}_{worst}} + \boldsymbol{B_{2p}}u + \boldsymbol{Z_\infty}\boldsymbol{L_\infty}(\boldsymbol{C_{2p}}\hat{\boldsymbol{x}} - \boldsymbol{y}) \tag{4.15}$$

and a state feedback

$$u = \boldsymbol{F_\infty}\hat{\boldsymbol{x}} \tag{4.16}$$

On comparison, the estimator equation is similar to Kalman filter equation where $\boldsymbol{L_\infty}$ is the output injection matrix scaled by $\boldsymbol{Z_\infty}$ and $\boldsymbol{F_\infty}$ is the state feedback gain matrix. The only additional term appearing in the above equation is $\boldsymbol{B_{1p}}\hat{\boldsymbol{w}}_{worst}$ where $\hat{\boldsymbol{w}}_{worst}$ is the estimate of the worst-case disturbance. Another important feature of $\mathcal{H}_\infty$ control design is the presence of terms $\gamma^{-2}\boldsymbol{B_{1p}}\boldsymbol{B_{1p}^T}$ and $\gamma^{-2}\boldsymbol{C_{1p}}\boldsymbol{C_{1p}^T}$ in the two Algebraic Riccatti Equations (ARE) obtained from the Hamiltonians in Eqs. (4.11) and (4.12). On comparison to ARE calculated for LQR state feedback matrix, the additional term $\gamma^{-2}\boldsymbol{B_{1p}}\boldsymbol{B_{1p}^T}$ indicates the influence of the way in which external disturbances enter the system (through $\boldsymbol{B_{1p}}$) and the possibility of the designer to weigh individual elements by properly selecting the matrix $\boldsymbol{B_{1p}}$. Similarly, on comparison with the ARE for Kalman-Bucy filter, $\mathcal{H}_\infty$ design is again influenced by the weights used in the linear combination of the output states. The freedom to choose the matrices $\boldsymbol{B_{1p}}$ and $\boldsymbol{C_{1p}}$ adds to the already large family of stabilizing controllers and hence the designer can expect to obtain higher performance and robustness levels in $\mathcal{H}_\infty$ control design than by traditional LQG design.

4.4 Wing/Store $\mathcal{H}_\infty$ Control Problem

As mentioned earlier, in $\mathcal{H}_\infty$ control design it is common to first identify the objective functions whose infinity norm is to be minimized. Typically they are either single- or multi-target objectives involving output sensitivity function $\boldsymbol{S_o}(s)$, output complementary

sensitivity function $\boldsymbol{T_o}(s)$ and/or control-input constraint function $\boldsymbol{U}(s)$. $\boldsymbol{S_o}(s)$ is the transfer function between the external disturbance (entering at the plant output) and the output and is a good measure for disturbance rejection. $\boldsymbol{T_o}(s)$ on the other hand is a good measure of noise attenuation and robust stability and is defined as the closed-loop transfer function between the input and the output of the plant.

Because $\boldsymbol{S_o}(s) + \boldsymbol{T_o}(s) = \boldsymbol{I}$, achieving good performance and robustness to model uncertainty cannot be attained simultaneously with ease. Fortunately, these objectives can be minimized in their respective frequency range of occurance by assigning frequency dependent weighting functions. For instance, since disturbances typically enter at low frequency region, a low-pass filter can be used for the sensitivity function to weed-out the high frequency content and assign importance to rejecting disturbances in that region. Similarly, $\boldsymbol{T_o}(s)$ can be weighed using a high-pass filter to assert the importance of minimizing its maximum singular values at high frequencies where the effect of model uncertainties and noise on the output are more prominent. Again as before (Chapter 3), for disturbance rejection and minimum sensitivity to structured perturbations, the maximum singular values of $\boldsymbol{S_o}(s)$ must be small and for good noise attenuation and robust stability with respect to output multiplicative uncertainty (in case of $\mathcal{H}_\infty$ design), the maximum singular values of $\boldsymbol{T_o}(s)$ must be made small.

This research work attempts to investigate the feasibility of designing a $\mathcal{H}_\infty$ controller-based closed-loop system that is robust to uncertainties due to store aerodynamics and other high frequency flexible structural modes that have been ignored. The designed closed-loop system is also intended to have good performance characteristics such as disturbance rejection and insensitiveness to low frequency parameter variations. Changes in the center of gravity location of store, mass, radius of gyration, etc are some of the examples of parameter variations that may occur in wing/store flutter suppression problem during typical combat maneuvers.

Mathematically these objectives are equivalent to minimizing the weighted output

sensitivity $\boldsymbol{S_o}(s)$ and output complementary sensitivity $\boldsymbol{T_o}(s)$ transfer matrices. Within the framework of $\mathcal{H}_\infty$ control theory, this implies the minimization of the infinity norm [36]

$$\min \left\| \begin{bmatrix} \boldsymbol{W_1 S_o} \\ \boldsymbol{W_2 T_o} \end{bmatrix} \right\|_\infty = \min \left\| \begin{bmatrix} \boldsymbol{W_1 (I + GK)^{-1}} \\ \boldsymbol{W_2 GK (I + GK)^{-1}} \end{bmatrix} \right\|_\infty < 1 \tag{4.17}$$

Here the loop is considered to be broken at the output where all the uncertainties are assumed to be reflected. Based on given performance requirements, frequency dependent weighting functions $\boldsymbol{W_1}(s)$ and $\boldsymbol{W_2}(s)$ can be appropriately chosen to give the designer relatively more freedom to achieve the desired objectives. Since it is unnecessary to minimize the effect of a cost function over a frequency range in which its effect is least likely, low and high-pass filters are generally used as weighting functions. Here the objective is to find an admissible controller $\boldsymbol{K}(s)$ which minimizes the above weighted norm subject to the constraint that the closed-loop system be stable.

A general block diagram of the objective function is shown in Fig. 4.2 where signals

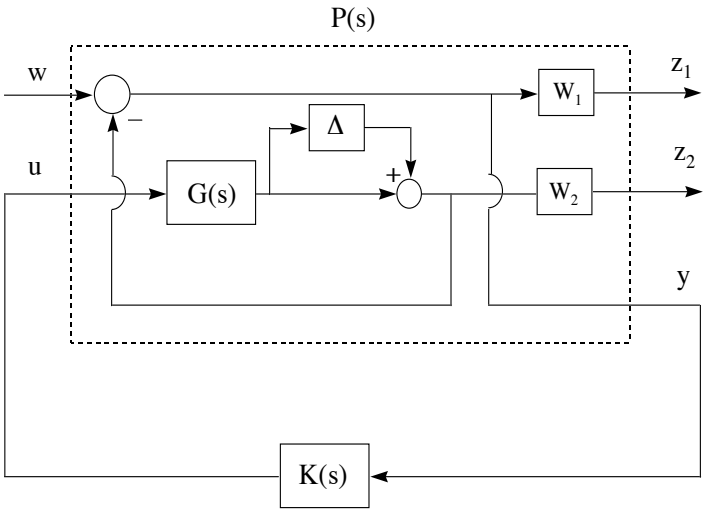

Figure 4.2: Block diagram of weighted mixed-sensitivity objective function

$\boldsymbol{w}$, u, $\boldsymbol{y}$ and $\boldsymbol{z}$ all carry the same information as given in the earlier section. Using Linear Fractional Transformation (LFT) theory [35], these weighted cost functions are reformulated

as

$$\begin{bmatrix} \boldsymbol{z_1} \\ \boldsymbol{z_2} \\ \boldsymbol{y} \end{bmatrix} = \begin{bmatrix} \boldsymbol{P_{11}} & \boldsymbol{P_{12}} \\ \boldsymbol{P_{21}} & \boldsymbol{P_{22}} \end{bmatrix} \begin{bmatrix} \boldsymbol{w} \\ u \end{bmatrix} = \left[\begin{array}{c|c} \boldsymbol{W_1} & \boldsymbol{-W_1 G} \\ \boldsymbol{0} & \boldsymbol{W_2 G} \\ \hline \boldsymbol{I} & \boldsymbol{-G} \end{array}\right] \begin{bmatrix} \boldsymbol{w} \\ u \end{bmatrix} \tag{4.18}$$

where $\boldsymbol{P}(s)$ is the generalized plant with realization $(\boldsymbol{A_p}, \boldsymbol{B_p}, \boldsymbol{C_p}, \boldsymbol{D_p})$ and $\boldsymbol{K}(s)$ represents the $\mathcal{H}_\infty$ controller. Since, for this problem, p_1 $(= 6) > m_2$ $(= 1)$ and p_2 $(= 3) \geq m_1$ $(= 3)$, the situation is referred to as a two-block $\mathcal{H}_\infty$ optimization problem [34]. The generalized plant is described by a set of equations

$$\begin{aligned} \dot{\boldsymbol{x}} &= \boldsymbol{A_p x} + \boldsymbol{B_{1p} w} + \boldsymbol{B_{2p}} u \\ \boldsymbol{z} &= \boldsymbol{C_{1p} x} + \boldsymbol{D_{11p} w} + \boldsymbol{D_{12p}} u \\ \boldsymbol{y} &= \boldsymbol{C_{2p} x} + \boldsymbol{D_{21p} w} + \boldsymbol{D_{22p}} u \end{aligned} \tag{4.19}$$

where the system matrices are given by [29]

$$\boldsymbol{P}(s) = \left[\begin{array}{c|c} \boldsymbol{A_p} & \boldsymbol{B_p} \\ \hline \boldsymbol{C_p} & \boldsymbol{D_p} \end{array}\right] = \left[\begin{array}{ccc|cc} \boldsymbol{A} & \boldsymbol{0} & \boldsymbol{0} & \boldsymbol{0} & \boldsymbol{B} \\ \boldsymbol{B_1 C} & \boldsymbol{A_1} & \boldsymbol{0} & \boldsymbol{B_1} & \boldsymbol{-B_1 D} \\ \boldsymbol{B_2 C} & \boldsymbol{0} & \boldsymbol{A_2} & \boldsymbol{0} & \boldsymbol{B_2 D} \\ \hline \boldsymbol{-D_1 C} & \boldsymbol{C_1} & \boldsymbol{0} & \boldsymbol{D_1} & \boldsymbol{-D_1 D} \\ \boldsymbol{D_2 C} & \boldsymbol{0} & \boldsymbol{C_2} & \boldsymbol{0} & \boldsymbol{D_2 D} \\ \boldsymbol{-C} & \boldsymbol{0} & \boldsymbol{0} & \boldsymbol{I} & \boldsymbol{-D} \end{array}\right] \tag{4.20}$$

and where $\boldsymbol{x}(t) \in \mathcal{R}^n$, $\boldsymbol{w}(t) \in \mathcal{R}^{m_1}$, $\boldsymbol{z}(t) \in \mathcal{R}^{p_1}$, $u(t) \in \mathcal{R}^{m_2}$ and $\boldsymbol{y}(t) \in \mathcal{R}^{p_2}$.

4.5 Simulation Results

The aim is to design an $\mathcal{H}_\infty$ controller that not only stabilizes the system at flutter speed but also maintains stability and improve nominal performance in the presence of unstructured uncertainties discussed earlier. To design an $\mathcal{H}_\infty$ controller, appropriate

weighting functions have to be first selected in order to be included in the generalized plant matrices (Eq. 4.20). The choice of weights is not trivial and is generally chosen purely as tuning functions to achieve best compromise between conflicting objectives. However its selection is often guided by the need to reject unwanted signals such as errors, noises, etc. in certain range of frequencies. Specifically the aim is to achieve at least 10:1 reduction in the output errors (with respect to open-loop performance) in the presence of low frequency (< 30 rad/sec) disturbances. This value of frequency is chosen so as to reject any unnecessary signals that are in the close range of critical flutter frequency ($\sim$25 rad/sec). This frequency range also includes some typical disturbance frequencies such as those due to gusts ($\sim$6 rad/sec), whose rejection is an important objective in the design process of a robust controller. For frequencies beyond 30 rad/sec, a 40-dB/decade roll-off is desired which places the control loop bandwidth at approximately 60 rad/sec. Such a steep roll-off ensures that the controller is proper. A closed-loop bandwidth of 60 rad/sec together with a second order roll-off also ensures acceptable noise attenuation and sufficient stability margin to tolerate variations in the loop transfer matrix magnitude which might arise due to unmodeled dynamics.

Based on above design specifications which quantify the trade-off between nominal performance and robust stability, the following weighting matrices are constructed:

$$\boldsymbol{W_1}(s) = \gamma \frac{10(s/3674.2+1)^2}{(s/30+1)^2}\boldsymbol{I_3} \tag{4.21}$$

$$\boldsymbol{W_2}(s) = \frac{(s+30)^2}{s+4500}\boldsymbol{I_3} \tag{4.22}$$

where $\boldsymbol{I_3}$ indicates that equal weighting has been assigned to each of the outputs. A singular value Bode plot of $\boldsymbol{W_1^{-1}}(s)$ and $\boldsymbol{W_2^{-1}}(s)$ depicting the design specifications for $\gamma = 1$ is shown in Fig. 4.3. The variable γ in $\boldsymbol{W_1}$ acts as a design parameter that is iteratively decreased until the norm in Eq. (4.17) is no longer satisfied. Physically it gives relative importance to one of the two conflicting objectives without sacrificing compromise between them. The *hinfopt* routine in PRO-MATLAB's Robust Control Toolbox [37] is used to find

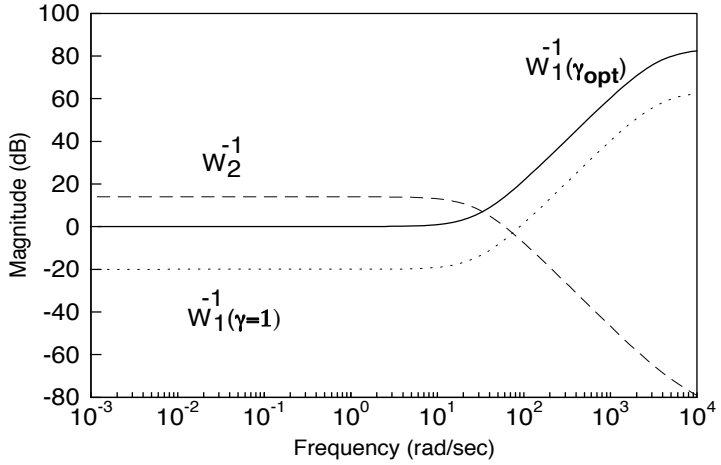

Figure 4.3: Bode plot of $\boldsymbol{W_1^{-1}}(s)$ and $\boldsymbol{W_2^{-1}}(s)$

an optimum value of γ for the plant and given set of weighting functions, which after several iterations is found to be 0.0996. Therefore the mathematically optimum performance (and hence robustness) specification corresponding to $\gamma_{opt} = 0.0996$ has set the upper limit for achievable design. The resulting deviation of the singular value Bode plot of $\boldsymbol{W_1^{-1}}(s)$ for $\gamma_{opt} = 0.0996$ from its initial plot corresponding to $\gamma = 1$ is shown in Fig. 4.3.

A plot of the cost function (Eq. 4.17) as a function of frequency for each of the outputs is shown in Fig. 4.4. In this figure, the cost functions for the pitching motions (α and θ) show slight deviation from one another at low frequencies having a magnitude in the neighborhood of 0 dB in the positive side. They roll-off at the rate of approximately 40-dB/decade in mid-frequency range. The singular value plot of the cost function corresponding to output h however has a magnitude of < 1 at all frequencies, with the roll-off rate at high frequencies being approximately equal to 20-dB/decade. This indicates that among the three outputs, the plunging motion (h) is least effected by parameter changes and output disturbances. The wing pitch angle (θ) and the store pitch angle relative to wing (θ), on the other hand, demonstrate relative sensitiveness to above inputs. Satisfactory noise attenuation properties are however exhibited by all the three outputs.

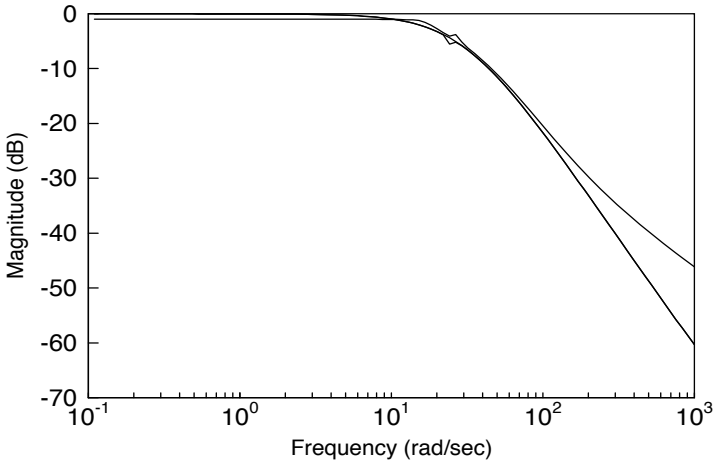

Figure 4.4: Singular value plot of the cost function

The gradual roll-off starting at mid frequency of the three outputs to higher frequencies indicate that the design performance of requiring the magnitude to be less than 1 is over-achieved ($\ll 1$). The cost function response corresponding to output h diverging from the other two at higher frequencies indicate that it would have a relatively smaller magnitude for noise attenuation.

4.5.1 Robust Stability Analysis

A singular value sufficiency test for stability robustness of a closed-loop system subjected to uncertainty due to unmodeled dynamics is obtained by applying the small gain theorem [33] to the loop in the block diagram of Fig. 4.5. For the $\mathcal{H}_\infty$ problem formulation, all the uncertainties discussed earlier are required to be reflected at the plant output [36]. Application of small gain theorem to the loop (Fig. 4.5) yields

$$\overline{\boldsymbol{\sigma}}[\boldsymbol{\Delta}]\overline{\boldsymbol{\sigma}}[\boldsymbol{T}_o] < 1 \tag{4.23}$$

where

$$\boldsymbol{T_o}(s) = \begin{matrix} \boldsymbol{G}(s)\boldsymbol{K}(s) \\ \boldsymbol{I} + \boldsymbol{G}(s)\boldsymbol{K}(s) \end{matrix}$$

is output complementary sensitivity transfer matrix. Assuming $\boldsymbol{GK}$ to be nonsingular, the above inequality can be further simplified to

$$\boldsymbol{\sigma}[\boldsymbol{\Delta}(j\omega)] < \underline{\boldsymbol{\sigma}}[\boldsymbol{I} + (\boldsymbol{G}(j\omega)\boldsymbol{K}(j\omega))^{\boldsymbol{-1}}] \qquad \forall\omega \tag{4.24}$$

This gives a conservative percentage tolerance bounds for output multiplicative perturbations that the closed-loop system can withstand before being destabilized.

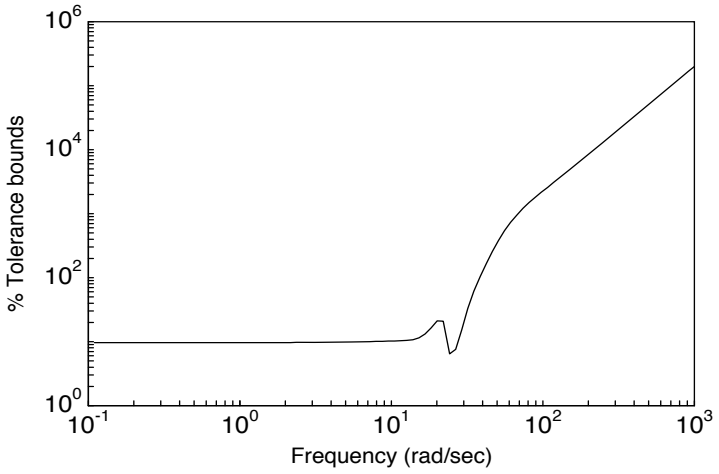

Figure 4.5: Singular value Bode plot of uncertainty tolerance bounds

Figure 4.5 shows the singular value Bode plot of the output multiplicative uncertainty tolerance bounds $\boldsymbol{\Delta}(s)$ as a function of frequency ω. The absolute value of the minimum singular value of $[\boldsymbol{I} + (\boldsymbol{G}(j\omega)\boldsymbol{K}(j\omega))^{\boldsymbol{-1}}]$ is found to be 15.52 dB, which implies that the closed-loop system is capable of withstanding at least $\pm 298\%$ plant uncertainty (with errors reflected at the output), without being destabilized. This magnitude of stability margin is observed to be at the flutter frequency (25 rad/sec) where it is required to alleviate the effects of unmodeled dynamics, such as those due to wing/store aerodynamic and other

flutter critical uncertainties. For frequencies beyond the 25 rad/sec, the percentage tolerance bounds increase monotonically with the increase in frequency. Large endurance margins are necessary at such frequencies where the effects of ignoring the aileron degree-of-freedom and other flexible modes including sensor and actuator dynamics are more prominent.

To test the effectiveness of the controller in sustaining any errors due to unmodeled dynamics, the multiplicative uncertainty model developed in Section 2.7 of Chapter 2 will be used. For small gain theorem to be used for uncertainty analysis, the error model $\Delta_m(s)$ must be stable and hence it is designed at sub-critical flutter speed of $0.9U_f$ with U_f/b being equal to $170sec^{-1}$. Figure 4.5 shows the plot of the output multiplicative uncertainty $\boldsymbol{\Delta}(s)$. For efficient tolerance capability of the closed-loop system, the plot of the maximum singular values of $\boldsymbol{\Delta}(s)$ must be less than the plot of the minimum singular values of $[\boldsymbol{I} + (\boldsymbol{GK})^{-1}]$ Eq. 4.24. Since robustness to modeling errors is a high frequency phenomenon, the plot of $\boldsymbol{\Delta}(s)$ must be below that of the other at least in the high frequency range. For the most part, it is indeed so and hence theoretically the $\mathcal{H}_\infty$ controller designed for this system should be able to withstand the given stable modeling error term, had it been appended to the plant in an output multiplicative sense. Since the plant is being multiplicatively perturbed at its output, the three available signals channels are perturbed individually by Δ_m for dimensional consistency as shown in the Fig. 4.6. The perturbation matrix can be realized as

$$\boldsymbol{\Delta}(s) = \begin{bmatrix} \Delta_m(s) & 0 & 0 \\ 0 & \Delta_m(s) & 0 \\ 0 & 0 & \Delta_m(s) \end{bmatrix} \tag{4.25}$$

Figure 4.7 compares the step response of the perturbed closed-loop system with that of the open-loop perturbed system. The dotted line in this figure clearly is increasing in amplitude, so the open-loop system with passive decoupler pylon is unable to withstand such a perturbation due to unmodeled dynamics arising from neglecting store aerodynamics and therefore diverges. Whereas with the closed-loop system on, the system endures such a perturbation and over a period of time suppresses it effectively.

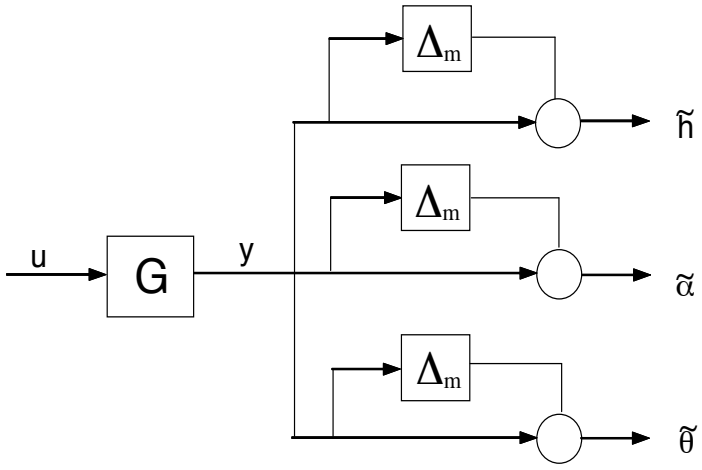

Figure 4.6: Output multiplicative uncertainty configuration

The shift in the steady-state value for the open- and closed-loop responses is due to the difference in dc gain (gain at low frequency $\omega = 0$) of the two systems which need not necessarily be the same. One way to let the systems have zero steady-state errors is to incorporate integral actions at the three output channels of interest. However including integrators for $\mathcal{H}_\infty$ design violates some of the assumptions listed above. Zhou et al. [29] present a procedure for augmenting the plant with integrators that simultaneously satisfy the necessary assumptions. The draw back is that it increases the order of the controller and hence is not included for the present analysis. Moreover since the magnitude of the difference in steady-state values is not too large, integral action has not been included in the design of the controller.

As mentioned earlier in Section 3.3.1, the additive uncertainty model also plays important role in assessing the stability robustness of the closed-loop systems. In addition, they also give a measure of control energy [34] which is given by

$$\overline{\boldsymbol{\sigma}}[\boldsymbol{\Delta}]\overline{\boldsymbol{\sigma}}\left[\frac{\boldsymbol{K}}{\boldsymbol{I}+\boldsymbol{GK}}\right] < 1 \tag{4.26}$$

The $\mathcal{H}_\infty$ norm of $\boldsymbol{K}/(\boldsymbol{I}+\boldsymbol{GK})$ is the square root of the maximal control-input energy. Thus the robust stability constraint for additive perturbations given above also limits the

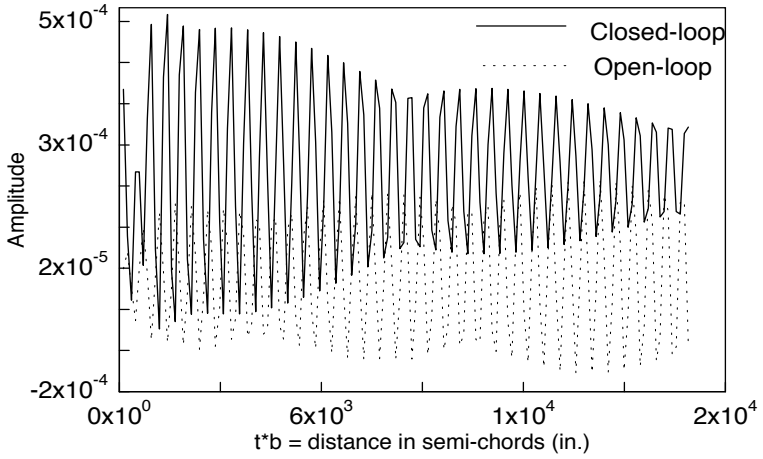

Figure 4.7: Step response of the open- and output multiplicatively perturbed closed-loop systems (output h)

maximal control-input energy.

What is shown in Fig. 4.8 is the tolerance bounds for additive perturbations plotted as a function frequency from the condition

$$\overline{\boldsymbol{\sigma}}[\boldsymbol{\Delta}] < \underline{\boldsymbol{\sigma}}[\boldsymbol{G} + \boldsymbol{K}^{-1}] \tag{4.27}$$

where $\boldsymbol{K}$ is non-singular. The above relation gives the size of the absolute perturbation $\boldsymbol{\Delta}(j\omega)$ that can be tolerated before the closed-loop becomes unstable. For instance, at 1000 rad/sec, the closed-loop system can tolerate a stable additive perturbation of infinity norm of 1.53×10^2.

The singular value Bode plot of the controller is shown Fig. 4.9, which approximately shows the characteristics of a first order system with a break frequency of 20 rad/sec. A 17-state strictly proper controller is obtained by solving the two-block mixed-sensitivity $\mathcal{H}_\infty$ problem. The controller has a large gain and has a bandwidth of 600 rad/sec as shown in Fig. 4.9. Large bandwidths are desired to be able to withstand sudden (additive) perturbations in the outputs of the plant. But in most applications, a controller with limited

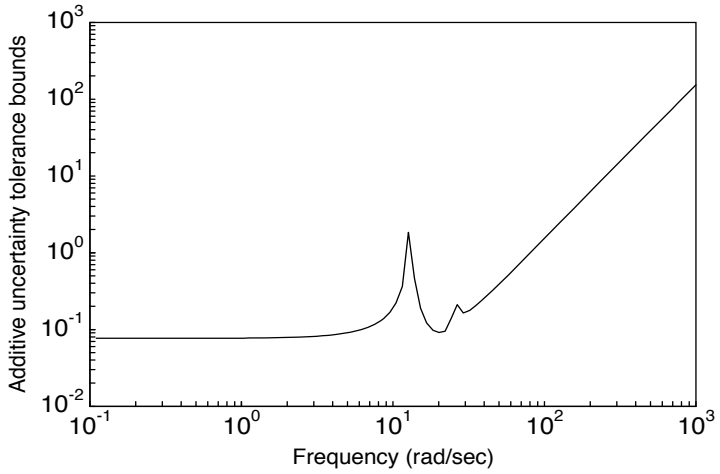

Figure 4.8: Additive uncertainty tolerance bounds

bandwidth is enough to prevent pushing the actuators beyond their limits and to avoid the controller exciting high frequency discarded modes. It also facilitates digital implementation wherein issues of sampling frequencies need to be further taken care of. A well designed controller should therefore take into account the above characteristics for its successful implementation.

4.5.2 Nominal Performance Analysis

For nominal performance analysis, the controller is designed at sub-critical flutter speed ($0.9U_f$) with an intention of comparing the open-loop passive decoupler pylon mounted wing/store system responses with those of the closed-loop to assess the effectiveness of active system. A time response of the output h for open- and closed-loop systems are compared in the figure below. Clearly the closed-loop system's output has better response than the open-loop system's output in terms of smaller amplitude of the transient response and faster settling time.

Figure 4.11 demonstrates that the compensated system has nice noise attenuation

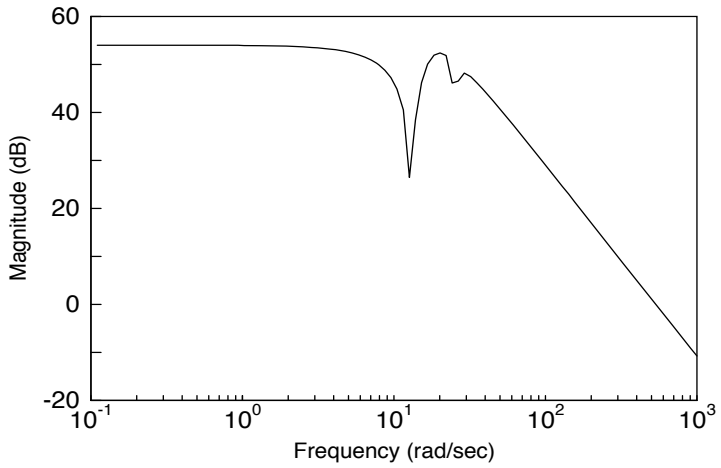

Figure 4.9: Controller transfer function

property at the three outputs h, α and θ, rejecting noise at higher frequencies (> 450 rad/sec) by as much as 80 dB. On comparison with Fig. 4.3 [$\boldsymbol{W_2^{-1}}(s)$], it is clear that while at higher frequencies the desired 40-dB/decade roll-off rate has been achieved, unnecessary noise attenuation is observed (for output h) at lower frequencies where its effect on the closed-loop response is typically negligible.

Another nominal performance measure can be obtained by comparing the open- and closed-loop magnitude response from disturbance input to output as shown in Fig. 4.12. A sinusoidal input centered at 6 rad/sec is used to model the disturbance. The singular value Bode plot in Fig. 4.12 indicates that the closed-loop system has better rejection magnitude than the open-loop wing/store model. At low frequencies of less than 10 rad/sec, where disturbances frequently enter, the closed-loop systems rejects them by at least 30 dB (with respect to the open-loop system) at the output θ. Particularly at the external disturbance frequency of 6 rad/sec, it rejects by as much as 62 dB. This can be verified by looking at the corresponding reduction in peak amplitudes of the time responses of the output θ when the open- and the closed-loop systems are subjected to sinusoidal frequency of 6 rad/sec (Fig. 4.13-4.14).

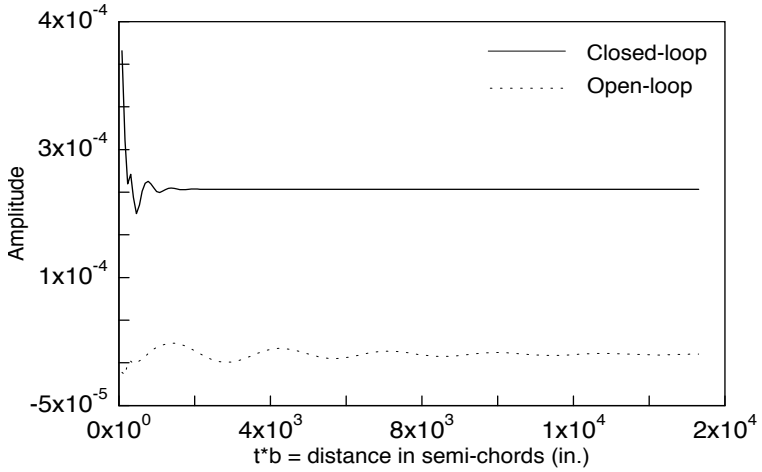

Figure 4.10: Step responses (output h)

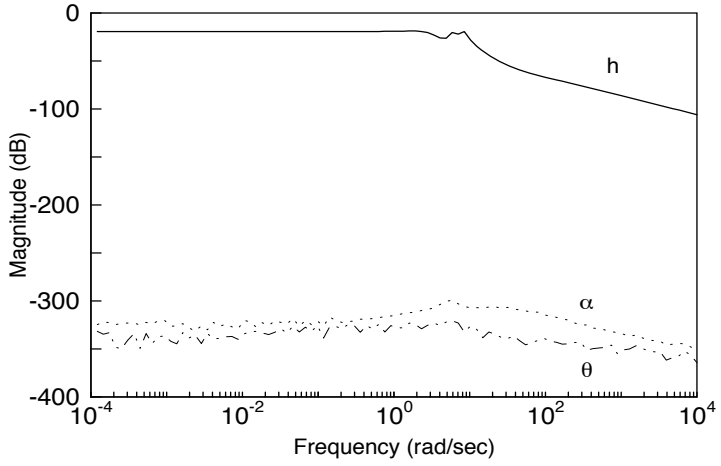

Figure 4.11: Output complementary sensitivity transfer matrix

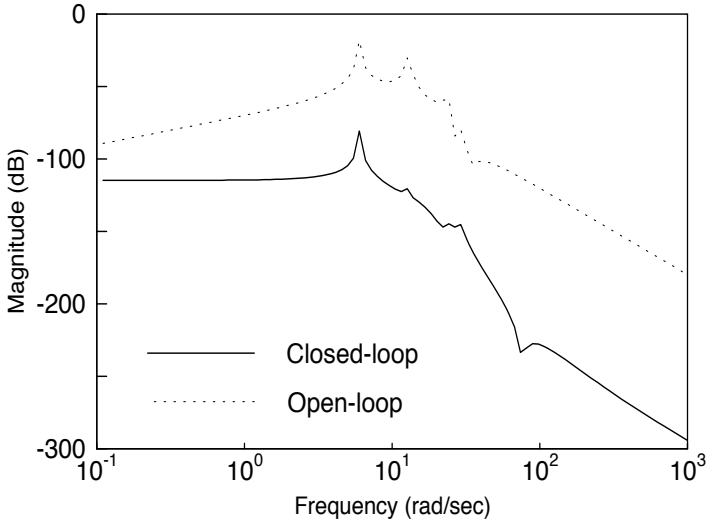

Figure 4.12: Magnitude response of the transfer function from disturbance input to output θ

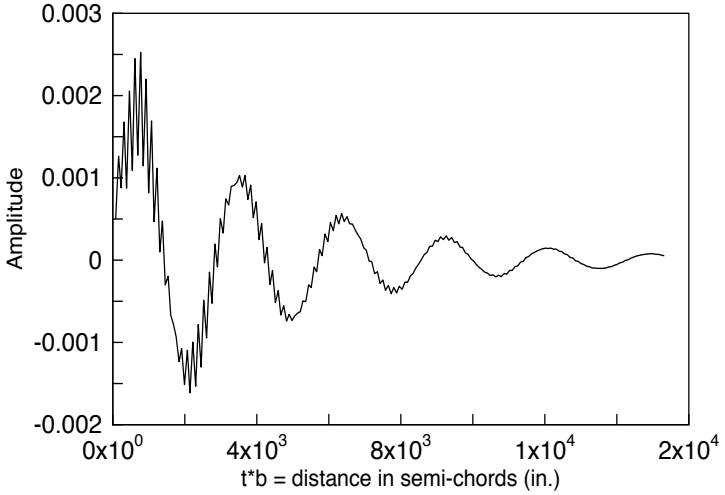

Figure 4.13: Time response of the open-loop system (output θ) to sinusoidal disturbance input

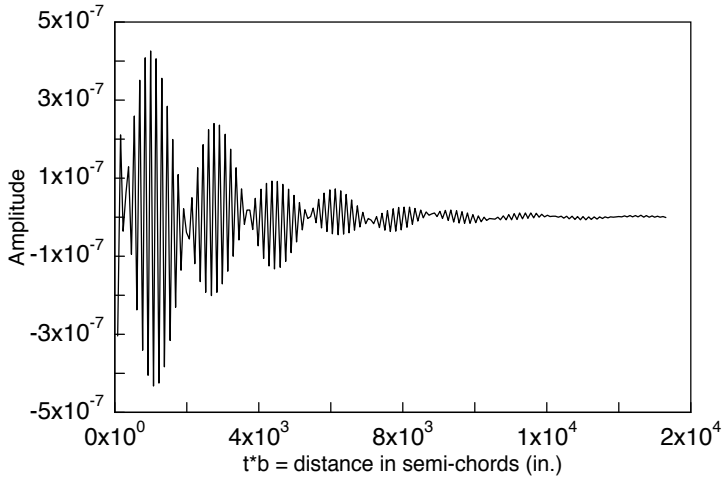

Figure 4.14: Time response of the closed-loop system (output θ) to sinusoidal disturbance input

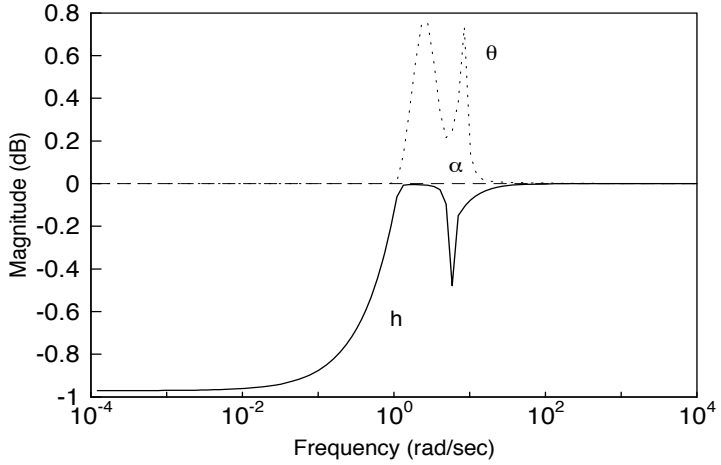

Figure 4.15: Output sensitivity transfer matrix

The characteristics of $\boldsymbol{\sigma}[\boldsymbol{S_o}(j\omega)]$ that are necessary for tracking step reference inputs and ensuring rejection of disturbances at the system output is shown in Fig. 4.15. The simulation shows that the disturbances entering at 6 rad/sec amplify the closed-loop response of the output θ with a magnitude of less than 0.25 dB. On the other hand, the same disturbances at the output h are rejected by 0.48 dB. This is to be expected as trade-off between sensitivity and complementary sensitivity functions $[\boldsymbol{S_o}(s) + \boldsymbol{T_o}(s) = \boldsymbol{I}]$ because from Fig. 4.11 it is indeed clear that outputs α and θ attenuate noise by a large magnitude, sometimes unnecessary at frequencies where its effect is least likely to occur. This shows that perhaps by assigning unequal weights (as opposed to those given in Eq. 4.21) to $\boldsymbol{W_1^{-1}}(s)$, with those corresponding to outputs α and θ weighed more strongly, better disturbance attenuation might have been achieved at those outputs. Nevertheless, for low frequency range (< 10 rad/sec) where the effect of gusts are more prominent, the plot shows that the disturbances at the outputs h and α never get amplified if not rejected whereas at θ they face little amplification. This plot also gives the measure of relative insensitiveness to low frequency wing/store parameter variations such as change in the c.g. location (x_θ) and radius of gyration (r_θ) of the store with flutter speed.

4.5.3 Perturbation Analysis

To evaluate the effectiveness of the closed-loop system to low frequency perturbations, the following two cases were tested.

Input Matrix Uncertainty

In this case, instead of the nominal $\boldsymbol{H}$ matrix (Section 2.5) the following perturbed matrix is assumed to represent a perfect actuator

$$\tilde{\boldsymbol{H}} = \begin{bmatrix} 0.2 \\ 0.5 \\ 1.4 \end{bmatrix} \tag{4.28}$$

The loop gains of the original and the perturbed systems can be used to calculate the equivalent output multiplicative uncertainty (i.e. reflecting the perturbation to the plant's output)

$$\boldsymbol{\Delta}(j\omega) = \frac{(\boldsymbol{G_{pert}K})(j\omega) - (\boldsymbol{G_{nom}K})(j\omega)}{(\boldsymbol{G_{nom}K})(j\omega)} \tag{4.29}$$

where the controller $\boldsymbol{K}(s)$ is designed based on the unperturbed nominal plant model $\boldsymbol{G}(s)$. Stability is guaranteed if the condition of Eq. (4.24) is satisfied at each frequency. The loop gains for original and perturbed systems a function of frequency are shown in Fig. 4.16.

The frequency response of the stability condition (Eq. 4.29) for the given input perturbation matrix is shown in Fig. 4.17. It is observed that at all the frequencies and particularly at lower frequencies where the parameter sensitivity is critical, the graph of maximum singular values of $\boldsymbol{\Delta}(j\omega)$ lies below that of the minimum singular values of $[\boldsymbol{I} + (\boldsymbol{G}(j\omega)\boldsymbol{K}(j\omega))^{-1}]$. This indicates that the stability is always guaranteed for the given parameter perturbation. Time responses to a pulse input of magnitude 1 on the perturbed open- and closed-loop systems are shown in Fig. 4.18. Up-until $100U_f$ the responses belong to the unperturbed open- and closed-loop systems and the later responses belong to that of the perturbed systems. In both perturbed and unperturbed cases, the output θ of the closed-loop response settles down relatively faster and has smaller amplitude than the corresponding open-loop response.

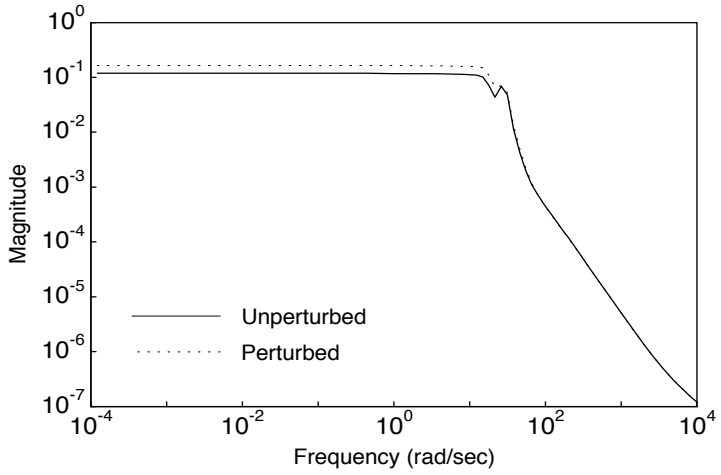

Figure 4.16: Loop gains of the perturbed and unperturbed system

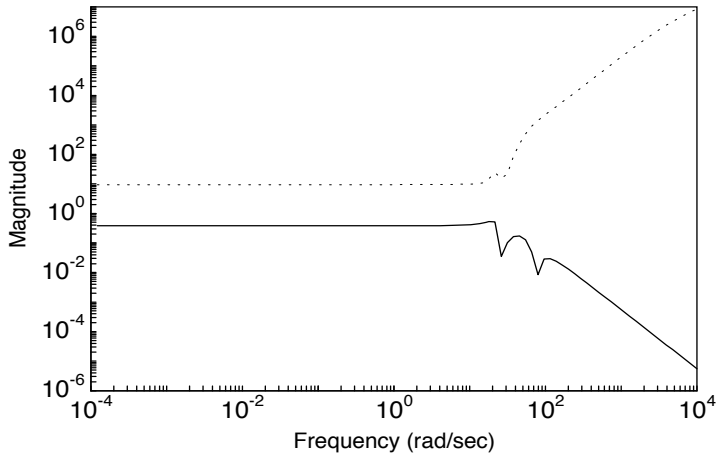

Figure 4.17: Stability test of Eq. (4.29) - solid $\boldsymbol{\sigma}[\boldsymbol{\Delta}]$, dashed $\underline{\boldsymbol{\sigma}}[\boldsymbol{I} + (\boldsymbol{GK})^{-1}]$

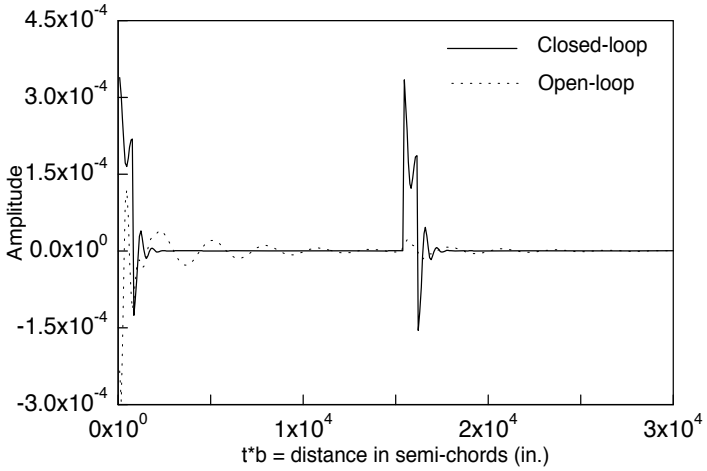

Figure 4.18: Pulse input response of open- and closed-loop systems (output θ)

Circulatory Store Aerodynamic Matrix Uncertainty

To make the controller to pass through a relatively more rigorous parametric test, all the zero terms due to lack of store aerodynamics are made non-zero. In addition, the actuator uncertainty is also kept for completeness. This amounts to modifying the elements of matrices corresponding to the circulatory part of the aerodynamics and are given by

$$\tilde{\boldsymbol{R}} = \begin{bmatrix} -2 \\ 0.69 \\ -2.3 \end{bmatrix} \quad \widetilde{\boldsymbol{S}}_{\mathbf{1}} = \begin{bmatrix} 1 & 1 & 1 \end{bmatrix} \quad \widetilde{\boldsymbol{S}}_{\mathbf{2}} = \begin{bmatrix} 1 & 0.652 & 1.8 \end{bmatrix} \quad \tilde{\boldsymbol{C}}_{\boldsymbol{nc}} = \begin{bmatrix} 0 & 153 & 0 \\ 0 & 99.756 & 0 \\ 0 & 250 & 0 \end{bmatrix} \tag{4.30}$$

Only some damping due to non-conservative store aerodynamics is assumed to be present ($\boldsymbol{C_{nc}}$ matrix) while it is assumed that the corresponding $\boldsymbol{M_{nc}}$ matrix remains unchanged. As before the singular value plot of the loop gains for the perturbed and the unperturbed cases are shown in Fig. 4.19.

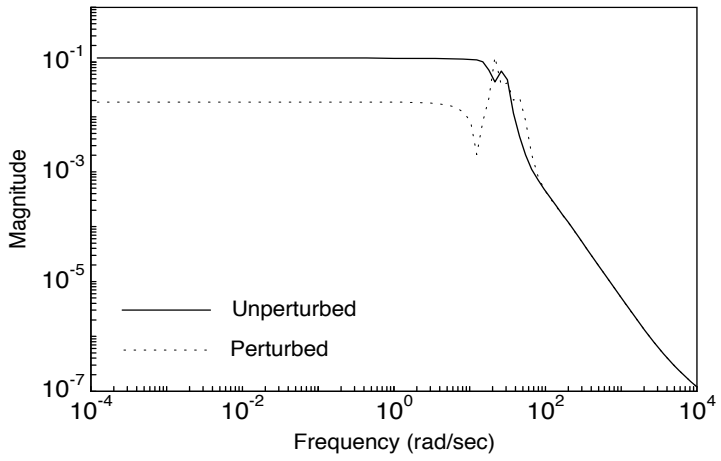

Figure 4.19: Loop gains of the perturbed and unperturbed system

It is observed that the loop gain for the perturbed system shows its effect more on the output h than on other outputs (not shown) at low frequencies. The stability condition Eq. (4.24) drawn as a function of frequency for the given input matrix perturbation is shown

in Fig. 4.20. It is observed that at all the frequencies and particularly at lower frequencies

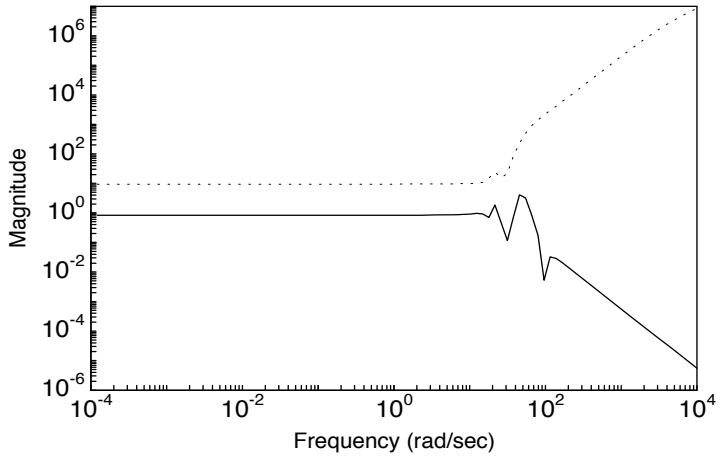

Figure 4.20: Stability test of Eq. (4.29) - solid $\boldsymbol{\sigma}[\boldsymbol{\Delta}]$, dashed $\underline{\boldsymbol{\sigma}}[\boldsymbol{I} + (\boldsymbol{GK})^{-1}]$

where the parameter sensitivity is critical, the graph of maximum singular values of $\boldsymbol{\Delta}(j\omega)$ is below that of the minimum singular values of $[\boldsymbol{I} + (\boldsymbol{G}(j\omega)\boldsymbol{K}(j\omega))^{-1}]$. This indicates that the stability is always guaranteed for the given parameter perturbation. Initial condition responses of the perturbed open- and closed-loop systems are shown in Fig. 4.21 and Fig. 4.22 respectively. Up-until $100U_f$ the responses belong to the unperturbed open- and closed-loop systems and the later responses belong to that of the perturbed systems.

In both perturbed and unperturbed cases, the output h of the closed-loop response settles down significantly faster and has smaller amplitude than the corresponding open-loop response. Moreover, for the same perturbation, the LQG/LTR compensated system was unstable whereas the $\mathcal{H}_\infty$ compensated system led to stability.

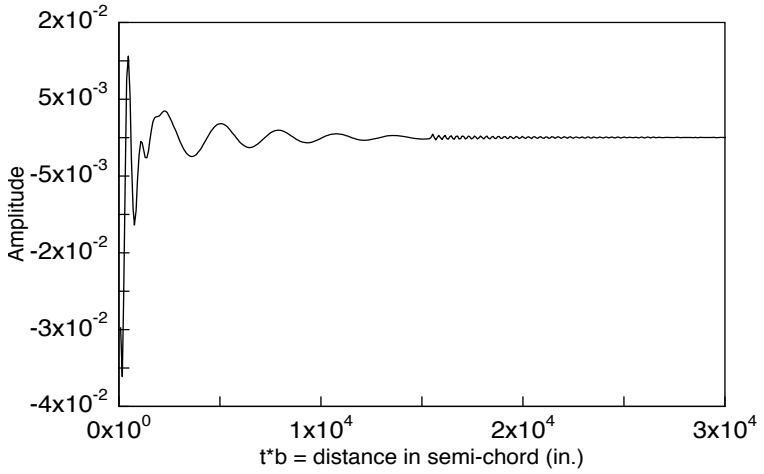

Figure 4.21: Initial condition response of open-loop system (output h)

4.6 Summary

The wing/store flutter model in this chapter is first formulated into a two port form (Fig. 4.1) where the objective is to find a controller $\boldsymbol{K}(s)$ that minimizes the $\mathcal{H}_\infty$ norm of the transfer matrix between $\boldsymbol{w}$ to $\boldsymbol{z}$ given by the lower linear fractional transformation of the generalized plant $\boldsymbol{P}(s)$. Physically the input signal vector $\boldsymbol{w}$ consist of all exogenous inputs comprising of plant disturbances, sensor noises and model-error outputs, while the output signal z consists of the outputs of the weighted cost functions whose minimization is desired. Signals $\boldsymbol{y}$ and u represent the sensor measurements and control input into the system respectively.

The generalized plant $\boldsymbol{P}(s)$ is obtained by transforming a multi-target objective functions (mixed-sensitivity) that are first identified based on the requirement of simultaneously achieving good nominal performance as well robust stability. A set of weighting functions are chosen to achieve best compromise between conflicting objectives ($\boldsymbol{S_o}(s)$ and $\boldsymbol{T_o}(s)$). The selection is made based on a set of specifications, such as the need to reject disturbances entering within a particular frequency range and a certain closed-loop bandwidth and roll-off

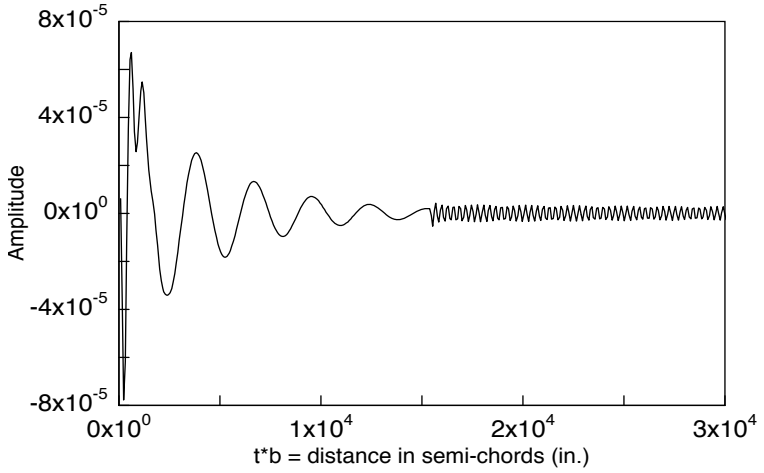

Figure 4.22: Initial condition response of closed-loop system (output h)

rate to ensure sufficient stability margin to tolerate modeling errors.

The effectiveness of the designed controller in attaining the desired robust stability and the nominal performance measures can be seen at a glance by inspecting the plot of the cost function (Fig 4.4). It is seen that cost function responses of the outputs θ and α at low frequencies have a magnitude of approximately 1 (0 dB) implying that the the sensitivity properties of these outputs (dictated by $\boldsymbol{S_o(s)}$) are under-achieved (Fig. 4.15). On the other hand, the output h at these frequencies demonstrated achievement of the desired objective. At higher frequencies where greater stability robustness (dictated by $\boldsymbol{T_o(s)}$) margins are required, the cost functions corresponding to the three outputs demonstrate achievement (in fact, over-achievement), with outputs α and θ showing relative over-achievement to output h (Fig. 4.11). Intuitively, this is to be expected since the sensitivity and complementary sensitivity functions together have a water-bed effect, where if one is achieved then the other won't and vice versa.

The above conclusions obtained by inspection of the cost function plot is confirmed by the robust stability and nominal performance analyses (Sections 4.5.1-4.5.3). For instance, when the modeling errors are reflected at the output, a minimum tolerance margin of $\pm$

298% is obtained at all frequencies. Step responses (Fig. 4.7) obtained by perturbing the closed-loop systems multiplicatively at flutter speed indicates that the controller stabilizes the unstable open-loop system.

For nominal performance analysis, the controller was designed for the plant at a sub-critical flutter speed. For a step input, the closed-loop system demonstrated a relatively faster transient response and smaller settling time than the open-loop system. There is however a difference in the steady-state values of the compensated and uncompensated systems. This is due to the absence of integrators in the closed-loop system. In other words, the roll-off rate at low frequencies is not sufficient enough for perfect tracking. Although this could be avoided by appending integrators at each of the outputs, there is a disadvantage of having to deal with an increased order of the plant resulting in a higher-order controller. The compensated system is also excited by a sinusoidal signal of frequency 6 rad/s (a typical disturbance frequency entering at the input of the plant through $\boldsymbol{w}$ of Eq. 2.29) and compared with the corresponding open-loop response. It is observed from the frequency plot of the output θ that the disturbances get rejected by as much as 62 dB. This is also seen from the reduction in the peak magnitudes of time responses of the open- and the closed-loop systems subjected to a sinusoidal input disturbance. To study the effect of parameter variations, for instance due to error in modeling actuator vector $\boldsymbol{H}$ and/or matrix corresponding circulatory store aerodynamics, the time responses plotted indicate that for both the cases (Figs. 4.18, 4.21-4.22) the system is capable of maintaining the stability.

Chapter 5

Robust Adaptive Controller Design

This chapter starts with a brief discussion on why adaptive control strategy is needed (Section 5.1) for the present wing/store flutter problem. Section 5.2 introduces to a robust linear quadratic adaptive control problem that is proposed to be used for this study. Subsections 5.2.1-5.2.3 describe various modifications that are needed to make the gradient method based adaptive algorithm more robust to modeling uncertainties. Subsection 5.2.4 discusses about the adaptive linear quadratic controller design. Section 5.3 puts together all the steps involved in the algorithm, which is then followed by results and discussions on the simulations obtained (Section 5.4). Finally Section 5.5 summarizes this chapter.

5.1 Introduction

During combat maneuvers of a military aircraft carrying underwing stores, many critical parameters change that effect the performance of the system and sometimes may lead to flutter. A particular combat situation is when the aircraft ejects stores (missiles). This is frequently accompanied by simultaneous changes in some or all parameters such as radius of gyration, location of store center of gravity, aerodynamic center position, etc. In this chapter,

an adaptive control algorithm is implemented to study if the on-line estimation/control scheme works well for the present wing/store model. The adaptive controller is designed at sub-critical flutter speed with the objective of investigating if any increase in performance and/or robustness is achieved in the presence of modeling uncertainties, when the system is subjected to sudden change in mass parameter value.

Motivation for continuous-time design

1. to be consistent with the controller design presented in the earlier chapters,
2. real-world problems are all stated in and enough to understand in continuous-time domain,
3. although controllers are often implemented in digital or discrete-time setting, designing them first in continuous domain would help interpret and address system characteristics such as relative degree, zero location etc. Moreover controller sampling is always done after the designing stage.

5.2 Robust Linear Quadratic Adaptive Control Problem

Previous research effort on the feasibility of using the adaptive control concept has proved successful in addressing the issues pertaining to the wing/store flutter problem Ref. [7]. The earlier method of suppressing flutter was however different as they used conventional techniques of actuating the control surface (ailerons) to negate the effects of instability causing aerodynamic forces. Moreover at that time, the adaptive strategies lacked current day modifications for robustness. In this work, a linear quadratic adaptive control concept is presented for a decoupler pylon mounted store. Modifications proposed in the late eighties and early nineties are included in the adaptive control algorithm to robustify the closed-loop wing/store flutter control system.

Adaptive control is typically categorized into indirect (explicit) and direct (implicit) techniques. Indirect adaptive control involves on-line explicit estimation of plant parameters which are then used for the controller design. That is, as the plant parameter changes, they are estimated and new controller parameters are constructed from the estimated plant parameters as if they were the true plant parameters (Certainty Equivalence Principle). This process is indirect in the sense that controller parameters are indirectly estimated (as opposed to direct estimation) from estimated plant parameters. In direct adaptive control scheme, the plant is first reparametrized in terms of controller parameters (that are also unknown) and then standard estimation techniques are used to implicitly estimate plant parameters. Clearly for low-order simple control laws, the reparametrization of the plant is possible, but is quite complex in case of complicated ones. In this work, a continuous-time

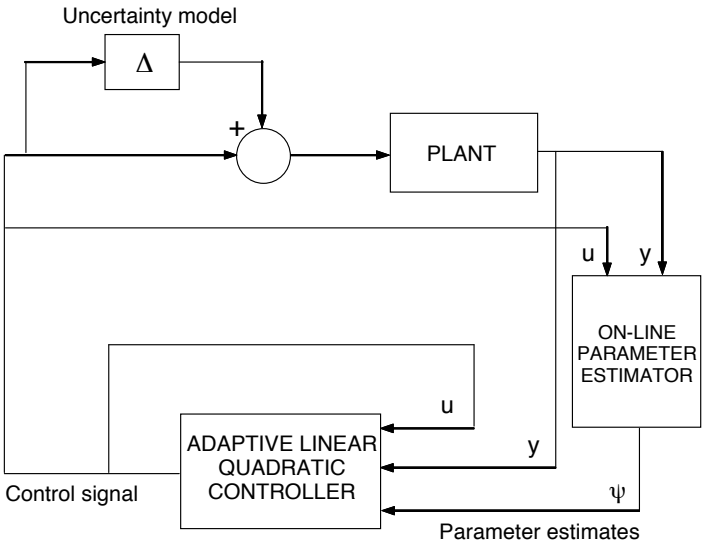

Figure 5.1: Block diagram of the adaptive estimation/control scheme

nonlinear indirect auto-adaptive feedback control design is undertaken for the performance enhancement and stability robustification of the wing/store flutter suppression problem. It is assumed that controller parameters and control law are designed based on estimated plant (linear) parameters defined by the polynomial coefficients of the single-input single-output system (Fig. 5.1). This type of adaptive control method is also known as a Self-Tuning

Regulator (STR) technique. An adaptive law based on gradient method is used for parameter estimation and is modified with the algorithms of leakage and dynamic normalization to robustify the adaptation. The reader is referred to Refs. [38] and [39] for excellent discussion and analytical proofs on above modifications.

5.2.1 Plant Parametrization

With the output taken to be a linear combination of the three primary degrees-of-freedom equally weighted, the system is represented in a transfer function form as

$$\begin{aligned} y &= \frac{Z}{R}(1+\Delta_m)u \\ &= \frac{b_6 s^6 + b_5 s^5 + \cdots\cdots + b_1 s + b_0}{s^8 + a_7 s^7 + \cdots\cdots + a_1 s + a_0}(1+\Delta_m)u \end{aligned} \tag{5.1}$$

which has a relative degree of 2. A common approach to represent such single-input single-output model for parameter estimation and control applications is the linear parametrization form where the unknown parameters are separated from the available signals and expressed as [38]

$$\begin{aligned} \frac{s^8}{\Lambda(s)}y &= [b_6, b_5, \ldots, b_0, a_7, \ldots, a_1, a_0]\left[\frac{\boldsymbol{\alpha_i^T}(s)}{\Lambda(s)}u, -\frac{\boldsymbol{\alpha_i^T}(s)}{\Lambda(s)}y\right] \\ &\quad + \frac{[b_6, b_5, \ldots, b_0]\boldsymbol{\alpha_{i-1}^T(s)}}{\Lambda(s)}\Delta_m(s)u \end{aligned} \tag{5.2}$$

where $\Lambda(s) = (s+\lambda_f)^8$, $\lambda_f > 0$ and $\boldsymbol{\alpha_i^T(s)} = [s^i, s^{i-1}, \ldots, 1], i = 7$. Here an 8th order stable filter $1/\Lambda(s)$ is introduced to avoid the use of derivatives of the only available signals u and y. In notational form, Eq. (5.2) is written as

$$z = \boldsymbol{\psi^T \phi} + \eta \tag{5.3}$$

where the signal z constitutes the 8th derivative of the output filtered by $(s+\lambda_f)^8$, $\boldsymbol{\psi}$ is a vector of all unknown parameters, $\boldsymbol{\phi}$ consists of all measurable signals, and η is the disturbance term due to modeling error.

5.2.2 Dynamic Normalization

In this modification, the input and output signals are normalized via the normalized estimation error [40] defined as

$$\epsilon = \frac{z - \widehat{z}}{m^2} \tag{5.4}$$

where $m^2 = 1 + n_s^2$ and $n_s^2 = m_n$ is the dynamic normalizing signal designed so that ϕ/m and the modeling error term η/m is always bounded. This allows the designer the freedom of not having the plant input signal bounded *apriori*. The normalizing signal is generated from the differential equation

$$\dot{m}_n = -\delta_0 m_n + u^2 + y^2 \qquad m_n(0) = 0 \tag{5.5}$$

Another advantage of normalization is that the unbounded modeling error term can be considered as a bounded input disturbance to the adaptive law for which an adaptive control law can then be designed and analyzed at relative ease. Applying gradient method on an instantaneous quadratic cost function $J(\psi) = (z - \psi^T\phi)^2/2m^2$, the minimizing trajectory governing the adaptive law is generated by

$$\dot{\boldsymbol{\psi}} = \boldsymbol{\Gamma}\epsilon\boldsymbol{\phi} \tag{5.6}$$

where $\boldsymbol{\Gamma} = \boldsymbol{\Gamma}^{\boldsymbol{T}} > \mathbf{0}$ is the adaptation gain or the weighting matrix used to control the rate of convergence of various parameters.

5.2.3 Leakage

In the absence of a persistently exciting signal, a bounded input disturbance such as the one due to the normalized modeling error, may generally cause parameter estimates to drift to infinity with time. Moreover in the presence of an adaptive control law, high-gain feedback generally excites unmodeled dynamics and leads to unbounded plant states.

Increasing the adaptation gain $\mathbf{\Gamma}$ too large also causes excitation of the high frequency unmodeled dynamics. To avoid parameter drift and high-gain instability, the original integrator in the adaptation law of Eq. (5.6) is modified [41] to include additional term giving it the property of a low-pass filter.

$$\dot{\boldsymbol{\psi}} = \mathbf{\Gamma}\epsilon\boldsymbol{\phi} - \mathbf{\Gamma}w\boldsymbol{\psi} \tag{5.7}$$

The idea of modifying the adaptive law is to make the time derivative of the Lyapunov function (used to analyze adaptive scheme) negative whenever parameter estimates exceeds certain bounds. The choice of w is governed by a continuous switching-σ modification

$$w(t) = \sigma_s = \begin{cases} 0 & \text{if } |\boldsymbol{\psi}(t)| < M_0 \\ \sigma_0 \left(\frac{\left|\boldsymbol{\psi}(t)\right|}{M_0} - 1 \right) & \text{if } M_0 \leq |\boldsymbol{\psi}(t)| \leq 2M_0 \\ \sigma_0 & \text{if } |\boldsymbol{\psi}(t)| > 2M_0 \end{cases} \tag{5.8}$$

where $\sigma_0 > 0$ is a small constant and M_0 is an upper bound for the unknowns $|\boldsymbol{\psi}|$. The idea behind switching algorithm is that whenever estimated parameters exceed certain bound dictated by M_0, the pure integral is converted to a leaky one and if the estimated parameters are within the threshold bound, then the switching is turned off.

5.2.4 Linear Quadratic Adaptive Controller

Here an adaptive linear quadratic regulator design with an on-line state observer is used for control law. At each frozen time t, the information from the output, input and the estimated parameters generated by the adaptive law are used for the purpose. Certainty equivalence approach is assumed wherein the unknown polynomial coefficients are replaced by their estimates. Using the famous separation principle, these estimated parameters are then used to solve the Algebraic Riccati Equation (ARE) on-line and for the design of a full-order Luenberger observer, independently.

Since this is a regulator problem, the state-space realization in the observer canonical form is given by

$$\dot{\hat{\boldsymbol{e}}} = \hat{\boldsymbol{A}}\hat{\boldsymbol{e}} + \hat{\boldsymbol{B}}u - \hat{\boldsymbol{K}}_{\boldsymbol{0}}(\boldsymbol{C}^{\boldsymbol{T}}\hat{\boldsymbol{e}} - y) \tag{5.9}$$

where

$$\hat{\boldsymbol{A}} = \begin{bmatrix} -\hat{a}_7 & 1 & 0 & \dots & \dots & 0 \\ -\hat{a}_6 & 0 & 1 & \dots & \dots & 0 \\ \vdots & \vdots & \vdots & \ddots & \vdots & \vdots \\ -\hat{a}_0 & 0 & 0 & \dots & \dots & 1 \end{bmatrix} \quad \hat{\boldsymbol{B}} = \begin{bmatrix} 0 \\ \hat{b}_6 \\ \vdots \\ \hat{b}_0 \end{bmatrix} \quad \boldsymbol{C} = \begin{bmatrix} 1 & 0 & \dots & 0 \end{bmatrix} \tag{5.10}$$

Here $\hat{\boldsymbol{e}}$ is the state of the full-order observer and the control law is given by $u = -\hat{\boldsymbol{K}}_{\boldsymbol{c}}\hat{\boldsymbol{e}}$ where the feedback gain $\hat{\boldsymbol{K}}_{\boldsymbol{c}}$ is obtained by solving the algebraic Riccati equation

$$\hat{\boldsymbol{A}}^{\boldsymbol{T}}\boldsymbol{P} + \boldsymbol{P}\hat{\boldsymbol{A}} - \boldsymbol{P}\hat{\boldsymbol{B}}R_c^{-1}\hat{\boldsymbol{B}}^{\boldsymbol{T}}\boldsymbol{P} + \boldsymbol{C}\boldsymbol{C}^{\boldsymbol{T}} = \boldsymbol{0} \tag{5.11}$$

pointwise in time as and when the parameters are estimated. For faster estimation, the eigenvalues of observer dynamics $\hat{\boldsymbol{A}} - \hat{\boldsymbol{K}}_{\boldsymbol{0}}\boldsymbol{C}^{\boldsymbol{T}}$ are placed 3 to 5 times farther to the left of those of $\hat{\boldsymbol{A}} - \hat{\boldsymbol{K}}_{\boldsymbol{c}}\hat{\boldsymbol{B}}$.

In the above adaptive optimal pole-placement feedback law, the stabilizability of the pair $(\hat{\boldsymbol{A}}, \hat{\boldsymbol{B}})$ cannot always be guaranteed at each frozen time t. This problem arises because there is no way to avoid the cancellation of right-half plane poles and zeros without any additional modifications. One of the approaches suggested [42] involves constructing a convex set of all unknown parameters $\in \Re^{2n}$ such that the absolute value of the determinant of the Sylvester matrix of estimated polynomial coefficients is always greater than certain known *apriori* lower bound. Knowledge of such a known convex bounded set for higher order plants is difficult to construct and is rather a strong assumption. In this work, the stabilizability of $(\hat{\boldsymbol{A}}, \hat{\boldsymbol{B}})$ is assumed $\forall t \geq 0$ and the simulation studies presented also validate this assumption.

5.3 Robust Adaptive Linear Quadratic Control Algorithm

In this section, the algorithm described earlier is summarized.

1. The actual plant is modeled as

$$y = \frac{Z}{R}(1 + \Delta_m)u$$

2. Where the nominal plant model is

$$\begin{aligned} y &= \frac{Z(s)}{R(s)}u \\ Z(s) &= \boldsymbol{\psi_b^{*T}}\boldsymbol{\alpha}(s) \\ R(s) &= s^n + \boldsymbol{\psi_a^{*T}}\boldsymbol{\alpha}(s) \\ \boldsymbol{\psi}^* &= [\boldsymbol{\psi_b^{*T}}, \boldsymbol{\psi_a^{*T}}]^{\boldsymbol{T}} \\ \boldsymbol{\alpha}(s) &= [s^{n-1}, s^{n-2}, \ldots, s, 1]^T \end{aligned}$$

3. It is assumed that the polynomial R is monic whose degree n is known. Also, the transfer function of the modeled part of the plant $Z(s)/R(s)$ is assumed to be strictly proper where the polynomials $Z(s)$ and $R(s)$ are assumed to be coprime.

4. Parametrize the actual model into

$$z = \boldsymbol{\psi^{*T}}\boldsymbol{\phi} + \eta$$

where

$$\begin{aligned} z &= \frac{s^n}{\Lambda(s)}y \\ \boldsymbol{\phi} &= \left[\frac{\boldsymbol{\alpha^T}(s)}{\Lambda(s)}u, -\frac{\boldsymbol{\alpha^T}(s)}{\Lambda(s)}y\right]^T \\ \eta &= \frac{Z}{R}\Delta_m u \\ \Lambda(s) &= (s + \lambda_f)^n \qquad \lambda_f > 0 \end{aligned}$$

5. Adaptive law using gradient algorithm is given by

$$\dot{\boldsymbol{\psi}} = \boldsymbol{\Gamma}\epsilon\boldsymbol{\phi} - \boldsymbol{\Gamma}w\boldsymbol{\psi} \qquad \boldsymbol{\Gamma} = \boldsymbol{\Gamma}^{\boldsymbol{T}} > \mathbf{0}$$

where

$$\epsilon = \frac{z - \boldsymbol{\psi}^{\boldsymbol{T}}\boldsymbol{\phi}}{m^2}$$

$$m = \text{normalizing signal}$$

$$w = \text{leakage term}$$

6. Normalizing signal m is obtained as

$$m^2 = 1 + n_s^2$$

where

$$n_s^2 = m_n$$

$$\dot{m}_n = -\delta_0 m_n + u^2 + y^2, \qquad m_n(0) = 0$$

7. Leakage modification w with switching term σ_0 is given by

$$w = \sigma_s = \begin{cases} 0 & \text{if } |\boldsymbol{\psi}(t)| < M_0 \\ \sigma_0 \left(\frac{\left|\boldsymbol{\psi}(t)\right|}{M_0} - 1 \right) & \text{if } M_0 \leq |\boldsymbol{\psi}(t)| \leq 2M_0 \\ \sigma_0 & \text{if } |\boldsymbol{\psi}(t)| > 2M_0 \end{cases}$$

8. Thus $\hat{Z}(s,t)$ and $\hat{R}(s,t)$ are generated by the expressions

$$\hat{Z}(s,t) = \boldsymbol{\psi}_{\boldsymbol{b}}^{\boldsymbol{T}}(t)\boldsymbol{\alpha}(s)$$

$$\hat{R}(s,t) = s^n + \boldsymbol{\psi}_{\boldsymbol{a}}^{\boldsymbol{T}}(t)\boldsymbol{\alpha}(s)$$

9. To generate the estimated "states", a state observer is used

$$\dot{\hat{\boldsymbol{e}}} = \hat{\boldsymbol{A}}\hat{\boldsymbol{e}} + \hat{\boldsymbol{B}}u - \hat{\boldsymbol{K}}_{\mathbf{0}}(\boldsymbol{C}^{\boldsymbol{T}}\hat{\boldsymbol{e}} - y_p)$$

where

$$\hat{\boldsymbol{A}} = \begin{bmatrix} -\hat{a}_7 & 1 & 0 & \dots & \dots & 0 \\ -\hat{a}_6 & 0 & 1 & \dots & \dots & 0 \\ \vdots & \vdots & \vdots & \ddots & \vdots & \vdots \\ -\hat{a}_0 & 0 & 0 & \dots & \dots & 1 \end{bmatrix} \quad \hat{\boldsymbol{B}} = \begin{bmatrix} 0 \\ \hat{b}_6 \\ \vdots \\ \hat{b}_0 \end{bmatrix}$$

$$\begin{aligned} \boldsymbol{C} &= \begin{bmatrix} 1 & 0 & \dots & 0 \end{bmatrix} \\ \hat{\boldsymbol{K}}_{\boldsymbol{o}} &= \boldsymbol{a}^* - \boldsymbol{\psi_1} \\ A_o^* &= \prod_{i=1}^{n} (s + \beta p_i) = s^n + \boldsymbol{a}^{*\boldsymbol{T}} \boldsymbol{\alpha_{n-1}}(s) \end{aligned}$$

where p_i are the controller poles calculated using adaptive LQR and β is the factor by which adaptive observer poles are placed with reference to controller poles.

10. Calculation of adaptive controller poles consists of

$$p_i = eig(\hat{\boldsymbol{A}} - \hat{\boldsymbol{B}}\hat{\boldsymbol{K}}_{\boldsymbol{c}}) \qquad i = 1, 2, \dots, n$$

where

$$\begin{aligned} \hat{\boldsymbol{K}}_{\boldsymbol{c}} &= R_c^{-1} \hat{\boldsymbol{B}}^{\boldsymbol{T}} \boldsymbol{P} \\ \boldsymbol{P} &= \boldsymbol{P}^{\boldsymbol{T}} > 0 \quad \text{is calculated from the algebraic Riccatti equation} \end{aligned}$$

$$\hat{\boldsymbol{A}}^{\boldsymbol{T}} \boldsymbol{P} + \boldsymbol{P}\hat{\boldsymbol{A}} - \boldsymbol{P}\hat{\boldsymbol{B}}\boldsymbol{R}_{\boldsymbol{c}}^{-\boldsymbol{1}}\hat{\boldsymbol{B}}^{\boldsymbol{T}}\boldsymbol{P} + \boldsymbol{C}\boldsymbol{C}^{\boldsymbol{T}} = \boldsymbol{0}$$

are calculated at each time t.

11. The adaptive control law is given by

$$u = -\hat{\boldsymbol{K}}_{\boldsymbol{c}}(t)\hat{\boldsymbol{e}}$$

12. The design variables are $\lambda_f > 0$, $\boldsymbol{\Gamma > 0}$, $\sigma_0 > 0$, $\beta > 0$, and $R_c > 0$.

5.4 Simulation Results

In the algorithm given in earlier section, the values assigned to the design variables are: the adaptation gain $\mathbf{\Gamma} = \boldsymbol{I_{15}}$, the switching parameter $\sigma_0 = 200$, the filter parameter $\lambda_f = 2$, the observer pole factor $\beta = 3$, and the control weighting $R_c = 10$. The simulation consists of a release of 500 lb mass bomb from a rack of 2265 lb at the 20th non-dimensional time unit.

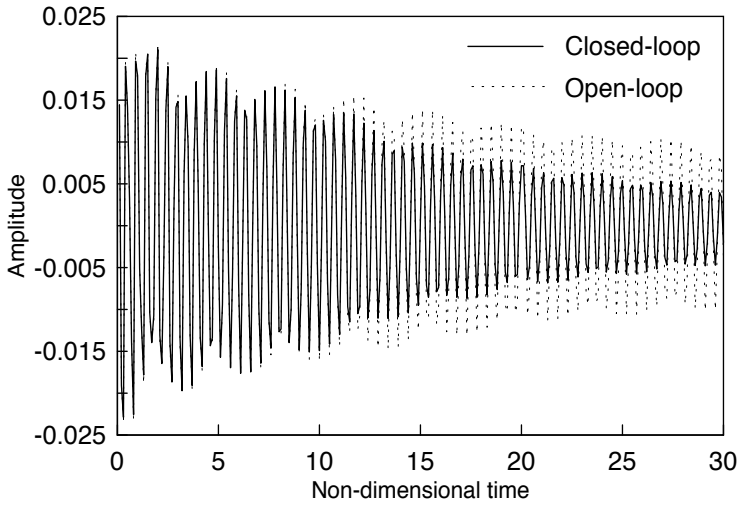

Figure 5.2: Open- and closed-loop response of store pitch angle (θ)

Figure 5.2 shows the response of the store pitch angle as a function of time. It is observed that at the instant of store release, there is insignificant change in the response. This is because the simulation ensures that the initial conditions of the states at the 20th non-dimensional time unit are the values of the states at the 19.9th non-dimensional time unit (continuous evolution). When compared to the open-loop's response, the closed-loop system demonstrates relatively faster settling time and reduced magnitude of vibration. It is to be noted that the closed-loop response plotted in Fig. 5.2 is with the uncertainty model included, whereas the open-loop response does not include the model. The response of the open-loop with the multiplicative uncertainty model included becomes unstable (not shown)

as soon as the system is given a perturbation of the above nature.

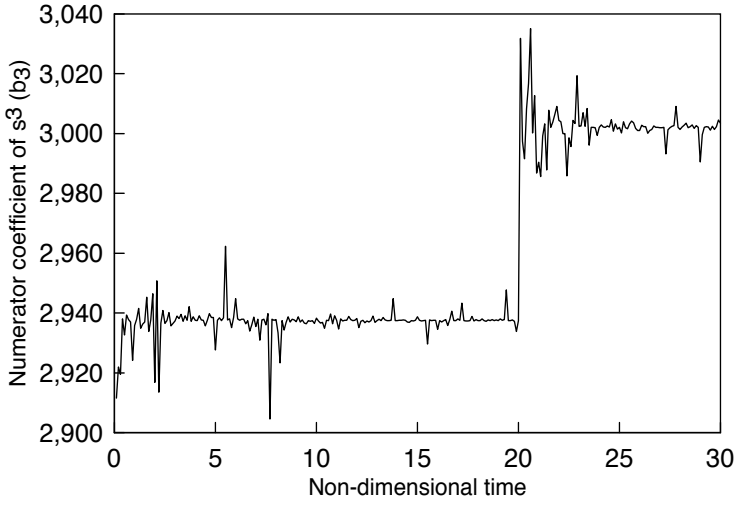

Figure 5.3: Estimation of parameter $\psi_4 = b_3 =$ coefficient of s^3

A very obvious change is seen in the parameter estimation response where the estimated parameters are the coefficients of the numerator and denominator polynomials, totalling to 15 in number. A representative plot of a parameter from numerator (coefficient of s^3) is shown in Fig. 5.3. With the initial values for these coefficients being different, the search for the true parameter takes place, with the true parameter being the coefficients corresponding 2265 lb mass. At the instant of store release, the true and unknown mass suddenly jumps to 1765 lb. This is clear from the step change in the estimated parameter response at the 20th non-dimensional time unit. Again the search process continues as before as governed by the adaptation law.

Figure 5.4 illustrates the percentage error between the true unknown parameter and the estimated parameter values corresponding to the coefficient shown in Fig. 5.3. It is observed that the percentage errors are negligible and leads to the conclusion the adaptation is effective in estimating the unknown parameters.

The time response of dynamic normalization signal (m) that is used to bound the

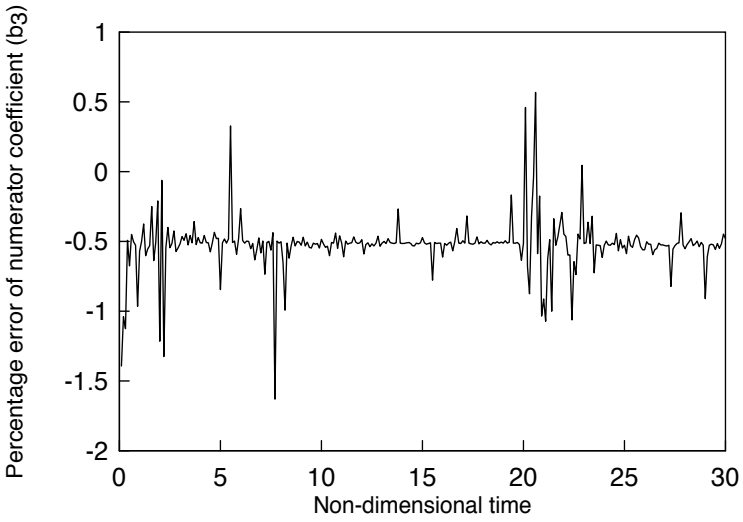

Figure 5.4: Percentage estimation error of $\psi_4 = b_3 =$ coefficient of s^3

available signals ($\boldsymbol{\phi}$) and η that is related to u through the modeling error transfer function $[\Delta_m(s)]$ is shown in Fig. 5.5. It is observed that both $\boldsymbol{\phi}$ and η are unbounded during the entire course of simulation, with the magnitude of unboundedness being large at the start of the simulation and at the instant of store release. The dynamic normalizing signal attempts to approach 1 which indicates that normalizing is not required anymore.

A representative time history of a state ($\hat{e}_1$) of the estimator (observer) is shown in Fig. 5.6. The initial conditions on the state estimator are zero both at the start of the simulation as well as when the store is ejected. This is as opposed to the concept of evolution which was applied to the actual states (outputs) of the system. Alternately, one could think of the situation that just before the instant of store release, the adaptation is switched-off and is switched-on again. At this instant, the adaptive algorithm lost track of the previous values of the estimator states as well as the unknown parameters. So it essentially starts off right from scratch, namely, zero initial conditions for the estimator states and an initial guess for the unknown coefficients (parameters).

The corresponding control history ($u = -\hat{\boldsymbol{K}}_{\boldsymbol{c}}\hat{\boldsymbol{e}}$) is shown in Fig. 5.7, where the peak value of the control effort is around 0.06 units. At the instant when the store is released, the

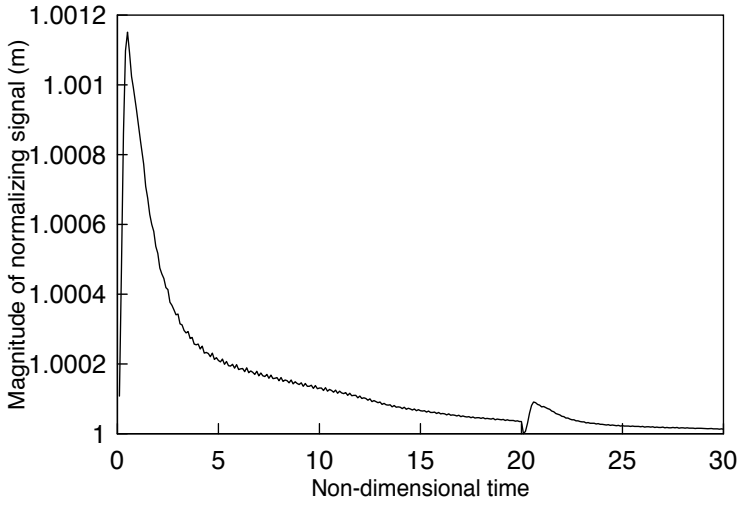

Figure 5.5: Dynamic normalization signal m

actuator response shows signs of perturbation in its simulation. This is because the control effort is being put in to the system to estimate and control the unknown parameters back. It remains to be seen (work in progress) whether the peak value is within the limits of actuator saturation value. If it is not, then the control weighting λ_f can appropriately be modified to accommodate for the limitations.

5.5 Summary

In this chapter, an indirect adaptive control algorithm is implemented for the wing/store flutter model. The schemes involves on-line estimation of plant parameters that are used for the design of adaptive control which is based on linear quadratic optimal control theory. The adaptive law for on-line parameter estimation is based on gradient method that is modified with the algorithms of leakage and dynamic normalization to robustify the adaptation process.

The implementation of self-tuning regulator algorithm demands that the plant be first

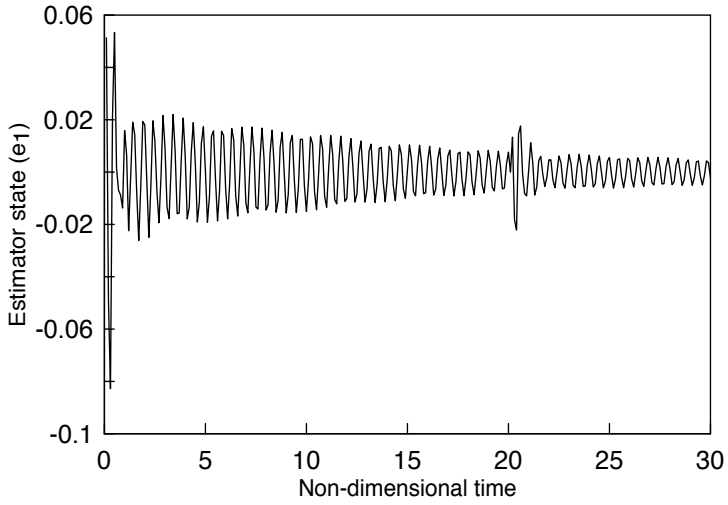

Figure 5.6: Time history of estimation state $\hat{e}_1$ of the adaptive observer

reparametrized into a form which is a function of unknown parameters ($\boldsymbol{\psi}$), all measurable signals ($\boldsymbol{\phi}$) and η the disturbance term due to modeling error. Further since the parametrized model is restricted to be a SISO model, a linear combination of the equally weighted three degrees-of-freedom is considered for simulation purposes. To avoid the concern of a lack of *apriori* bounded input u, the input and output signals are normalized. This has an added advantage that the uncertainty model error term can be regarded as a bounded disturbance term to the plant. Applying the gradient method to an instantaneous normalized quadratic cost function yeids the desired adaptive law (Eq. 5.6) for parameter estimation. The adaptation law is further modified to to give it the property of a low-pass filter (Eq. 5.7) that avoids the high-gain instability and the associated parameter drift that the original adaptation law typically exhibits.

The design of a linear quadratic adaptive controller involves the use of information from the output, input and estimated parameters for the design of adaptive feedback and the full-order observer gain matrices. The simulations show that the designed closed-loop system is robust to given unstructured as well as structured perturbations. The unstructured perturbation is given in the form of an input multiplicative uncertainty model approximating

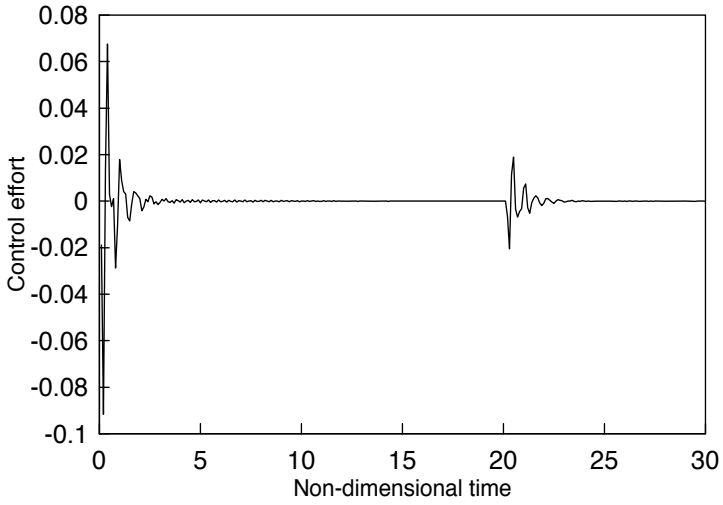

Figure 5.7: Control authority

the error in store aerodynamics while the structured perturbation is given in the form of a sudden variation in the store mass parameter due to the release of an under-wing store. The effectiveness of the adaptive control scheme is measured in terms of the smoothness of the response of the output, the error in parameter estimation and the control authority, all of which show satisfactory behavior without any unrealistic deviations.

Chapter 6

Conclusions and Future Work

The focus of this work was to investigate an active method of enhancing the performance and robustifying the stability of a wing/store flutter suppression system. The present work is built upon a wing/store flutter suppression system consisting of a decoupler pylon mounted store with pitch-pivot mechanism proposed by Reed [11]. The aim of the new concept presented in this work is to replace the passive spring-damper elements with an active element, namely, a piezoceramic strut that consists of a series of thin circular plates laminated on opposite faces with piezoceramic material. The poled directions of the piezoceramics are aligned so that a voltage applied across the element contracts on one side and expands on the other. The plate bending is then translated into an axial motion along the strut. Modern state-space based controllers have been implemented for the first time in literature to study the various performance and stability issues of the proposed concept. The overall conclusion reached of this simulation study is that an active wing/store flutter suppression system using a robust control law based on $\mathcal{H}_\infty$ theory yields relatively favorable results when compared to an uncompensated passive decoupler pylon mounted store flutter suppression system. The favorable results include robustness of the system to modeling uncertainties and an increase in performance in terms of disturbance rejection, noise attenuation, and insensitiveness to parameter variations. Further, preliminary simulation study

of the plant with a robust adaptive controller indicated that on comparison with the passive wing/store flutter suppression system, an increase in performance and stability can be obtained during store release event which is crucial during combat maneuvers of an aircraft.

Specific conclusions of this dissertation are:

1. Use of an active strut as a decoupler pylon increases the wing/store flutter speed substantially over that of a rigidly attached store, provided the strut's stiffness property satisfies Reed's criterion.

2. Coupled with an appropriate controller, the system is shown to have increased performance in terms of withstanding parameter variations, rejecting unwanted output disturbances, attenuation of noises, and more importantly an increased robust stability margin for uncertainties in modeling errors.

3. $\mathcal{H}_\infty$ controller compensated system demonstrated better overall performance and robust stability over LQG/LTR controller, under approximately the same given maximum control-energy constraint. The $\mathcal{H}_\infty$ theory based controller has the advantage of assigning weights more intuitively by means of sensitivity and complmentary sensitivity weights whose realm of action is restricted to frequency ranges that are typically independent of each other.

4. An approximate multiplicative uncertainty model, derived to represent the error due to neglecting store aerodynamics, appears to be an effective tool in analyzing the robust stability of the closed-loop wing/store flutter model.

5. Preliminary investigations with robust adaptive controller based on gradient law and linear quadratic controller has shown promising results in terms of the ability of system to track unknown parameters as well maintaining performance and stability in the presence of multiplicative uncertainties during store release event.

6.1 Conclusions

Detailed contributions and key conclusions of this dissertation are illustrated below chapter-wise:

Chapter 2: A typical section model is used for the structural model of the wing and a two-dimensional incompressible aerodynamics theory is used to model the aeroloads around the wing. The aerodynamics around the store is however neglected. The lack of store aerodynamics is compensated by analyzing the system using a multiplicative uncertainty model. The model is derived assuming that the aerodynamics around the wing and the store can be equivalently captured by a modified Jones' rational approximation.

The only forces and moments acting on the store are due to the actuator which acts as an active decoupler pylon. The active decoupler pylon consists of a piezoceramic strut which acts both as a load carrying tie between the wing and the store as well as an actuator providing necessary moments at the wing and the store end to maintain the alignment between them while at the same time acting as a soft spring to isolate the wing pitch from store pitch inertia effects. The forces and moments induced by the actuator are incorporated into the equations by the principle of virtual work. The equations of motion are converted into state-space equations via the use of Jones' approximation for the Theodorsen function describing the circulatory aerodynamics around the wing.

Open-loop simulations using the wing/store parameters corresponding of an F-16 aircraft carrying a GBU/8 store configuration were used for the study throughout. The results indicate a 14.86% increase in flutter speed with the decoupler pylon over that of a bare wing and a 33.86% increase over a rigidly attached store.

Chapter 3: A linear quadratic optimal controller is designed for the single-input multi-output (SIMO). A Loop Transfer Recovery (LTR) algorithm based controller yielded a $\pm 350\%$ stability margin around the flutter frequency (25 rad/sec) that is necessary to alleviate any concerns about robustness of the system due to uncertainty in higher dynamic

modes. In terms of nominal performance, although the LQG/LTR compensated system demonstrated faster time responses and satisfactory noise attenuation properties at the outputs, the effect of sinusoidal input disturbances have not been able to get rejected. This has been illustrated by an example wherein a sinusoidal input disturbances with frequency 6 rad/sec has been shown to have made negligible reduction in the output response. Similarly the output sensitivity properties have been found to be satisfactory at the output h (plunging motion), but the pitch angle outputs did not show any improvement in sensitivity properties. This may be potentially dangerous to the actuator because it may not be able to withstand the perturbations and may result in physical failure of the strut due to resulting excessive tension or compression.

The results of this chapter has been accepted for publication into the Journal of Aircraft [43].

Chapter 4: A controller for the wing/store flutter problem is designed using the Glover-Doyle algorithm of the $\mathcal{H}_\infty$ theory which solved the minimization of a stacked objective. In particular, the simultaneous minimization (in appropriate frequency range) of the weighted output sensitivity and complementary sensitivity transfer matrices is solved. The weights were chosen based on the requirements that the output errors entering within the close range flutter frequency range (< 30 rad/sec) be rejected by 10:1 margin (with respect to that of the open-loop system) and a 40-dB/decade closed-loop roll-off rate be achieved at higher frequencies that ensures acceptable sufficient stability margins and acceptable noise attenuation. While the cost functions corresponding to the three outputs met the infinity norm objective (< 1) at higher frequencies, the cost functions corresponding to outputs α and θ did neither meet nor violate the objective at lower to mid frequency ranges. This is a potential cause for concern because at low frequencies the sensitivity margins at the pitch angles will not be sufficient enough to withstand parameter variations. This resulting freeplay between wing and the store will cause actuator failure. This could perhaps be avoided by appropriate choosing unequal weights at the three output channels.

By reflecting the uncertainties at the output of the plant, the tolerance margin around the flutter frequency was observed to be $\pm 298\%$. This magnitude of margin is essential for enduring modeling errors such as those due to store aerodynamics and other flexible modes. A typical time response comparing the perturbed open- and closed-loop system indicate the effectiveness of the controller to suppress flutter. Several other nominal performance measures including noise attenuation, input disturbance rejection, etc have been found to be satisfactory.

The results of this chapter have been published in the Journal of Guidance, Control, and Dynamics [44].

Chapter 5: In this chapter, an indirect adaptive robust control algorithm based controller is designed for a SISO wing/store model. The algorithm consists of an adaptive law that is based on gradient method modified (with leakage and switching-sigma algorithms) to make the closed-loop system more robust to uncertainties and parameter variations. The feedback control loop consists of a linear quadratic adaptive controller that uses the estimated plant parameters to construct a state observer gain matrix. Linear quadratic regulator law is then used to construct the state feedback gain matrix adaptively.

The effectiveness of the designed adaptive controller is verified by simulating a sudden change in store mass parameter (at sub-critical flutter speed) simulating the real life situation of an ejection of a bomb out of an underwing external rack. The on-line estimator performed very well in tracking the uncertain plant parameter coefficients to a small percentage error of their true value. The controller also demonstrated an improvement in performance over the open-loop response in terms of faster settling time and smaller steady-state amplitude. Moreover, the presence of an input multiplicative uncertainty model had no effect on the stability of the closed-loop system while it caused the open-loop system response to diverge (not shown). This type of robustness is especially critical during combat maneuvers.

The results of this chapter are proposed to be submitted for consideration to the Journal of Guidance, Control, and Dynamics [45].

6.2 Future Work

This study would be incomplete without incorporating actuator dynamics into the loop. While this study investigated the feasibility of using such an active approach for increasing the performance and robustness of the wing/store system from a control theoretic point of view, it is proposed that the future work would include a thorough investigation into the effect of actuator dynamics on the above results. The physical considerations of the actuator, such as force and stroke limitations, strength of the actuator material in withstanding the pitch angle variations of the wing and the store, power requirements and saturation limits etc are all proposed to be included in the future study. Scope also exists for extending the study to a more realistic subsonic regime. In terms of the control theory, re-running the simulations using unequal weights for the three cost functions (in $\mathcal{H}_\infty$ control) could throw some light into the trade-offs between performance and robustness. Another potential control strategy that could be utilized is the μ-synthesis which considers the issue of both structured as well as unstructured uncertainties simultaneously. A MIMO robust adaptive control strategy, perhaps a Least Mean Square (LMS) control or decentralized control, is also in the roster of further investigations.

Bibliography

[1] Mykytow, W. J., "Recent analysis methods for wing/store flutter," *Specialist Meeting on Wing-with-Stores Flutter*, AGARD-CP-162, April 1962.

[2] Katz, H., "Flutter of aircraft with external stores," *Proceedings of Aircraft Stores Symposium*, Vol. II, Armament Development and Test Center, Eglin Air Force Base, FL, November 1969.

[3] Foughner, J. T. Jr., and Besinger, C. T., "F-16 flutter model studies of external wing stores," *NASA-TM-74078*, October 1977.

[4] Triplett, W. E., "A feasibility study of active wing/store flutter control," *Journal of Aircraft*, Vol. 9, No. 6, 1972, pp. 438-444.

[5] Noll, T. E., Felt, L. R., Mykytow, W. J., Russell, Major, H. L., "Potential application of active flutter suppression to future fighter attack aircraft," *Aircraft/Stores Compatibility Symposium*, September 1973.

[6] Sandford, M. C., Abel, I., and Gray, D. L., "Development and demonstration of a flutter suppression system using active controls," *NASA-TR-R-450*, December 1975.

[7] Harvey, C. T., Johnson, T. L., and Stein, G., "Adaptive control of wing/store flutter," *AFFDL-TR-79-3081*, April 1979.

[8] Haidl, G., Lotze, A., and Sensburg, O., "Active flutter suppression on wings with external stores," *AGARD-AG-175*, 1974.

[9] Hönlinger, H., "Active flutter suppression on an airplane with wing mounted external stores," *AGARD-CP-228*, August 1977.

[10] Hönlinger, H., and Destuynder, R., "External store flutter suppression with active controls," *Lecture Series, von Karman Institute for Fluid Dynamics*, Vol. 2, December 1978, pp. 1-85.

[11] Reed, W. H., III, Foughner, J. T. Jr., and Runyan, H. L., "Decoupler pylon: A simple effective wing/store flutter suppressor," *Journal of Aircraft*, Vol. 17, No. 3, 1980, pp. 206-211.

[12] Reed, W. H., III, Cazier, F. W. Jr., and Foughner, J. T. Jr., "Passive Control of Wing/Store Flutter," *NASA-TM-81865*, December 1980.

[13] Triplett, W. E., Kappus, H. P. F., and Landy, R. J., "Active flutter suppression systems for military aircraft - a feasibility study," *AFFDL-TR-72-116*, February 1973.

[14] Runyan, H. L., "Effect of a flexibly mounted store on the flutter speed of a wing," *NASA-CR-159245*, April 1980.

[15] Desmarais, R. N., and Reed, W. H. III, "Wing/store flutter with nonlinear pylon stiffness," *Journal of Aircraft*, Vol. 18, No. 11, 1981, pp. 984-987.

[16] Lottati, I., "Aeroelastic tailoring of a composite wing with a decoupler pylon as a wing/store flutter suppressor," *Journal of Aircraft*, Vol. 25, No. 3, 1988, pp. 271-280.

[17] Yang, Z.-C., and Zhao, L.-C., "Wing-store flutter analysis of an airfoil in incompressible flow," *Journal of Aircraft*, Vol. 26, No. 6, 1989, pp. 583-587.

[18] Yang, Y.-R., "KBM method of analyzing limit cycle flutter of a wing with an external store and comparison with a wind-tunnel test," *Journal of Sound and Vibration*, Vol. 187, No. 2, 1995, pp. 271-280.

[19] Dowell, E. H., Crawley, E. F., Curtiss, H. C. Jr., Peters, D. A., Scanlan, R. H., and Sisto, F., "*A Modern Course in Aeroelasticity,*" Kluwer Academic Publishers, 1995.

[20] Peloubet, R. P., Jr., Haller, R. L., and McQuien, L. J., "Feasibility study and conceptual design for application of NASA decoupler pylon to the F-16," *NASA-CR-165834*, May 1982.

[21] Clayton, J. D., Haller, R. L., and Hassler, J. M. Jr., "Design and fabrication of the NASA decoupler pylon for the F-16 aircraft," *NASA-CR-172354*, January 1985.

[22] Gade, P. V. N., and Flowers, G. T., "Flutter suppression of an airfoil with unsteady forces using a piezoelectric active strut," *AIAA/ASME Adaptive Structures Forum*, AIAA paper 94-1746, April 1994.

[23] Pokines, B., Belvin, W. K., and Inman, D. J., "Static and dynamic characteristics of a piezoceramic strut," *Proceedings 5th AIAA/DOD Control-Structures Interaction Technology Conference*, 1992, pp. 133-140.

[24] Won, C. C., Sulla, J. L., Sparks, D. W. Jr., and Belvin, W. K., "Application of Piezoelectric Devices to Vibration Suppression: From Modeling and Controller Designs to Implementation," *AIAA Guidance, Navigation and Control Conference*, Paper No. 92-4610, August 1992.

[25] Carter, C., "*Design and Fabrication of Piezoelectric Wafer Actuator,*" Ph.D. Dissertation, Expected December 1998.

[26] Theodorsen, T., "General theory of aerodynamic instability and the mechanism of flutter," *NACA Report 496*, 1935.

[27] Edwards, J. W., "Unsteady aerodynamic modeling and active aeroelastic control," Stanford University, *SUDAAR 504*, Stanford, CA, February 1977.

[28] Jones, R. T., "Operational treatment of the nonuniform lift theory to airplane dynamics," *NACA Technical Note 667*, 1938.

[29] Zhou, K., Doyle, J. C., and Glover, K., *Robust and Optimal Control*, Prentice Hall, Upper Saddle River, NJ, 1996.

[30] Ridgely, D. B., and Banda, S. S., "Introduction to Robust Multivariable Control," *AFWAL-TR-85-3102*, February 1986.

[31] Dorato, P., Abdallah, C., and Cerone, V., "*Linear-Quadratic Control: An Introduction,*" Englewood Cliffs, Prentice Hall, 1995.

[32] Venkayya, V. B., and Tischler, V. A., "Frequency control and its effect on the dynamic response of flexible structures," *AIAA Journal*, Vol. 23, No. 11, November 1985, pp. 1768-1774.

[33] Dailey, R. L., "Lecture notes for the workshop on $\mathcal{H}_\infty$ and μ methods for robust control," American Control Conference, May 1990, pp. 1-116.

[34] Chang, B. C., Li., X. P., Banda, S. S., and Yeh, H. H., "Robust Control Systems Design by $\mathcal{H}_\infty$ Optimization Theory," AIAA Paper No. 91-2686-CP, 1991, pp. 723-729.

[35] Green, M., and Limebeer, D. J. N., *Linear Robust Control*, Prentice Hall, Englewood Cliffs, NJ, 1995.

[36] Maciejowski, J. M., *Multivariable Feedback Design*, Addison-Wesley Publishing Company, Wokingham, England, 1993.

[37] Chiang, R. Y., and Safonov, M. G., "*Robust-Control Toolbox*, MathWorks, South Natick, MA, 1988.

[38] Slotine, J.-J. E., and Li, W., "*Applied Nonlinear Control,*" Prentice Hall, 1991.

[39] Ioannou, P. A., and Sun, J., "*Robust Adaptive Control,*" Prentice Hall, 1996.

[40] Ioannou, P. A., and Tsakalis, K. S., "*IEEE Transactions on Automatic Control,*" Vol. 31, No. 11, 1986, pp. 1033-1043.

[41] Ioannou, P. A., and Kokotovic, P. V., "*Adaptive Systems with Reduced Models,*" Lecture Notes in Control and Information Sciences, Vol. 47, Springer-Verlag, 1983, pp. 85.

[42] Goodwin, G. C., and Sin, K. C., "*Adaptive Filtering Prediction and Control,*" Prentice Hall, Englewood Cliffs, New Jersey, 1984.

[43] Gade, P. V. N., and Inman, D. J., "Active Control of Store-Induced Flutter in Incompressible Flow," *Journal of Aircraft*, in print.

[44] Gade, P. V. N., and Inman, D. J., "Two-Dimensional Active Wing/Store Flutter Suppression Using $\mathcal{H}_\infty$ Theory," *Journal of Guidance, Control, and Dynamics*, Vol. 20, No. 5, September-October 1997, pp. 949-955.

[45] Gade, P. V. N., and Inman, D. J., "Robust Adaptive Control of Store Release Event for Wings with External Stores," *Journal of Guidance, Control, and Dynamics*, submitted and in review, March 1998.

Vita

Prasad Gade is the eldest of the two sons of Mr. Balakrishna Rao and Mrs. Gowri. He was born in Narasaraopet in India on the 8th of November, 1969. After the schooling years, Prasad entered Birla Institute of Technology and Science, Pilani (India) in 1987 where he received a Bachelors degree in Mechanical Engineering and a Masters degree in Mathematics as part of the dual degree program in 1992. He then came to U.S.A. to pursue graduate degree in Mechanical Engineering at Auburn University. After receiving the Masters degree in 1994, he spent the last three-and-a-half years at Virginia Tech where he is a doctoral candidate in the Engineering Science and Mechanics department. During his tenure as a Ph.D. student, he married Sridevi Chintapalli on the 1st of January, 1997 and constantly gets reminded by her that he has no excuse of forgetting their wedding anniversary.